NTNU – Trondheim
Norwegian University of
Science and Technology

Onset and Progression of Vortical Structures for a Surface Combatant at Drift Angles 0, 10 and 20 Degrees

Tale Fjell Egeberg

NTNU
Department of Marine Technology

MASTER THESIS

Onset and Progression of Vortical Structures for a Surface Combatant at Drift Angles 0, 10 and 20 Degrees

---

Author:
Tale Fjell Egeberg

Supervisor NTNU:
Bjørnar Pettersen

Supervisor IIHR:
Fred Stern

5th June 2013

Abstract

The onset on progression of vortical structures of the ship model DTMB 5512 (geosym of DTMB5415) has been examined for drift angles -1°, 10° and 20°, by means of tomographic particle image velocimetry (TPIV). The drift angle β = -1°, which is close to the neutral angle, was chosen instead of 0°, when it was discovered that 0° gave asymmetry in the flow. The DTMB 5415 is preliminary design for a surface combatant for the US Navy, and is equipped with a transom stern and a sonar dome in the bow, as well as bilge keels. Two major streamwise vortices are detected for β=-1°, the sonar dome vortex (SDV) and the fore-body keel vortex (FBKV). There is also a vortex forming on the bilge keel (called the bilge-keel vortex, BKV). For β=10° the main flow feature is the SDV. One vortex forms on either side of the sonar dome, and merge between X/L_{pp}=0.120 and X/L_{pp}=0.200. A BKV is seen on the leeward side at X/L_{pp}=0.600, but merges quickly with the SDV. At X/L_{pp}=0.935 the windward BKV has drifted close to the centreline, and in addition a vortex has formed on the after-body. The major vortices of β=20° are the SDV, FBKV and windward FBKV. Only one SDV is observed, and it is assumed that the windward SDV dissipates rapidly because of the strain from the strong crossflow at this drift angle. The inception the the FBKV's is around X/L_{pp}=0.200, and it is assumed that they either dissipate or merge with the stronger SDV at some point between X/L_{pp}=0.400 and X/L_{pp}=0.600. Vortices form on both bilge keels at X/L_{pp}=0.400. The leeward BKV persists until somewhere between X/L_{pp}=0.600 and X/L_{pp}=0.800. At X/L_{pp}=0.800 the windward BKV has drifted close to the centreline, and we see the early formation of a vortex on the after-body. The ABKV still persists at X/L_{pp}=0.935.

Detailed analysis of the 3D mean flow field is performed for X/L_{pp}=0.400, in order to determine the influence of drift angle on the turbulent kinetic energy (TKE), Reynolds stresses, strain rates, vorticity and vortical structures. The magnitude of strains, stresses, and thus TKE, as well as vorticity increase with the drift angle. For the two largest drift angles, the maxima of strains and stresses are in the vicinity of the SDV. For β=-1°, the proximity of the hull influences the stress and strain field. Iso-surfaces of Q>0 and λ_2<0 are used to identify vortical structures. There seems to be little difference between them when computing mean values, although λ_2 appears to be more sensitive to the measurement noise close to the model surface. For the instantaneous iso-surfaces, λ_2 seems to cap-

ture more small vortex filaments, but the major trends are the same.

Frequency analysis of the SDV of β=20° at measurement stations X/L$_{pp}$=0.060 - 0.600 reveal a dominant frequency of approximately 3[Hz] for the spanwise velocity components, but no dominant frequency for the streamwise component.

Sammendrag

Virvelsystemet til skipsmodellen DTMB 5512 (geosym av DTMB5415) har blitt undersøkt eksperimentelt ved hjelp av *tomographic particle image velocimetry* (TPIV), for tre statiske avdriftvinkler -1°, 10° og 20°. Vinkelen β = -1°, som er nær den faktiske nøytralvinkelen, ble valgt istedet for 0° da det ble oppdaget at denne gav et asymmetrisk strømningsbilde. DTMB 5415 er et tidlig design til et krigsskip for US Navy. Skipet har tverr hekk, og er utstyrt med en sonarkuppel i baugen.

Det dannes to virvler på sonarkuppelen ved alle avdriftvinkler, og disse blir sterkere når vinkelen øker. For 10° forenes de to virvlene til en kort tid etter at de oppstår, og for 20° antas det at virvelen på babord side dissiperer raskt grunnet den sterke tverrstrømningen ved denne vinkelen. Det observeres også virveldannelse på forskipet, samt på slingrekjølene, samt på etterskipet for 10° og 20°.

Strømningsbildet ved X/L$_{pp}$=0.400 studeres i detalj, for å avgjøre avdriftvinkelens betydning for turbulent kinetisk energi, Reynolds-stress, og virvling, samt størrelse og form på de ulike virvlene. Det observeres at størrelsene på de overnevnte variblene øker med vinkelen.

FFT benyttes for å avgjøre om det finnes en dominant frekvens for virvelen fra sonarkuppelen ved β = 20°. Det observeres en frekvens på 3[Hz] for v og w, men ingen tydelig dominant frekvens for u.

Acknowledgements

First of all I would like to thank my supervisor Bjørnar Pettersen, whose bright idea it was that I should go to Iowa and to do my thesis work, and my co-supervisor Fred Stern who agreed to host me. Bjørnar may have been slightly surprised that I took to the idea so fast; in fact I wrote to him only a week after our meeting to ask how the initial planning was going, and kept nagging about it until the plans were settled. My visit at IIHR has been a very valuable experience, and I hope other master students from NTNU will get the opportunity to go in the future.

My sincere thanks to Hyunse Yoon who has been a great help to me during my work at IIHR, and who took care of the post-processing of the TPIV raw images. I would also like to thank Lichuan Gui and his vast army of undergrads, who were responsible for the TPIV measurements.

Last, but not least, a great big thank you to Haitham Elshiekh, who kindly guided me through the bureaucracy of US immigration my first week in Iowa, when I was dazed and confused, and had the flu on top of everything.

Tale Fjell Egeberg

Contents

Nomenclature

Greek Letters

β	Drift angle [$Degrees$]
Δ	Mass displacement [kg]
ρ_p	Tracer particle density [kgm^{-3}]
σ	Dynamic sinkage [$Degrees$]
τ	Dynamic trim [m]
μ_f	Dynamic viscosity of a fluid [Nsm^{-2}]
ω	Vorticity vector [s^{-1}]
Ω_{ij}	Vorticity tensor [s^{-1}]

Symbols

∇	Volume displacement [m^3]
B_{WL}	Breadth at water line [m]
C_B	Block Coefficient [-]
d_p	Tracer particle diameter [m]
D_w	towing carriage wheel diameter [m]
$Fn=\frac{U}{\sqrt{gL}}$	Froude number [-]
F_i	Force in i-direction, i=x,y,z [N]
H_N	Normalized Helicity Density [-]
L_0	Characteristic length of obstacle in suspended particle flow [m]
L_{pp}	Length between perpendiculars [m]
L_{WL}	Length at waterline [m]
M_i	Moment in i-direction, i=x,y,z [Nm]
T_m	Mean draft [m]
S_{ij}	Strain rate tensor [s^{-1}]
U_B	Calibration factor for towing speed measurement [-]
U_T	Towing speed [ms^{-1}]
U_{T0}	Nominal towing speed [ms^{-1}]
$u = U(x,y,z,t)/U_T$	normalized streamwise velocity [-]
$v = V(x,y,z,t)/U_T$	normalized horizontal spanwise velocity [-]
$w = W(x,y,z,t)/U_T$	normalized vertical spanwise velocity [-]
$R_e = UL/\nu$	Reynolds Number [-]

$x = X/L_{pp}$ normalized x-coordinate [-]
$y = Y/L_{pp}$ normalized y-coordinate [-]
$z = Z/L_{pp}$ normalized z-coordinate [-]

Abbreviations

ABKV	After-body Keel Vortex
AD	Analogue-digital
BKV	Bilge-keel Vortex
CFD	Computational Fluid Dynamics
DFT	Discrete Fourier Transform
DTMB	David Taylor Model Basin
EFD	Experimental Fluid Dynamics
FBKV	Fore-body Keel Vortex
FFT	Fast Fourier Transform
HPIV	Holographic PIV
IIHR	Iowa Institute of Hydraulic Research
INSEAN	Istituto Nazionale per Studi ed Esperienze di Architettura Navale
KLD	Karhunen-Loeve Decomposition
LW	Leeward
MIT	Massachusetts Institute of Technology
NSWC	Naval Surface Warfare Center
PCA	Principal Component Analysis
PIV	Particle Image Velocimetry
PMM	Planar Motion Mechanism
POD	Proper Orthogonal Decomposition
px	Pixels
SDV	Sonar Dome Vortex
SVD	Singular-Value Decomposition
SPIV	Stereoscopic PIV
TPIV	Tomographic PIV
WW	Winward

1   Introduction

Oblique flow is a topic of great interest in ship hydrodynamics. The effects of an incident drift angle has consequences for resistance, propulsion performance, manoeuvring characteristics and stability.

A number of studies have examined the effects of drift angle on propeller performance. The influence of drift angle on the forces and moments of propellers have been studied for the case of a single four-bladed propeller (Meyne and Nolte, 1973), and for high speed twin screw vessels (Sasajima and Muruhashi, 1980). The flow-straightening effect of the propeller on a rudder in oblique flow was investigated by Ymuro (1980), and cavitation on the propellers of high speed displacement ships in oblique flow conditions was investigated by Rutgersson (1981). Recent efforts include a numerical study of a marine propeller in tight manoeuvring conditions (Dubbioso et al., 2013), and an experimental study of shaft loads on an azimuth propeller subjected to oblique flow and waves (Amini and Steen, 2011)

Studies of oblique flow around ship hulls have treated the effect of drift angle on the forces and moments, as well as on the vortex systems. Hydrodynamic forces and moments on a transom stern high-speed ship in oblique static drift was treated by Fan and Lu (1991). Longo and Stern (2002) investigated the effect of drift angle on forces and moments, as well as sinkage, trim and heel for a cargo/container model ship. The wave pattern and vortical structures were also investigated. Interesting findings from this study include the occurrence of a wave-breaking vortex from the breaking bow wave. The flow structures(Marcu and Lungu, 2012) and manoeuvring coefficients (Phillips et al., 2009), as well as forces and moments (Kume et al., 2006; Toxopeus, 2011; Wang et al., 2011) of the KVLCC2 tanker model have been investigated for various drift angles. The numerical investigation of the KVLCC vortex system by Xing et al. (2012) is of particular interest to the present study. Static drift angles $0°$, $12°$ and $30°$ were simulated, and vortex breakdown with helical mode instability in the wake of the breakdown was observed for the major vortices.

The objective of the present work is to investigate the influence of drift angle on the onset and progression of vortical structures for the surface combatant model DTMB 5415, by means of data from tomographic particle image velocimetry (TPIV) experiments. The project is unique in that

TPIV is used to document ship flow in a towing tank; to the knowledge of the author, the towed TPIV system at IIHR is the only one of its kind in operation at this point.

The overall purpose of the study is to provide validation data for computational fluid dynamics (CFD). A vast effort of providing reliable benchmark data for numerical analysis has been going on since the 1970's. The first international workshop on numerical prediction of viscous ship flow was held in Gothenburg in 1980 (Larsson, 1981), and since then the workshop has been repeated a number of times. Recent efforts have focused on three modern hull forms, introduced at the Gothenburg workshop in 2000 (Larsson et al., 2003); a tanker (KVLCC1 and -2) a container ship (KCS) and a surface combatant (DTMB 5415).

The DTMB 5415 is a preliminary design of a surface combatant for the U.S. Navy from approximately 1980, with a transom stern and a sonar dome in the bow. The geometry is widely used as a test case for evaluation of general CFD tools (Zhao and Zhang, 2003; Muscari and Di Masco, 2004; Moraga et al., 2008; Ahmed, 2011) as well as optimization-oriented ones (Peri and Campana, 2003; Kim et al., 2010; Huang and Feng, 2012).

The vortical structures, as well as forces and moments, of the DTMB 5415 at a static drift angle of 20° was investigated numerically by Bhushan et al. (2011). The labels of the different vortices detected in the current work will follow the naming convention from that study.

IIHR has a long-standing collaboration with DTMB and INSEAN on obtaining benchmark data for the DTMB 5415, including forces and wave pattern(Gui et al., 2001), wake topology (Logo et al., 2007), coupled heave and pitch motions (Irvine Jr. et al., 2008) and uncertainty analysis (Longo and Stern, 2005). Scars and vortices induced by bow and shoulder wave breaking were studied by Olivieri et al. (2007). For a summary of the progress before 2000, please refer to Stern et al. (2001).

The use of TPIV is a major step forward in the ability to characterize the vortex systems of a ship model. Detailed 3D-3C measurements allows a better understanding of the behaviour of vortices and turbulent structures of the hull. Where in-plane vorticity and 2D turbulent kinetic energy (TKE) were previously the only tools available to determine the strength and position of swirling structures from PIV data, we are now able to use more robust criteria for vortex detection, such as the Q-criterion (see

section 2.1.1).

The experimental technique of particle image velocimetry (PIV) will not be elaborated herein. Readers who are unfamiliar with the concept are advised to consult the detailed and well written work of Adrian and Westerweel (2011).

2 Theory and Background

In this section some background will be given on vortex identification, and also on some mathematical tools that are relevant for the data analysis. In addition, a brief overview of volumetric PIV techniques will be given, comparing them to tomographic PIV.

2.1 Vortex definitions and detection

The notion of a vortex is so well established in the field of fluid dynamics that few stop to consider the actual definition. The fact of the matter is that, currently, no single definition of the vortex is universally accepted. This may be surprising to some, considering the long history of fluid-dynamics research, and the wide use of vortex dynamics to explain flow phenomena. Turbulence is commonly described by its elementary components, often called eddies or coherent structures (Cantwell, 1981), and much of turbulence physics is well explained using vortex dynamics (Hunt, 1987). This brings urgency to the question of a stringent definition of vortices.

When considering a vortex, here understood as the *vortex core*, several intuitive definitions spring to mind, such as vorticity maxima, pressure minima and closed or spiralling streamlines. Unfortunately, neither of these criteria are unambiguous.

Regions of high vorticity are not only found in vortices, but also in parallel shear flows. Although the criterion has been used with some success for free shear flows (Hussain and Hayakawa, 1987; Bisset et al., 1990), it may not always be satisfactory, for example in flows where the vorticity magnitude of the shear regions is similar to that of the vortex core. For planar wall-bounded flows, Lugt (1979) showed that the vorticity maxima and minima occurred solely at the wall, which means that any vortices

would pass undetected if the method relied on vorticity maxima.

The reasoning behind the local pressure minimum criterion is that, in a vortex, there tends to be a pressure minimum on the axis of the swirling motion when the centrifugal force is balanced by the pressure force (called the cyclostrophic balance (Neumann and Pierson, 1966)). This is, however, only strictly true in steady inviscid planar flow. Jeong and Hussain (1995) point out that a well-defined pressure minimum can exist in unsteady irrotational flow which does not necessarily involve a vortex (a vortex is required to have a net vorticity). Also, sinks and sources have pressure minima at the origin, but involve no swirling motion whatsoever.

Definitions of a vortex requiring closed or spiralling streamlines are problematic because most of them are not Galilean-invariant, i.e. the stream topology changes under Galilean transformations such as constant speed translations (Haller, 2005). Another important inadequacy is that a particle may not complete a full revolution around the core during the lifetime of a vortex, and will thus go undetected if closed streamlines are required.

Roughly speaking there are two main categories of vortex identification schemes (Sahner, 2009):

 i) Vortex region detection

 ii) Vortex core line extraction

In the first category vortical structures are defined as regions where some scalar quantity lies within a certain value range. Examples of such criteria are the well known Q, λ_2 and Δ criteria. These techniques are generally Galilean invariant due to the fact that they use velocity derivatives only. Region detection methods will be discussed in section 2.1.1. The second category is based on finding the centreline of the vortex, however it may be defined in each individual method. An example of this is the notion of the vortex core as the center of swirling motion (Sujudi and Haimes, 2010). A summary of these techniques will be given in section 2.1.2. One of the important differences between these two classes of methods is that whereas the vortex region techniques require user interaction, the vortex line methods are largely automatic once started. Vortex region detection requires setting a threshold to exclude noise, and the user must make a decision on whether or not the structure observed is actually a vortex.

2.1.1 Vortex region detection methods

The most popular vortex region criteria are based on the decomposition of the velocity gradient tensor into its symmetric and antisymmetric parts, the strain rate tensor and the vorticity tensor respectively. Thus, we have

$$\nabla \boldsymbol{u} = \boldsymbol{S} + \boldsymbol{\Omega}. \tag{1}$$

where the strain rate tensor is given as

$$\boldsymbol{S} = \frac{1}{2} \left[\frac{\partial u_i}{\partial x_j} + \frac{\partial u_j}{\partial x_i} \right], \ i, j = 1, 2, 3, \tag{2}$$

and the vorticity tensor is given as

$$\boldsymbol{\Omega} = \frac{1}{2} \left[\frac{\partial u_i}{\partial x_j} - \frac{\partial u_j}{\partial x_i} \right], \ i, j = 1, 2, 3, \tag{3}$$

The strain rate tensor indicates the amount of stretching and folding in the flow, driving the mixing process, while the vorticity tensor indicates vortical activity.

A three-dimensional set of of first-order differential equations can be written as

$$\dot{\boldsymbol{x}} = \boldsymbol{A}\boldsymbol{x}, \tag{4}$$

where $\boldsymbol{x} = [x_1 \ x_2 \ x_3]$.In the case of fluid flow a_{ij} are the coefficients of the rate-of-deformation tensor (velocity gradient tensor) evaluated at $(x_1, x_2, x_3) = (0, 0, 0)$ (Chong et al., 1990). For steady flow, the solution trajectories correspond to streamlines, whereas for unsteady flow they correspond to particle paths. If λ_1, λ_2 and λ_3 are the eigenvalues of $\mathbf{A}$, then

$$[\boldsymbol{A} - \lambda \boldsymbol{I}] \, \boldsymbol{e} = 0, \tag{5}$$

where $\boldsymbol{e}$ is the eigenvector. The eigenvalues can be determined by the characteristic equation

$$det \, [\boldsymbol{A} - \lambda \boldsymbol{I}] = 0. \tag{6}$$

For a 3×3 matrix we write this

$$\lambda^3 + \boldsymbol{P}\lambda^2 + \boldsymbol{Q}\lambda + \boldsymbol{R} = 0, \tag{7}$$

where $\boldsymbol{P} = div(\nabla\boldsymbol{u})$, $\boldsymbol{Q} = \frac{1}{2}\left[trace(\nabla\boldsymbol{u})^2 - trace(\nabla\boldsymbol{u}^2)\right]$ and $\boldsymbol{R} = det(\nabla\boldsymbol{u})$ are the three invariants of $\nabla\boldsymbol{u}$. Different vortex region methods have different requirements for the invariants.

The first three-dimensional vortex criterion, the Q-criterion, was proposed by Hunt et al. (1988), defining the vortex as a spatial region where the second invariant of $\nabla\boldsymbol{u}$ is positive, with the additional requirement that the pressure in the region be lower than the ambient value. Q is given as

$$Q = \frac{1}{2}\left[trace(\nabla\boldsymbol{u})^2 - trace(\nabla\boldsymbol{u}^2)\right] = -\frac{1}{2}\left[|\boldsymbol{S}|^2 - |\boldsymbol{\Omega}|^2\right]. \qquad (8)$$

Thus, the Q-criterion is defined as

$$Q = -\frac{1}{2}\left[|\boldsymbol{S}|^2 - |\boldsymbol{\Omega}|^2\right] > 0. \qquad (9)$$

From the above equation we see that negative values of Q, indicating no vortical structures, occur when strain dominates the vorticity. A weakness of this criterion is that $Q > 0$ does not imply that the pressure minimum occurs within the region; it could occur on the boundary of the region. Thus, there is no explicit connection between a region where $Q > 0$ and a region with a pressure minimum.

Chong et al. (1990) proposed another well-known criterion, the Δ-criterion. Eigenvalues of the velocity gradient tensor are used to classify the streamline pattern around any point in the flow, in a frame of reference moving with the velocity at this point. Here, vortices are defined as regions where

$$\Delta = \left(\frac{Q}{3}\right)^3 + \left(\frac{det\nabla\mathbf{u}}{2}\right)^2 > 0. \qquad (10)$$

This Galilean-invariant method is linked to the intuitive concept of a vortex gives spiralling streamlines with respect to some frame of reference. It can be shown that if the Jacobian of the streamline pattern has a conjugate pair of complex eigenvalues, the flow exhibits spiralling motion locally, in a plane corresponding to these values. Δ gives the eigenvalue magnitude. Thus, a large Δ signifies strong spiralling pattern in the given reference frame.

For the λ_2-criterion, proposed by Jeong and Hussain (1995), the vortex core is defined as a connected region with two negative eigenvalues of

$\boldsymbol{S}^2 + \boldsymbol{\Omega}^2$, which is equivalent to the second largest of the three eigenvalues being negative, $\lambda_2 < 0$. The criterion is based on two requirements for the vortex core:

(i) A vortex core must have a net vorticity.

(ii) The geometry of the identified vortex core must be Galilean invariant.

Taking the gradient of the Navier-Stokes equation and extracting the symmetric part gives

$$\frac{D\boldsymbol{S}_{ij}}{Dt} - \nu \boldsymbol{S}_{ij,kk} + \boldsymbol{S}_{ik}\boldsymbol{S}_{kj} + \boldsymbol{\Omega}_{ik}\boldsymbol{\Omega}_{kj} = -\frac{1}{\rho}p_{,ij}. \qquad (11)$$

The first two terms on the left-hand side of this equation represent unsteady irrotational strain and viscous effects respectively. Now, as unsteady straining can cause pressure minima without the involvement of vortices, and viscous effects may eliminate the pressure minimum in a vortical flow, these effects are simply discarded to obtain the definition of λ_2.

In most cases the Q- and λ_2 definitions will give similar results, but Jeong and Hussain (1995) give some examples in which the Q gives inadequate results compared to λ_2. In the case of a vortex passing through a vortex ring, the Q=0 shows disconnected vortex cores along the axis of the continuous axisymmetric vortex column (see fig. 1). This indicates that the Q-criterion is not an adequate definition for a vortex expanding due to an imposed non-uniform strain field, which might give problems when Q is applied to vortices with strong core dynamics. It is important to note that whereas Q<0 has a clear physical interpretation, i.e. strain-dominated flow, there is no such physical concept related to $\lambda_2 > 0$.

8
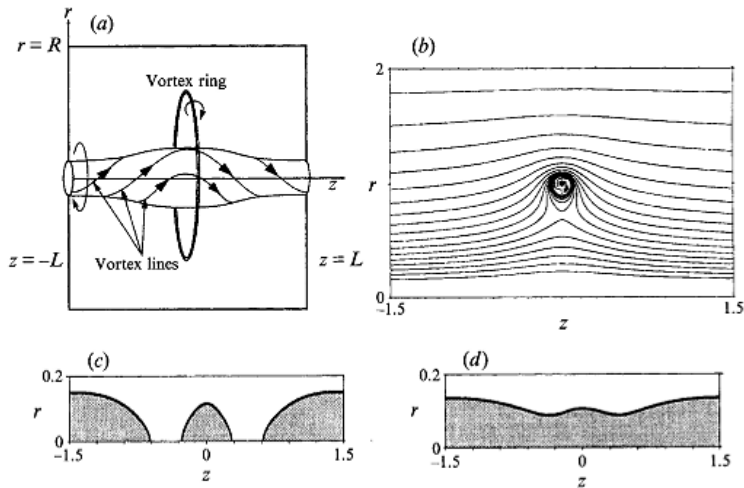
Figure 1: Axial vortex passing through a vortex ring. a) schematic view b) stream function c) Q=0 d) λ_2 =0. From Jeong and Hussain (1995, Fig.10).

The λ_{ci} - criterion by Zhou et al. (1999) is based on the Δ - criterion, and uses the imaginary part of the complex eigenvalue of the velocity gradient tensor for vortex identification. Provided that $\nabla \boldsymbol{u}$ has complex conjugate eigenvalues, the streamlines in the locally curvelinear coordinate system (y_1, y_2, y_3), which is spanned by the vectors $(\mathbf{u}_1, \mathbf{u}_2, \mathbf{u}_3)$ and locally translating with the fluid particle, are given by

$$y_1(t) = y_1(0)e^{\lambda_r t} \tag{12}$$

$$y_2(t) = y_2(0)e^{\lambda_{cr}t}\left[y_2(0)cos(\lambda_{ci}t) + y_3(0)sin(\lambda_{ci}t)\right] \tag{13}$$

$$y_3(t) = y_3(0)e^{\lambda_{cr}t}\left[y_3(0)cos(\lambda_{ci}t) - y_2(0)sin(\lambda_{ci}t)\right]. \tag{14}$$

The so-called 'swirling-strength' λ_{ci} is a measure of the local swirling rate inside the vortex, where the time it takes to complete one revolution is $2\pi\lambda_{ci}$. The strength of vortex stretching or compression is given by λ_r. In addition to identifying vortex regions, the swirling strength criterion also identifies the strength and local plane of the swirl motion.

Chakraborty et al. (2005) proposed the following requirements for the identification of a vortex core

(i) The identification criterion should be Galilean invariant.

(ii) The local flow in the frame of reference translating with the vortex should be swirling.

(iii) The separation between swirling material points inside the vortex core should remain small, i.e. the orbits of the material points are compact.

Their method is based on λ_{ci}. The criteria that satisfy the above requirements are given as

(i) $\lambda_{ci} \geq \epsilon$

(ii) $\lambda_{cr}/\lambda_{ci} \leq \delta$

where ϵ and δ are positive threshold values. Small values of λ_{ci} corresponds to a fluid particle using a long time to complete a revolution about the core, implying a weak vortex. Similarly, large values implies a strong vortex. Large values of the ratio $\lambda_{cr}/\lambda_{ci}$ implies that neighbouring particles do not remain neighbours throughout an entire revolution about the core, defying the requirement of compact orbits.

Haller (2005) proposed a vortex criterion which is not only Galilean-invariant, but also objective. Like the Q-criterion, it identifies vortex- and strain-dominated regions in the flow, but opposed to the criteria presented so far, $\boldsymbol{M_z}$ is based on a Lagranian approach.

In continuum mechanics, a quantity can be called objective is it remains invariant when subjected to perturbations of the form

$$\tilde{\boldsymbol{x}} = \boldsymbol{Q}(t)\boldsymbol{x} + \boldsymbol{b}(t), \tag{15}$$

where $\boldsymbol{Q}(t)$ is a time-dependent proper orthogonal tensor and $\boldsymbol{b}(t)$ is a time-dependent translation vector. This combination holds all possible changes in frame of reference.

Galilean-invariant techniques will give consistent results in reference frames that move at constant relative speeds. Haller, however, states that Galilean invariance is not sufficient, as criteria based on this may fail to be invariant under more general conditions, such as in the case of rotating frames of reference.

Without diving too deep into the mathematics of the analysis, it is proven that a trajectory is hyperbolic (saddle-type) as long as the strain acceleration tensor $\mathbf{M}$ remains positive over a zero strain cone $\mathbf{Z}$ moving with the trajectory. Hyperbolic trajectory manifolds are responsible for folding and stretching in the flow.

$$\mathbf{M} = \partial_t \mathbf{S} + (\nabla \mathbf{S}) + \mathbf{S}(\nabla \mathbf{v})^T \mathbf{S} \tag{16}$$

Restricting $\mathbf{M}$ to $\mathbf{Z}$ in an an arbitrary point gives either positive definite or indefinite values. Thus, vortices are defined as sets of trajectories with indefinite values $\mathbf{M_z}$, i.e. elliptic. In numerical applications with a sparse grid, there is little chance of finding a trajectory which is wholly elliptic or wholly hyperbolic. In this case qualitative observations on $\mathbf{M_z}$ can still be made. Low values indicate strain-dominated flow, i.e. a majority of hyperbolic points along the path-line. High values indicate vortex-dominated flow, i.e. a majority of elliptic points along the path-line.

2.1.2   Vortex core line detection methods

Several techniques for detecting the core line of a vortex exist, based on the notion that a vortex can be described as circular particle motion around a common centre. Robinson (1991) described the vortex as follows:

> 'A vortex exists when instantaneous streamlines mapped onto a plane normal to the vortex core exhibit a roughly circular or spiral pattern, when viewed from a reference frame moving with the center of the vortex core'

As mentioned in the introduction to this section, there are some issues associated with these techniques, namely lack of Galilean invariance, and the fact that, in rapidly evolving flows, fluid particles may not complete a full orbit in the lifetime of a vortex. Nevertheless, these methods can be very useful for obtaining information about the flow structures.

Sujudi and Haimes (2010) devised an algorithm for identifying the centre of swirling motion in 3D vector fields, based on critical-point theory. A critical point is defined as a point where the slope of the streamline is indeterminate and the velocity is zero in an appropriate frame of reference. According to critical point theory, the eigenvalues and eigenvectors of the

rate-of-deformation tensor evaluated at a critical point defines the flow pattern around this point. If the rate-of-deformation tensor has one real and two complex-conjugate eigenvalues, the critical point is of focus-saddle type (see fig. 2). Intuitively, such a point is a centre of swirling motion. By employing the concept of reduced velocity, the criteria for the focus-saddle point are extended to non-critical points in the flow. The reduced velocity $\boldsymbol{u_r(x)}$ at a point $\mathbf{x}$ is given as the projection of the steady flow field $\mathbf{u(x)}$ onto the plane normal to the real eigenvector $\mathbf{e}$:

$$\boldsymbol{u_r(x) = u(x) - [u(x)e(x)]e(x)}. \tag{17}$$

If the reduced velocity is zero, the point is the centre of swirling motion. This method is not Galilean invariant, but depends on the frame of reference. Weinkauf et al. (2007) generalized this method for unsteady flows.
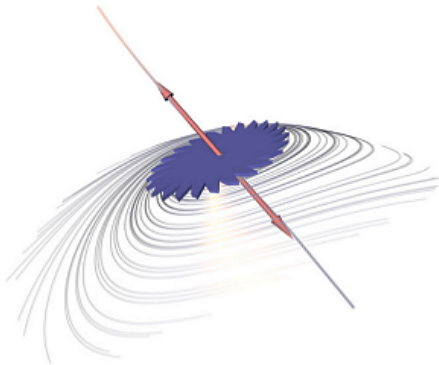
Figure 2: Critical point of focus-saddle type. The blue plane is spanned by the eigenvectors corresponding to the complex eigenvalues. The centre of the swirling motion is the real eigenvector, denoted by the red arrows. From Sahner (2009, fig 3.3)
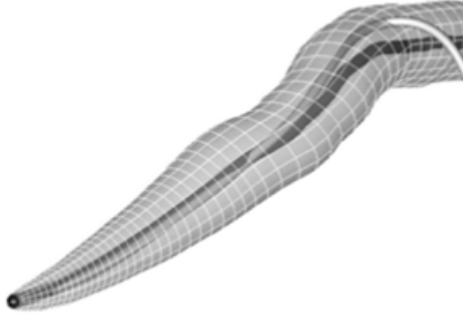
Figure 3: Vortex tube with vorticity line (white) and corrected vorticity line (black). From Banks and Singer (1994, fig 3)

Banks and Singer (1994) developed a vortex core identification method based on vorticity, using the pressure as a correcting factor. Vorticity lines are used to trace the vortex skeleton. A vorticity line is defined as a lines which is tangent to the local vorticity vector in every point. Alone, these lines might stray from the vortex, but imposing a criterion for the pressure along the line makes the method self-correcting. The skeleton is grown from an initial seed point, which is determined by a requirement of high vorticity and low pressure. Once the seeding point is found, the next position is determined by integration along the vortex line. This position is then adjusted to lie at the pressure minimum in the plane perpendicular to the original vorticity vector. Figure 3 gives an example of the results from this method. Notice how the vorticity line (white) strays from the vortex tube, but the corrected line (black) stays in place.

A Galilean invariant vortex core line detection method was proposed by Sahner et al. (2005). The method is in fact a combination of core line and region methods (as defined in the section 2.1), as it is based on extracting vortex lines from Galilean-invariant quantities such as Q or λ_2. Maxima lines of Q > 0 are called ridge valley lines and minima lines of λ_2 < 0 are called valley lines (see fig. 4). The lines are extracted using the method of feature flow fields (Theisel and Seidel, 2003). The methodology is similar to that of Banks and Singer (1994). First seeding points for the maximum/minimum lines are found, and these points are used to extract the rest of the lines as field lines of a derived velocity field, called the feature flow field. A drawback of this method is that it requires second-

order derivatives.
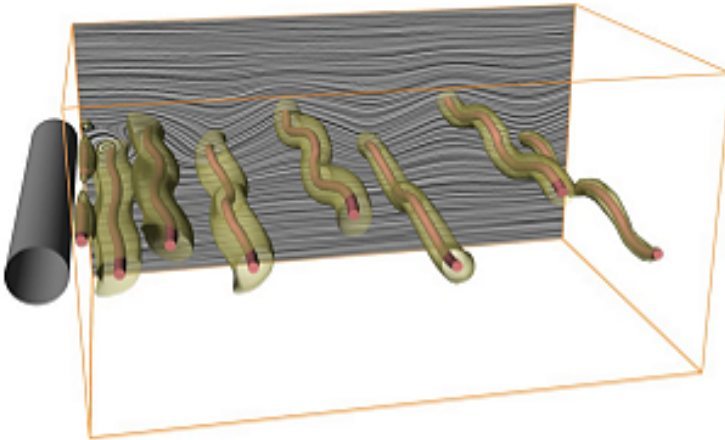
Figure 4: Valley lines behind a circular cylinder with λ_2 iso-surfaces. From Sahner et al. (2005, fig 1 c))

A related method based on λ_2 was proposed by Schafhitzel et al. (2008). The vortex core is defined as a curve which connects λ_2 minima restricted to planes that are perpendicular to the core lines. The algorithm consists of the following steps:

i) λ_2 iso-surface extraction.

ii) Computation of the curve skeleton of the λ_2 iso-surface to build an initial prediction for the core line.

iii) Correction of the locations of the prediction by searching for λ_2 minima on planes perpendicular to the core line.

One of the the advantages of this technique is that the topology of the vortex core is guaranteed to be the same as the initial curve skeleton. However, it is a geometrical approach, tracking the vortex core line in the spatial domain only, not in time.

2.1.3 Application of vortex detection criteria in the current study

Among the above criteria, Q, λ_2 and λ_{ci} seem to be the most common applied to experimental data from tomographic PIV. One reason for this is that they are easy and fast to implement with computer tools such as MATLAB or Tecplot. In this study we shall mainly make use of the Q-criterion, but the λ_2 - criterion will be used for comparison. To get a better understanding of these quantities we shall go through the equations more carefully. First the Q-criterion:

$$
\begin{aligned}
Q &= -\frac{1}{2}\left[\boldsymbol{S}_{ij}\boldsymbol{S}_{ij} - \boldsymbol{\Omega}_{ij}\boldsymbol{\Omega}_{ij}\right] \\
&= -\frac{1}{2}\left[\frac{1}{4}\left[\frac{\partial u_i}{\partial x_j} + \frac{\partial u_j}{\partial x_i}\right]^2 - \frac{1}{4}\left[\frac{\partial u_i}{\partial x_j} - \frac{\partial u_j}{\partial x_i}\right]^2\right] \\
&= -\frac{1}{2}\frac{\partial u_i}{\partial x_j}\frac{\partial u_j}{\partial x_i}, \ \ i,j = 1,2,3.
\end{aligned}
$$

Written in Cartesian coordinates we get

$$
Q = -\frac{1}{2}\left[\left(\frac{\partial u}{\partial x}\right)^2 + \left(\frac{\partial v}{\partial y}\right)^2 + \left(\frac{\partial u}{\partial x}\right)^2 + 2\frac{\partial u}{\partial y}\frac{\partial v}{\partial x} + 2\frac{\partial v}{\partial z}\frac{\partial w}{\partial y} + 2\frac{\partial u}{\partial z}\frac{\partial w}{\partial x}\right].
$$

As we already know, λ_2 is the second largest eigenvalue of the symmetric matrix

$$
\boldsymbol{A} = \boldsymbol{S}_{ik}\boldsymbol{S}_{kj} + \boldsymbol{\Omega}_{ik}\boldsymbol{\Omega}_{kj},
$$

where

$$
\begin{aligned}
a_{11} &= S_{11}^2 + S_{12}^2 + S_{13}^2 - \Omega_{12}^2 - \Omega_{13}^2 \\
a_{12} &= S_{11}S_{12} + S_{12}S_{22} + S_{13}S_{23} - \Omega_{13}\Omega_{23} \\
a_{13} &= S_{11}S_{13} + S_{12}S_{23} + S_{13}S_{33} - \Omega_{12}\Omega_{23} \\
a_{22} &= S_{12}^2 + S_{22}^2 + S_{23}^2 - \Omega_{12}^2 - \Omega_{23}^2 \\
a_{23} &= S_{12}S_{13} + S_{22}S_{23} + S_{23}S_{33} - \Omega_{12}\Omega_{13} \\
a_{33} &= S_{13}^2 + S_{23}^2 + S_{33}^2 - \Omega_{13}^2 - \Omega_{23}^2.
\end{aligned}
$$

After some calculations, we get

$$
\begin{aligned}
a_{11} &= \left(\frac{\partial u}{\partial x}\right)^2 + \frac{\partial u}{\partial y}\frac{\partial v}{\partial x} + \frac{\partial u}{\partial z}\frac{\partial w}{\partial x} \\
a_{12} &= \frac{1}{2}\frac{\partial u}{\partial x}\left[\frac{\partial u}{\partial y} + \frac{\partial v}{\partial z}\right] + \frac{1}{2}\frac{\partial v}{\partial y}\left[\frac{\partial u}{\partial y} + \frac{\partial v}{\partial x}\right] + \frac{1}{2}\frac{\partial u}{\partial z}\frac{\partial w}{\partial y} + \frac{1}{2}\frac{\partial w}{\partial x}\frac{\partial v}{\partial z} \\
a_{13} &= \frac{1}{2}\frac{\partial u}{\partial x}\left[\frac{\partial u}{\partial z} + \frac{\partial w}{\partial x}\right] + \frac{1}{2}\frac{\partial w}{\partial z}\left[\frac{\partial u}{\partial z} + \frac{\partial w}{\partial x}\right] + \frac{1}{2}\frac{\partial v}{\partial x}\frac{\partial v}{\partial z} + \frac{1}{2}\frac{\partial u}{\partial y}\frac{\partial w}{\partial y} \\
a_{22} &= \left(\frac{\partial v}{\partial y}\right)^2 + \frac{\partial u}{\partial y}\frac{\partial v}{\partial x} + \frac{\partial v}{\partial z}\frac{\partial w}{\partial y} \\
a_{23} &= \frac{1}{2}\frac{\partial v}{\partial y}\left[\frac{\partial v}{\partial z} + \frac{\partial w}{\partial y}\right] + \frac{1}{2}\frac{\partial w}{\partial z}\left[\frac{\partial v}{\partial z} + \frac{\partial w}{\partial y}\right] + \frac{1}{2}\frac{\partial u}{\partial y}\frac{\partial w}{\partial x} + \frac{1}{2}\frac{\partial v}{\partial x}\frac{\partial u}{\partial z} \\
a_{33} &= \left(\frac{\partial w}{\partial z}\right)^2 + \frac{\partial u}{\partial z}\frac{\partial w}{\partial x} + \frac{\partial v}{\partial z}\frac{\partial w}{\partial y}.
\end{aligned}
$$

All the calculations have been performed in Tecplot, which was also used to plot the resulting iso-surfaces. An example of comparison between the two criteria is shown in figure 5. Using the same absolute values of Q>0 and λ_2<0 should give similar results, i.e. the same shape and size of vortical structures. Indeed, the differences between the two plots are very slight. λ_2 seems to capture more small vortex filaments than Q, as can be seen in the region marked by a black circle. The hole which can be seen in the Q>0 SDV is also a result of this; that the $\lambda_2 \sim$ -1000 iso-surfaces capture a larger amount of small-scale structures. Apart from this, the maxima seem to be located in the same places and the overall shape of the SDV is similar.

(a) Q iso-surfaces **(b)** λ_2 iso-surfaces
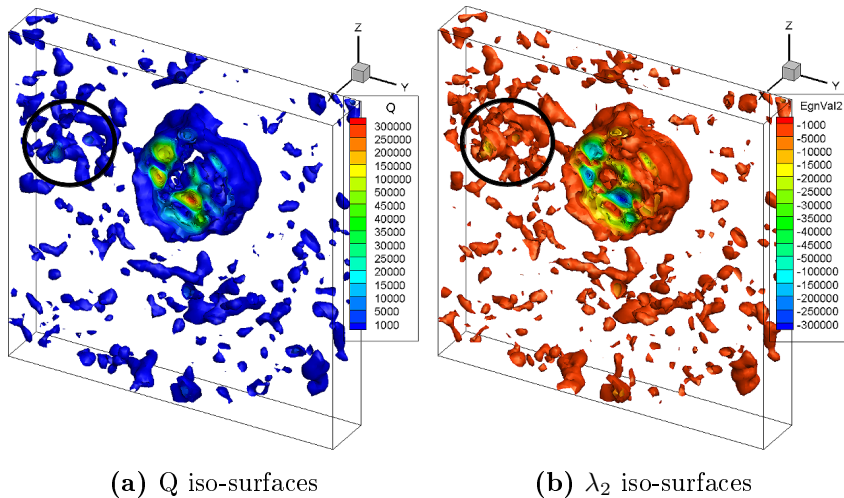
Figure 5: Q and λ_2 iso-surfaces from a time-instance of the SDV of $\beta=20°$ at x=0.400.

Neither Q nor λ_2 provide information about the direction of swirl. For this puropse, we employ the normalized helicity density H_N (Levy et al., 1990), given as

$$H_N = \frac{\boldsymbol{u} \cdot \boldsymbol{\omega}}{|\boldsymbol{u}||\boldsymbol{\omega}|}, \tag{18}$$

where $\boldsymbol{u}$ is the velocity vector and $\boldsymbol{\omega}$ is the vorticity vector. $-1 \leq H_N \leq 1$ is the scalar product of the two vectors, giving the directional cosine between them. The sign of H_N indicates the direction of the vortex swirl relative to the streamwise velocity component. Figure 6 shows the same iso-surfaces as figure 5, only coloured by H_N. There hardly any difference between $\lambda_2<0$ and Q>0, neither in direction nor magnitude of H_N.
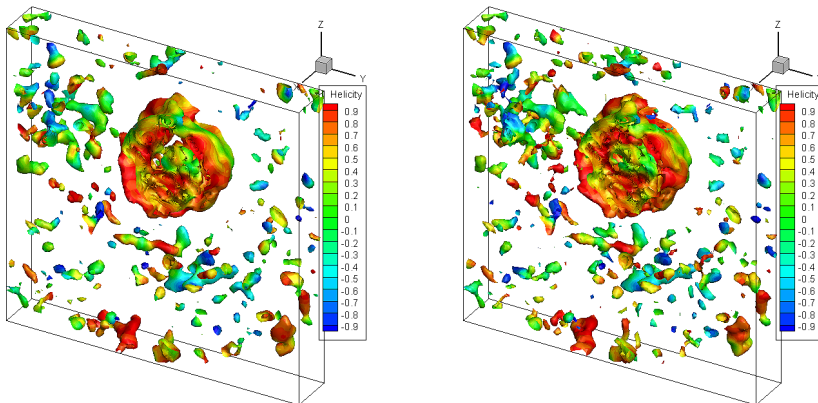
(a) Q iso-surfaces coloured by H_N **(b)** λ_2 iso-surfaces coloured by H_N

Figure 6: Q and λ_2 iso-surfaces from a time-instance of the SDV of $\beta=20°$ at x=0.400, coloured by H_N.

2.2 Mathematical tools

2.2.1 Proper Orthogonal Decomposition

Proper orthogonal decomposition (POD) is a powerful data analysis method for obtaining low-dimensional approximations of high-dimensional processes (Liang et al., 2002). In fluid mechanics it is commonly employed in analysis of turbulent flows, where it can be used to identify which structures have the largest contributions to the kinetic energy. POD has been proved to be an effective method for identifying dominant features and events for both experimental and numerical data (Feng et al., 2011).

The techniques uses the orthogonal transformation to convert a data-set where the variables might be correlated, into a set of linearly independent variables known as the proper orthogonal modes. The transformation is such that the first mode contains the most energy, and each successive mode contains less energy than the previous. The idea is that the high-dimensional process can be sufficiently described by choosing a finite number of modes to represent it. Here, only a brief summary of the POD technique will be given. Please refer to Berkooz et al. (1993) for a more rigorous treatment of the method.

Assume a velocity function with spatio-temporal variation $\mathbf{u}(\mathbf{x}, t)$. The

18

function bases that give the best approximation of the velocity are $\boldsymbol{a}_n(t)$ and $\boldsymbol{\phi}_n(x)$, so that

$$\boldsymbol{u}(\boldsymbol{x},t) = \sum_{n=1}^{\infty} \boldsymbol{a}_n(t)\boldsymbol{\phi}_n(x). \qquad (19)$$

The velocity function is now decomposed into its spatial and temporal components. The eigenfunction $\boldsymbol{\phi}_n(x)$ must be determined as to maximize the function

$$\frac{\langle (\boldsymbol{u},\boldsymbol{\phi})(\boldsymbol{u},\boldsymbol{\phi}) \rangle}{(\boldsymbol{\phi},\boldsymbol{\phi})} = \lambda \geq 0, \qquad (20)$$

where $\langle \rangle$ denotes the ensemble average and $(,)$ denotes the inner product. λ is the eigenvalue, also called mode energy. This classic maximization problem leads to the formulation

$$\int \langle \boldsymbol{u}(\boldsymbol{x})\boldsymbol{u}^*(\boldsymbol{x'}) \rangle \boldsymbol{\phi}(\boldsymbol{x'})d\boldsymbol{x'} = \lambda\boldsymbol{\phi}(\boldsymbol{x}). \qquad (21)$$

There are three basic ways of solving this problem, principal component analysis (PCA), Karhunen-Loeve Decomposition (KLD) and Singular-Value Decomposition (SVD)(Liang et al., 2002).

In the current study we have used the built-in POD tool of the PIV software, which is a black-box approach seeing as the mathematical background of the tool is not elaborated in the manual[1]. In order to give the reader an example of a solution approach, we look to Meyer et al. (2007). Their method uses the so-called 'snapshot POD' introduced by Sirovich (1987).

Assuming a velocity fluctuation field $\boldsymbol{u} = (u, v)$, all fluctuating velocity components from N snapshots can be arranged in a matrix

$$\boldsymbol{U} = [\boldsymbol{u_1}, \boldsymbol{u_2}, \cdots, \boldsymbol{u_n}]. \qquad (22)$$

Then, the autocovariance function is given by

$$\boldsymbol{M} = \boldsymbol{U^T U}. \qquad (23)$$

---

[1]Upon asking for details about this from LaVision, the author was simply told that the 'standard method' had been used.

From this, the eigenvalue problem can be solved by

$$\boldsymbol{MA_i} = \lambda_i \boldsymbol{A_i}, \tag{24}$$

where λ is the eigenvalue and $\boldsymbol{A}$ is the eigenvector. The eigenvalues are ordered by size, from large to small values, so that the most energetic modes come first. The eigenvectors are used as a basis for the POD modes, so that

$$\boldsymbol{\phi_i} = \frac{\sum_{n=1}^{N} A_{i,n} \boldsymbol{u}_n}{\left|\left|\sum_{n=1}^{N} A_{i,n} \boldsymbol{u}_n\right|\right|}, \ i = 1, 2, \cdots, \boldsymbol{N}, \tag{25}$$

where $A_{i,n}$ is the nth component of the eigenvector corresponding to the ith eigenvalue λ_i. $||(\cdots)||$ denotes the discrete 2-norm, defined as

$$||y|| = \sqrt{y_1^2 + y_2^2 + \cdots + y_n^2}. \tag{26}$$

The POD coefficients are determined by projecting the fluctuating part of the velocity field onto the POD modes, so that

$$\boldsymbol{a}_i = \boldsymbol{\psi^T} \boldsymbol{u}_n, \tag{27}$$

where $\boldsymbol{\psi} = [\boldsymbol{\phi}_1 \ \boldsymbol{\phi}_2 \cdots \boldsymbol{\phi}_N]$. When the POD coefficients and modes are known, the velocity field can be reconstructed using the first Nth modes, so that

$$\boldsymbol{u}_n = \boldsymbol{\psi} \boldsymbol{a}_n. \tag{28}$$

Here, the velocity fluctuations have been used to calculate the POD modes, but it has been shown that the velocities themselves can be used with a similar result (Feng et al., 2011).

Applied to the current experimental data, there is a notable improvement to the frequency analysis after POD is applied. Figure 8 shows the FFT's of the vertical crossflow component extracted at five points in the β=20° SDV. It is not possible to distinguish any peaks, although, based on CFD analysis, dominant frequencies were expected to occur. We do see some peaks, but none of which are similar for all points. This is most likely due to the high noise level of the measurement. Figure 8 shows the same dataset, but reconstructed using the first ten POD modes that had

a contribution to the energy of more than 1%.This number of modes was considered sufficient to represent the velocity field, and adding modes did not give additional information. Now dominant frequencies that coincide in all five points are clearly visible. This demonstrates the efficacy and usefulness of POD analysis for complex turbulent flows.
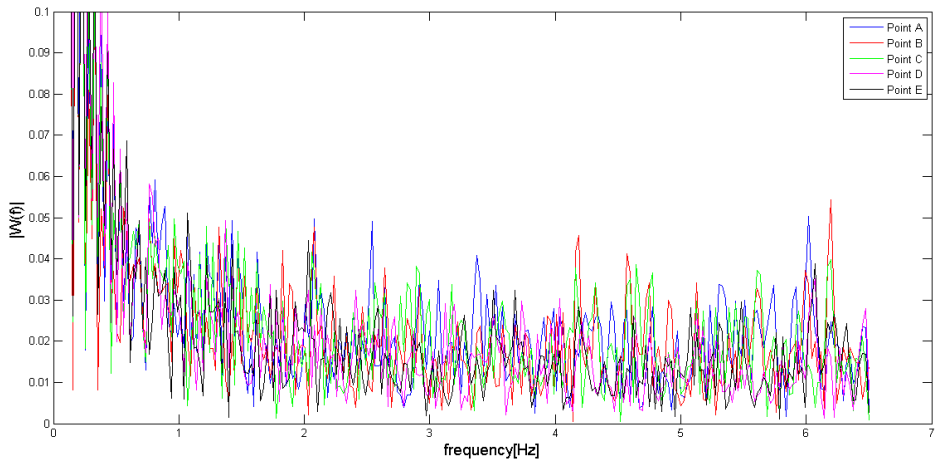
Figure 7: FFT of w at five points in the β=20° SDV, before POD reconstruction.
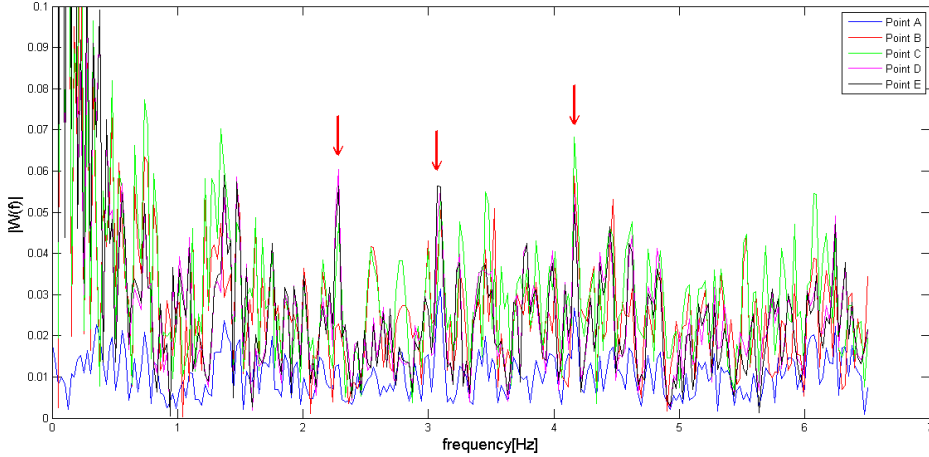
Figure 8: FFT of w at five points in the β=20° SDV, after POD reconstruction. Dominant and secondary frequencies that coincide for all points marked by red arrows.

2.2.2 The Discrete Fourier Transform and Spectral Leakage

When applying the Fourier transform, one must be aware that it implicitly applies to an infinitely repeating signal. Applying it to a finite signal can cause so-called spectral leakage, or aliasing, which is in effect the introduction of new frequency components.

Assume we are sampling a continuous signal with a sampling frequency f_s. This gives the sampling period

$$\Delta t = \frac{1}{f_s}. \tag{29}$$

The frequency of the kth array element in the frequency domain, frequently referred to as a frequency bucket, can be related to the signal sampling frequency as

$$f_k = \frac{k}{N\Delta t} = \frac{k}{N} f_s, \tag{30}$$

where k is the bucket number and N is the number of samples. It follows from the above equation that k, which is always an integer, can be expressed as

$$k = \frac{f_k}{f_s} N. \tag{31}$$

This expression tells us two things:

i) For a given number of samples, the frequency resolution is inversely proportional to the sampling rate.

ii) For a given sampling rate, frequency resolution is proportional to the number of samples.

Lyon (2009) elegantly describes this effect by means of Heisenberg uncertainty principle. Certain pairs of physical properties cannot be accurately determined simultaneously. For the Discrete Fourier Transform (DFT) these variables are time and frequency. To get better frequency precision we need more samples, and thus a longer time window. However, this decreases the time precision, i.e. our ability to localize the event in time. The same problem applies when reversing our properties. Any attempt to precisely locate the event in time leads to a decreased number of samples, which declines the precision in frequency.

Now, let us look at the current experimental work. 20[s] of data has been sampled with a frequency of $13[Hz]$, which gives us N=260. Since most FFT routines requires a sample size of a power of 2, that leaves us with N=256. Keeping in mind that k has integer values only, we see that a bucket frequency of 1[Hz], as an example, gives k=19.69152. Since this is not possible, spectral energy leaks between buckets 19 and 20, hence the name spectral leakage.

To negate the effects of spectral leakage 'windowing' is applied. This technique modulates the input signal so that the spectral leakage is evened out over all frequency components. Windowing is done by multiplying the input signal by a window function, reducing the amplitudes at the beginning and end of a sample. Windowing will also reduce the overall amplitudes in the frequency domain. There are numerous such functions available, and their different properties make them suited for different types of input signals.

In this study, the frequency behaviour of the SDV was first investigated by means of the built-in Fast Fourier Transform (FFT) tool in MATLAB.

Although the source code of this function is not available to the public, we know that it is based on the FFTW library (Frigo and Johnson, 1998) developed at Massachusetts Institute of Technology (MIT). The FFTW library uses the Cooley-Tukey algorithm (Cooley and Tukey, 1965) to decompose the Discrete Fourier Transform (DFT).

The performance of the MATLAB fft tool has been examined by applying it to a sinusoidal function of two components. One component has amplitude 0.1 and frequency $3[Hz]$ and the other has amplitude 0.05 and frequency $5[Hz]$ so that

$$y(t) = 0.1sin(6\pi t) + 0.05sin(10\pi t). \tag{32}$$
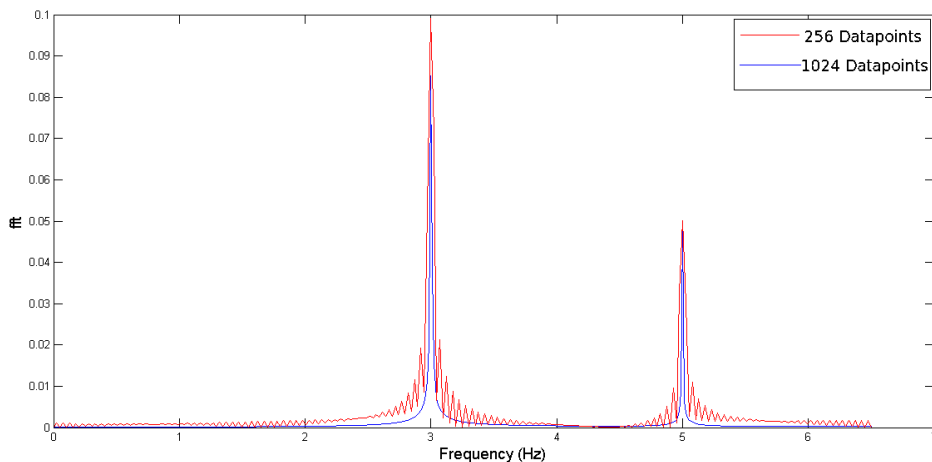
Figure 9: Test of built-in MATLAB FFT routine using 1024(blue) and 256(red)data-points.

The FFT was applied using 1024 data-points and 256 datapoints, which is the number of datapoints we have in our actual measurement series (actually the number is 260, but without using zero-padding the FFT requires the sample length to be a power of 2). A sampling frequency of $13[Hz]$ was used for the test. From figure 9 we see that the amplitude approximation of the signal is better at 260 data-points, particularly for the largest amplitude. A certain amount of spectral leakage is observed in both cases,but the side lobes are sharper and have a larger amplitude

when the number of datapoints is decreased.

In figure 10, the signal has been corrupted with random noise. The noise is made by multiplying MATLAB's rand() function, which gives a random number between 0 and 1, by a threshold amplitude. First we try a maximum noise amplitude of 0.1. We see that the frequencies are still accurately determined, but the amplitudes are no longer accurate for either dataset. Since the amplitude of the noise is low compared to the signal, we are still able to identify the dominant frequencies. However, when increasing the noise level above order of magnitude of the amplitude of the dominant frequency, the FFT is no longer able to extract useful frequency information. This can be seen in figure 11, where the maximum amplitude of the noise is increased to 0.5. We see that for the longest signal the FFT is still able to distinguish the peak with the highest amplitude, at $3[Hz]$, but the smaller amplitude peak is lost in the noise. For the shorter signal, no dominant frequencies are distinguishable. If the noise level in the current measurement is close to the amplitude of the turbulent fluctuations, distinguishing the relevant frequency content could be problematic without additional filtering.
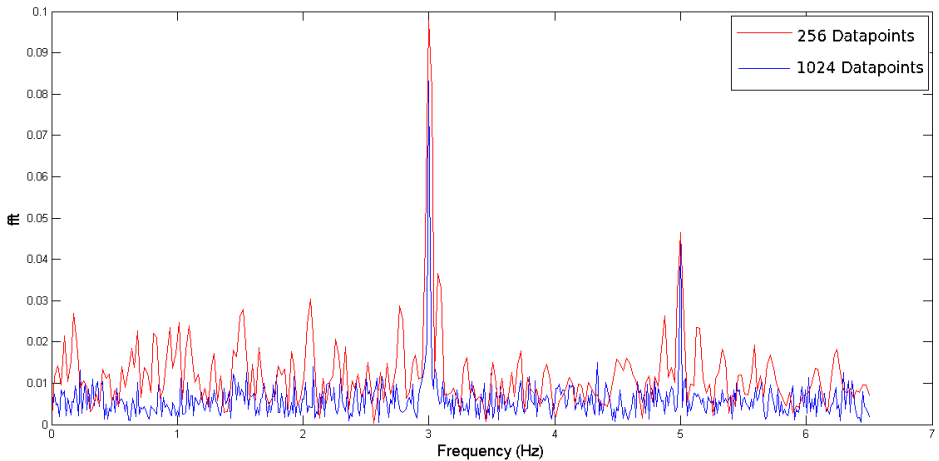
Figure 10: Test of built-in MATLAB FFT routine using 1024(blue) and 256(red)data-points. The input signal has been corrupted by random noise with a maximum amplitude of 0.1.
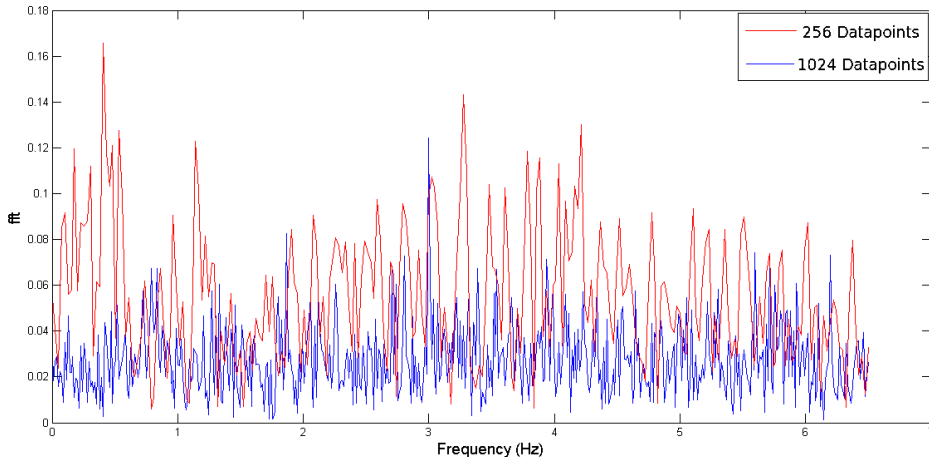
Figure 11: Test of built-in MATLAB FFT routine using 1024(blue) and 256(red)data-points. The input signal has been corrupted by random noise with a maximum amplitude of 0.5.

Now, we apply the MATLAB fft() to the time signal extracted at five point in the SDV for $\beta=20°$. The data has been reconstructed using the first ten POD modes. The effect of spectral leakage is clearly visible in the lower frequency ranges in figure 12a, depicting the FFT of the vertical crossflow component. In order to reduce the leakage, which might cover interesting features of the frequency content, a Hamming window has been applied, given by

$$w_H(n) = 0.54 - 0.46cos\left(2\pi\frac{n}{N}\right),\ 0 \le n \le N. \tag{33}$$

The Hamming windows aims at reducing the first side-lobe of the dominant frequency. As opposed to the widely used Hann window, it does not go to zero at the end of the sample. The reduction of the first side-lobe is greater than the Hann window, but the remaining lobes decay slower when the Hamming window is used (Donnelly and Rust, 2005). Figure 12b shows the FFT's after windowing. The amplitudes are significantly reduced, and the peaks are broader than before the window was applied. Actually, the peak amplitudes are approximately half of the original amplitude. Trying different windows gives approximately the same result. This is not ideal, and a better approach would be to use an FFT tool which was

less sensitive to spectral leakage. Particularly so, as we do not have access to the MATLAB source code, and are thus unable to investigate further into the reasons for the spectral noise.
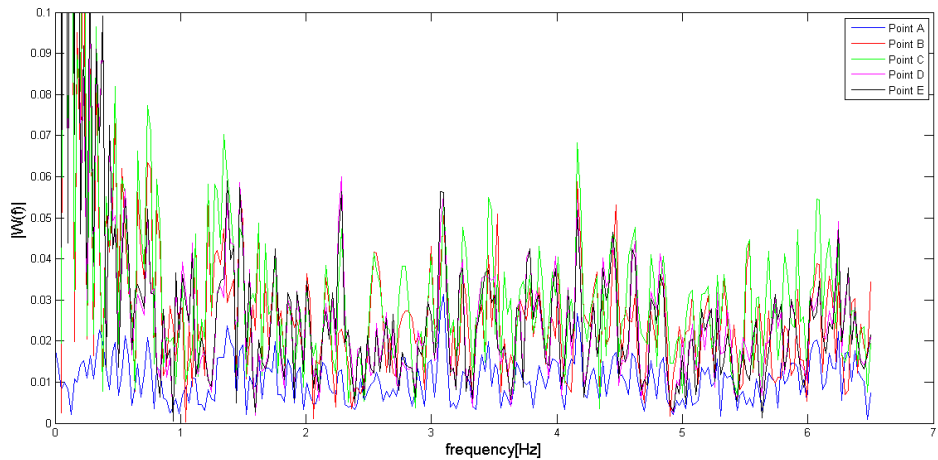
(a) No window applied.
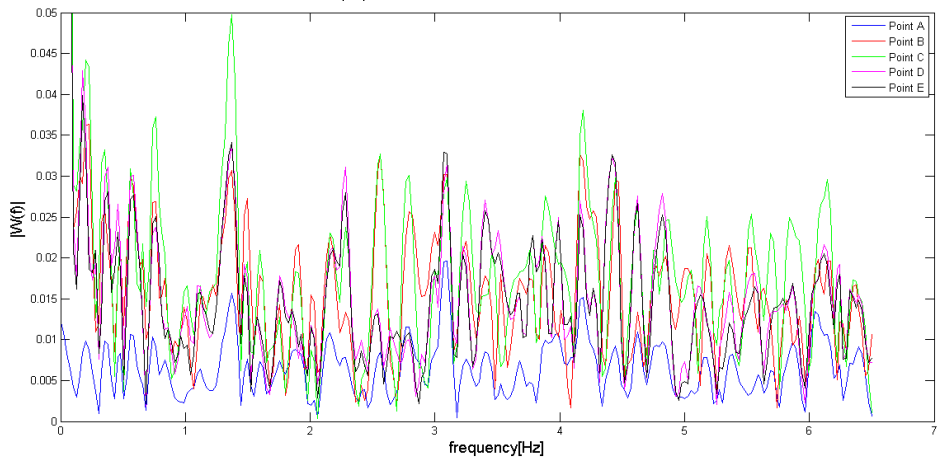
(b) Hamming window applied.

Figure 12: FFT of w, overlap of all five points. Data reconstructed from the first ten POD modes.

In order to get a comparison to the results from MATLAB, and possibly

a better tool, we apply a FORTAN routine (Press et al., 1992, p. 498-503) to compute the FFTs. First the behaviour of the tool is investigated for the same sinusoidal signal as before. Figures 13 and 14 show the performance test of the FORTRAN routine.
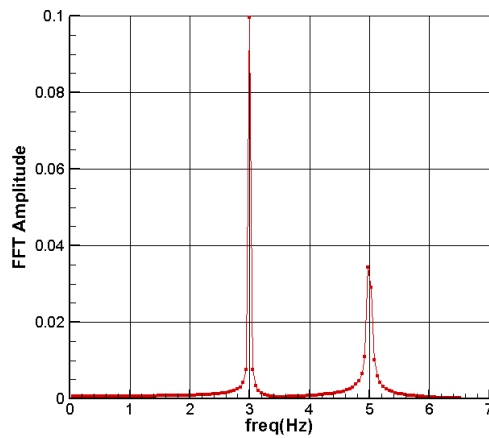
Figure 13: Test of FORTRAN 77 FFT routine, 256 datapoints, sampling frequency 13[Hz].
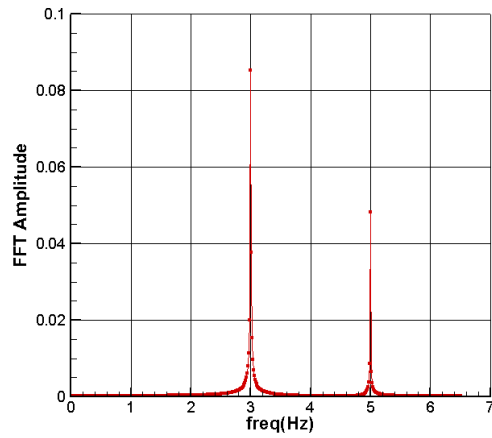
Figure 14: Test of FORTRAN 77 FFT routine, 1024 datapoints, sampling frequency 13[Hz].
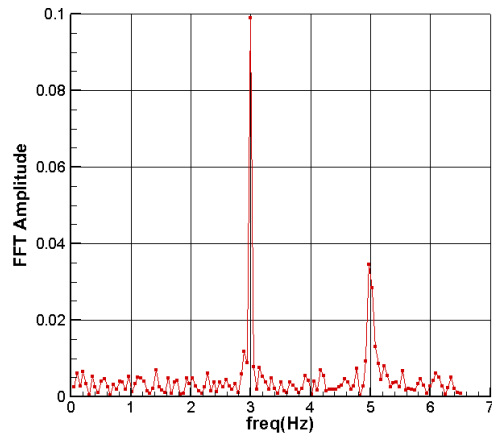
Figure 15: Test of FORTAN 77 FFT routine, 256 datapoints, random noise with a maximum amplitude of 0.1.
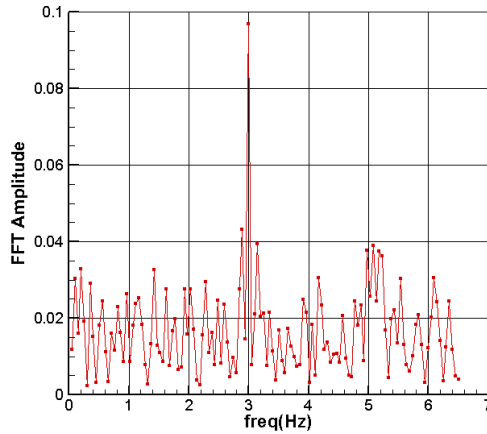
Figure 16: Test of FORTAN 77 FFT routine, 256 datapoints, random noise with a maximum amplitude of 0.5.

From figures 13 and 14, we see that the largest amplitude of the signal is well resolved with the 256-point series. The peaks are rather broad, which means that there is a certain amount of spectral leakage close to the dominant frequencies. The lower amplitude is reduced with respect to the input signal. For the 1024-point series there is less leakage, but both amplitudes are significantly reduced with respect to the input signal. However, the leakage is significantly smaller than for the FFTs computed using MATLAB. Also, the sharp sidelobes that were seen for the 256-point signal are completely gone.

Random noise of amplitudes 0.1 and 0.5 has been added to the 256-point signal(Figures 15 and 16). We see that for the lower noise amplitude both frequencies are still distinguishable. For the highest noise amplitude the 5[Hz] peak is no longer distinguishable, due to its low amplitude. The peak at 3[Hz], however, is still well resolved. Note that this was not the case for the 256-point series when computed by the MATLAB routine; no meaningful frequency content was distinguishable.

Figure 17 shows the FFT of the vertical crossflow component, calculated from the time signal extracted at five point in the SDV for β=20°(the same points that were tested for the MATLAB routine). There is no ev-

idence of the kind of spectral leakage that occurred when the MATLAB
routine was applied to the same dataset. This means that windowing is
rendered unnecessary simply by switching the numerical routine. It is un-
fortunate that we do not have the possibility to examine why this is, but it
can be concluded that the FORTRAN routine is a more robust tool then
the MATLAB routine. Thus, we shall use the FORTRAN FFT routine in
any further analysis.
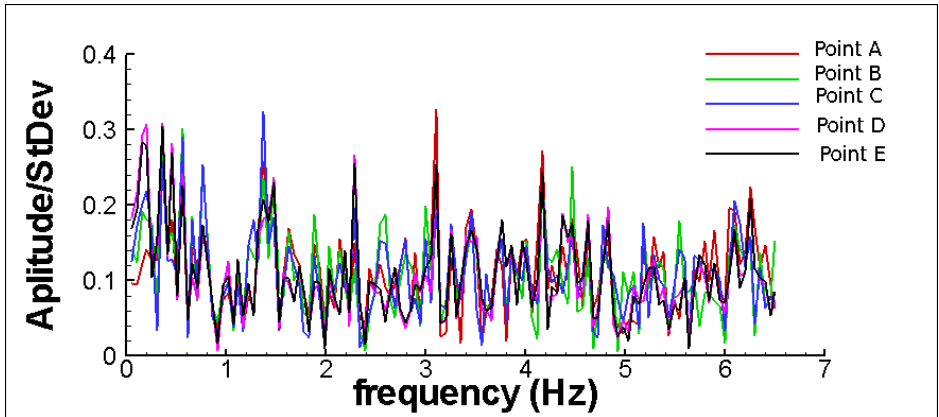
Figure 17: FFT of w, all points overlap. The amplitudes have been normalized
by the standard deviation of w.

2.3 Tomographic PIV and other volumetric PIV methods

Tomographic PIV (TPIV) is used for 3D velocity measurements. Instead
of a very thin light-sheet, as in conventional PIV techniques, a volume
section is illuminated. The volume thickness varies. It might be compa-
rable to a thick light-sheet, typically $8[mm]$, or it can be a full volume,
$10\text{-}14[mm]$. The volumetric particle distribution is reconstructed from
multiple camera views, and the displacement field is calculated by means
of three-dimensional cross-correlation. Interrogation volumes replace the
usual interrogation areas, and the three-component displacement is found
in each volume. The entire domain is illuminated instantaneously, and the
particles over the domain are all in focus, which requires a relatively small
lens aperture.

The number of cameras in the setup can be varied, though four is

common. In principle, two views would be sufficient to reconstruct the 3D particle distribution, but the performance of the system can be significantly increased by using more than two cameras. Other variables that affect the reconstruction quality are the angle between the camera axis and the volume face, the particle density within each interrogation volume, volume thickness, and the accuracy of the calibration. A comprehensive study of the effect of these parameters, as well as a thorough description of the technique, is found in Elsinga et al. (2006).

To the knowledge of the author no material has been published regarding tomographic PIV applied to ship hydrodynamics. However, numerous literature exists on cases that are relevant to marine technology in a broader sense. Flow around circular cylinders, an important topic in the offshore industry, is investigated by means of TPIV by Hain et al. (2007) (finite cylinder), Scarano and Poelma (2009)(vorticity considerations). The flow around a pitching plate, easily compared to the rudder of a ship, was investigated by Buchner et al. (2012). Turbulent boundary layer flow was the subject of Schröder et al. (2008), Buchmann et al. (2010) and Elsinga et al. (2012).

There are several other PIV techniques, in addition to tomographic PIV, that allow 3D measurements. Examples are stereoscopic PIV (Prasad, 2000), holographic PIV (Hinsch, 2002),scanning- and multi-plane systems (Brucker, 1995; Khäler and Kompenhaus, 2000) as well as defocusing techniques (Pereira and Gharib, 2002).

Stereoscopic PIV (SPIV) is commonly used for experimental setups in both wind- and water facilities. The advantage of SPIV over TPIV is that the laser power required to illuminate a light sheet, as opposed to a full volume, is much lower which allows a larger field of view (FOV) for SPIV compared to TPIV. A stereoscopic field-of-view could be 40 by 40 [cm], whereas for TPIV it is typically 10 by 10[cm] or smaller. For example, Wolf and Hörnschemeyer (2012) use a FOV of only 34 by 13 [mm]. Stereoscopic PIV is, however, not fully 3C, in that the out-of-plane component is not directly measured, but reconstructed from the in-plane components. Comparison between the SPIV and TPIV suggests that TPIV is better suited for strongly three-dimensional flows (De Kat and Van Oudheuseden, 2012).

Schäfer and Schröder (2011) compared holographic and tomographic

PIV with emphasis on resolving the time-dependent, three-dimensional small-scale structures. In holographic PIV interference of coherent light scattered by the tracer particles and a reference beam is used to encode information of the amplitude and phase of the scattered light incident on a sensor plane, i.e. the hologram. When illuminating the hologram with the reference beam the original light intensity field can be reconstructed, and velocity information is obtained by means of 3D cross-correlation of the intensity field. The main drawbacks of this technique lie in the extreme complexity of the experimental setup and the time it takes to develop the holographic plate. With fully digital techniques, such as TPIV, the quality of the images can be checked instantly, and modifications can be made quickly if needed. This is not possible with HPIV. The same problem is encountered when in the process of optimizing interrogation volume size, overlap etc. Depending on the desired resolution, this could take a few hours. The advantage of HPIV over TPIV is that it allows for larger volumes. Still, TPIV provides higher spatial resolution, and this, combined with the relative simplicity of the setup, gave the conclusion that TPIV was the most promising technique for measurement of small-scale turbulence.

Scanning-plane PIV is a quasi-volumetric technique. By means of a rotating mirror, the light-sheet is scanned across the measurement domain taking 2D or stereoscopic PIV measurements in each plane. The major drawback of this technique is that obtaining the true instantaneous velocity field in the volume is not possible, only the average field. Nevertheless, Hori and Sakakibara (2004) deemed that their time resolution was sufficient to capture the instantaneous vortical structures (represented by vorticity iso-surfaces) and 3D streamlines of a turbulent round jet. The Reynolds number was 1000 and 50 planes were traversed by the light sheet over a time interval of $0.22[s]$. The residue of the divergence was used as an error estimate, and was calculated to 7% of the vorticity rms at the centreline of the jet.

Multi-plane PIV is somewhat similar to the scanning-plane method, but instead of using a single light-sheet traversing the flow, several planes are measured simultaneously, or a with a small offset in time, depending on the flow and which variables are of interest. Schröder and Kompenhaus (2004) used multi-plane PIV to investigate a turbulent spot. The experiment was conducted in a low turbulence wind tunnel facility, using

a vertically mounted flat plate with an elliptic leading edge and a flap at the trailing edge. A turbulent spot was introduced to the laminar flow by local injection of air. Two measurement planes parallel to the wall were used. The planes had a small height-wise(in the boundary layer) separation and were either measured simultaneously or staggered in time. This allowed the determination of relevant turbulent quantities such as the velocity fluctuation fields, the Reynolds stresses of all four quadrants, the in-plane component of vorticity, rms fields, and the corresponding probability density functions (PDF), as well as spatial and space-time correlations.

The same setup was later used by Schröder et al. (2008) for a feasibility study of time-resolved tomographic PIV applied to the investigation of a turbulent spot. A $32 \times 18 \times 29 \ [mm^3]$ measurement volume was sampled at $5[kHz]$. The coherent structures organization is analyzed by 3D-vorticity and -swirling-strength (λ_{ci}) iso-surfaces visualization. Streaks and hairpin-like or arch vortical structures are most prominent. The role of these structures in the spatio-temporal development of the flow is better understood when using TPIV data, as the double-plane technique of the previous study was limited, and could not capture the whole complex process.

Willert and Gharib (1992) introduced the technique of defocusing PIV. Unlike other 3D PIV techniques, which are predominantly multi-camera setups, it uses a single camera, equipped with a three hole aperture, to capture the flow within a measurement volume. In the raw image, a single particle shows up as three particles forming an equilateral triangle. The position and size of these triangles are used extract depth information. Originally a pointwise reconstructed velocity field, it was extended to a voxel-based description by Pereira and Gharib (2002). The error in the reconstructed displacements were found to be approximately 1% in the in-plane directions, whereas the error in the depth-displacements was up to six times larger. One drawback of defocusing PIV is the high laser power required due to the small aperture of the holes.

3 Experimental Setup and Procedures

The DTMB 5512(geosym of DTMB 5415) was tested at three different static drift angles: -1°, 10° and 20°, at a Froude number F_N=0.280, which

corresponds to the full-scale cruising speed of the vessel, 20 knots. The corresponding Reynolds number is 4.85×10^6. The full-scale dynamic sinkage and trim at this condition were maintained throughout the experiments, and the tests were conducted in calm-water conditions.

It is a known fact that it is not possible to have similarity of full-scale and model-scale F_N and R_e at the same time. Scaling for the Reynolds number in a towing tank experiment is generally not practical, as it requires very high speeds for a small model, and therefore Froude-scaling is used. This is an issue if one is interested in the behaviour of viscous phenomena such as boundary layer separation and vortex formation, which are R_e-dependent. In this study, however, the problem of Reynolds scale effects is neatly avoided by running the CFD simulations, for which the experimental data is meant to provide a validation basis, for the model geometry and not the full scale ship. In other words, the main concern is prediction capabilities at model-scale, not similarity to full-scale conditions.

The drift angles were chosen based on experience and the experimental capabilities. From earlier experiments in the IIHR towing tank it is known that the ship's global forces and moments at static drift have linear characteristics up to approximately 10°, where they become nonlinear. 20° is the largest angle which permits measurements without notable blockage effects. The choice of the smallest drift angle -1°, is a result of inherent experimental uncertainty. The first sets of measurements were conducted at 0°, which was thought to be the neutral angle. Logically it should be, if it is assumed that the model is completely symmetric and that there is no skew in the setup. However, a certain asymmetry of the flow was observed at 0°. This may be due to various reasons, such as a flaw in the manufacture of the model, causing it to lose perfect symmetry, or inaccuracy in the weight ballasting. The streamlines near the centre-plane and the local velocity were examined for β=0°, -1° and -2°. The tests showed that -1° was in reality closer to the neutral angle than 0°. Later, more rigorous neutral angle tests have been conducted, where it was found that -0.5° is the best approximation. Unfortunately, this was discovered too late for being able to incorporate data for the corrected drift angle in the current work. Also, data for stations x=0.600, 0.800 and 0.935 was not available for -1° at the time this was written. In section 4 data for 0° will be presented for these stations.

The experiments were conducted with a free surface, which is necessary to get the correct forces and moments on the model. Moreover, numerical simulations at a drift angle of 20° show that vortices are induced by the breaking free surface (Bhushan and Stern, 2012). This means that there is interaction between the free surface and the vortex system, which cannot be neglected.

All figures in the current section are from a work report by Yoon et al. (2013).

3.1 Facility

The experiments were conducted in the towing tank facility at IIHR. The towing tank is $100[m]$ long, 3.048 $[m]$ wide and $3.048[m]$ deep, and is equipped with a wave-maker, a drive carriage, a planar motion mechanism (PMM) carriage, a model tracking system, an automated wave damping system and a wave-dampening beach. The drive carriage was instrumented to measure forces, moments, ship model motions and towing speed. The ship motions were registered by means of a infra-red based camera tracking system. The wave-dampening system and beach allow taking measurements with 12 minute intervals between carriage runs, as determined by visual inspection. The uncertainty of the towing tank test procedures was assessed by Longo and Stern (2005).

Figure 18: IIHR towing tank

Tank dimensions	
Length[m]	100
Width[m]	3.048
Depth[m]	3.048

Table 2: Facility overall dimensions.

3.2 Coordinate system

A ship fixed coordinate system is used in this study, with the origin at the mean water line, centreline and forward perpendicular (see fig. 19). z is positive upwards, x is positive towards the after-body, and y is positive towards the starboard side. All coordinates have been normalized by L_{pp}, so that $x = X/L_{pp}$, $y = Y/L_{pp}$ and $z = Z/L_{pp}$.
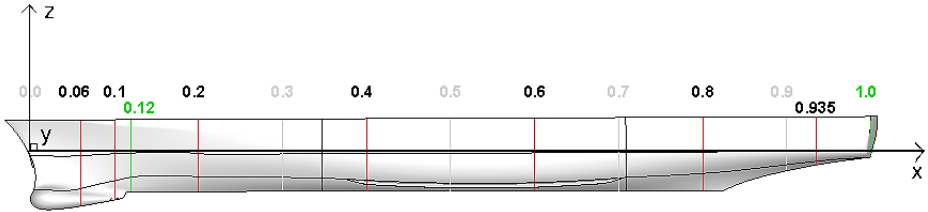
Figure 19: Ship fixed coordinate system.

3.3 Model geometry

The ship model is a DTMB 5512, which is a geosym of the DTMB 5415. It was manufactured at the Naval Surface Warfare Center (NSWC), at scale 1:46.6. The hull is fibre-reinforced plexi-glass with L_{pp}=3.048[m] and a block coefficient C_B=0.506, and it has a transom stern and a sonar dome in the bow. Apart from port and starboard bilge-keels, the model is un-appended, i.e. struts, propulsors, rudders and shafts are excluded from the design. In order to initiate transition to turbulence, cylindrical studs have been placed in a row at x=0.05 . The studs have a height of 1.6[mm], a diameter of 3.2[mm] and are fixed with a spacing of 9.5[mm]. The dimensions and placement of the studs an in accordance with the recommendations of ITTC (2002).

Figure 20: DTMB 5512 ship model. Bilge keels shown in top image.

	Full scale	DTMB # 5415	DTMB # 5512
Scale[-]	1:1	1:24.83	1:46.6
L(L$_{pp}$)[m]	142.0	5.72	3.048
L$_{WL}$[m]	142.18	5.7273	3.052
B$_{WL}$	19.10	0.769	0.410
T$_m$[m]	6.16	0.248	0.132
∇	8472	0.5540	0.0086
Δ	8684	0.5540	0.0086
C$_B$	0.506	0.506	0.506

Table 3: Full scale and model dimensions

The model was first rigidly attached to a fixed mount(see fig. 21), and then ballasted to the dynamic sinkage ($\sigma = 0.192 \times 10^{-2}$L) and trim($\tau =$ -0.136° ;bow down) conditions corresponding to straight-ahead towing at F_N=0.280.
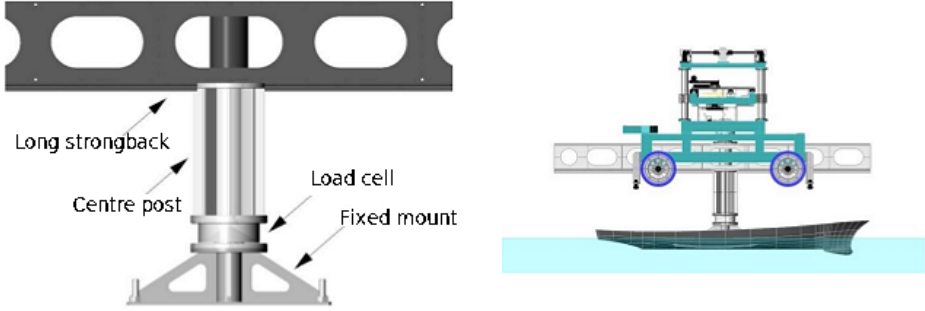
Figure 21: Side views of model mount. Left: fixed-mount. Right: Model mounted on carriage.

3.4   Measurement systems

Carriage Instrumentation

Towing Speed   The carriage towing speed U_T was measured by means of an optical encoder mounted on the carriage wheel. The system, developed at IIHR, consists of the encoder, a pulse counter, an analogue-digital (AD) converter and a PC. The wheel has 8000 small slots, and every time a slot passes the encoder a pulse registers. Thus, the carriage speed is determined by

$$U_T = \frac{n\pi D_w}{a\Delta t}\left(1 + U_B\right) \tag{34}$$

where a is the number of slots on the wheel, D_w is the wheel diameter, Δt is a known time interval and n is the number of counted pulses. U_B is a calibration for blockage from the tank walls, calculated as recommended by ITTC (1978). The linear resolution of the system is $0.15[mm/pulse]$.

Model Forces and Moments   The system for measuring forces and moments on the ship model consists of a six-component Izumi strain-gage type load cell, six Izumi amplifiers, a 16 channel AD converter and a PC. Maximum forces and moments for the load cell consists of $500[N]$ for F_x, F_y and F_z and 50, 50 and $200[Nm]$ for M_x, M_y and M_z respectively. The load cell is statically calibrated after testing, using standard weights.

Forces and moments on the model are not the subject of the current study, but it is noted for future reference that they have been measured

simultaneously with the velocities.

Tomographic PIV system

The tomographic PIV system used in the current study is a towed underwater system delivered by LaVision. Four CCD cameras, enclosed in water-tight cylindrical mounts, henceforth called torpedoes, were used for imaging, and the light source was a double-cavity pulsed Nd:Yag laser. The separation angle between the outer cameras and the measurement volume perpendicular is 20° and 55° respectively. Elsinga et al. (2006) found that in a symmetric four-camera setup, the optimum angle between the outer cameras and the perpendicular was near 30°, in order to increase the reconstruction quality. The sampling rate was restricted by the capability of the cameras, resulting in a rate of $13[Hz]$.

Silver coated hollow glass spheres (SCHGS) with a mean diameter of $d_p=14[\mu m]$, and density $\rho_p=1700[kg/m^3]$ were used as seeding. The particles are not exactly neutrally buoyant, but are observed to settle with time. The Stokes number, defined as

$$Stk = \frac{U_f}{L_0} \cdot \frac{\rho_p d_p^2}{18\mu_f}, \tag{35}$$

can be used as a measure of tracer particle fidelity. Here U_f is the incident fluid velocity, μ_f is the fluid dynamic viscosity, and L_0 is the characteristic length scale of an obstacle in the flow, for example the diameter of a circular cylinder. Stk is the ratio between the characteristic time scale of the flow versus that of the tracer particles. $Stk \ll 1$ signifies good tracer fidelity, whereas $Stk \gg 1$ means that the particles detach from the flow. For practical purposes, $Stk < 0.1$ gives acceptable flow tracer accuracy with an error smaller than 1% (McKeon et al., 2007). In our case, the ship model L_{pp} is the characteristic length scale, and the nominal towing speed is the outer velocity scale. This gives

$$Stk = \frac{U_{T0}}{L_{pp}} \cdot \frac{\rho_p d_p^2}{18\mu_f} = \frac{1.530}{3.048} \cdot \frac{1700 \cdot (14 \cdot 10^{-6})2}{18 \cdot 1.002 \cdot 10^{-3}}[-] \approx 9.2734e-06. \tag{36}$$

Stk is significantly lower than unity, which means that the SCHGS can be expected to give a good representation of the actual flow. The choice of

length scale and outer velocity scale influences *Stk*, and is not necessarily straight forward. As the streamwise vortices along the hull are the primary focus of study, we might also choose the nominal diameter of for example the SDV as the length scale. The vortex diameter is in the order of $5[mm]$. Inserting $L_0 \sim 5 \cdot 10^{-3}$ in equation 36 gives $Stk \sim 0.006$, which is still well below practical limit $Stk < 0.1$.

Uniform flow tests have been conducted in order to compare the TPIV measurement with the measured towing speed. The test were performed in straight-ahead condition without the ship model. Only the first 12 images were used to compute the velocities (Yoon et al., 2013). The results are shown in table 5.The error of the streamwise component averaged over all tests is 1.8%, for the horizontal and vertical spanwise components, the averaged errors are 1.1% and 0.8% respectively. Ideally, there should be no spanwise velocities in the freestream condition.
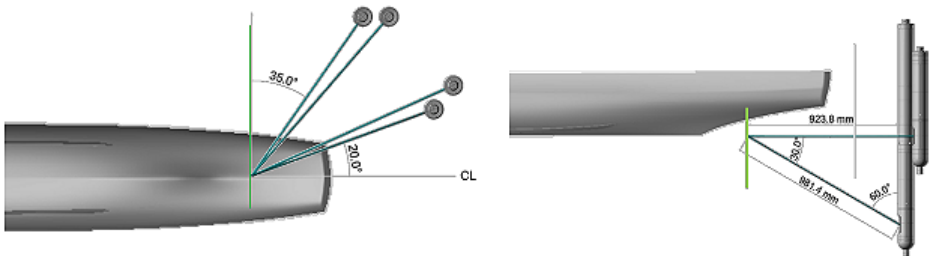
Figure 22: Left: Camera mount seen from below. Right: Side-view of camera mount.

TPIV System	
Camera:	Imager Pro sX 5M
Chip type	CCD
Pixel resolution $[px]$	2456×2058
Frame Rate$[Hz]$	13
Laser:	Nd:Yag
Power$[mJ/pulse]$	190
Max. pulse rate	$15[Hz]$
Housing:	Vertical Cylinder
Diameter$[mm]$	90
Distance from measurement volume$[mm]$	≈ 950
Measurement Volume$[mm^3]$	$100 \times 100 \times 10$
Software	DaVis8

Table 4: Specification of TPIV system

Test no.	$U_T[m/s]$	$\overline{U}[m/s]$	$\overline{V}[m/s]$	$\overline{W}[m/s]$
1	0.345	0.346	-0.011	-0.003
2	0.685	0.649	-0.002	0.005
3	1.021	1.002	0.004	0.002
4	1.355	1.332	0.007	0.008
5	1.533	1.520	0.014	0.022
6	1.682	1.664	0.018	0.017

Table 5: Results from freestream TPIV measurements compared to U_T

3.5 Notes on the Data Post-Processing

Post-processing of the raw images has been done by means of LaVision's software DaVis 8.1. For details about the software routines, please refer to the DaVis8.1 product manual. Although the post-processing routines will not be elaborated here, some notes about filtering should be made, as application of such clearly effects the result.

After the raw vector field has been obtained, the velocity field still has a number of outliers, particularly in vicinity of the hull, and at the vortex core. Insufficient resolution at the vortex core is a known problem

in PIV in general, as particles that are not exactly neutrally buoyant tend to be dispersed away from the core. It is beneficial to filter out as many of these outliers as possible, but without losing actual vectors. First a local median filter is applied. This filter compares the magnitude and direction of a vector to its neighbours, and rejects the vector is the difference is above a certain tolerance.

After the application of the median filter, there is still an unacceptably high number of outliers in the field. This is because the median filter will not work if a sufficient number of outliers are clustered together. Global filters can get rid of spurious vectors. First, a requirement is imposed that all vectors have positive values of the streamwise velocity component. This is reasonable, as no backflow is expected at this drift angle and F_N. Secondly, the time mean and standard deviation of the velocity is calculated at each point in the field. A requirement is set that the velocity can be no larger than the mean $\pm$ 4.5 times the standard deviation. This should give us a confidence of 95% for a random dataset with an unknown distribution.

3.6   Normalizing of velocities

In this work, all velocities have been normalized by U_T. In section 4, the overview plots of all stations have been normalized by the nominal towing speed U_{T0}=1.530$[m/s]$. Data from the measurement zone containing the SDV of β=20° has been normalized according to table 8.

Mean values are presented in section 4.1.1. For each drift angle, five measurement series were taken, and the mean data fields have been computed by first time-averaging each measurement series, and subsequently taking the ensemble average of all five series. β=-1° and 10° have been normalized according to table 7 and 6 respectively.

Run01	Run02	Run03	Run04	Run05
1.52977809	1.53104921	1.53053513	1.52833477	1.52808139

Table 6: Mean towing speed $[m/s]$, SDV zone, β=10°, x=0.400.

Run01	Run02	Run03	Run04	Run05
1.536	1.536	1.536	1.537	1.534

Table 7: Mean towing speed [m/s], SDV zone, β=-1°, x=0.400.

	Run01	Run02	Run03	Run04	Run05
x=0.060	1.53445599	1.53510768	1.53237559	1.53536398	1.53455601
x=0.100	1.53600886	1.53345299	1.53433440	1.53305160	1.53173784
x=0.120	1.53441740	1.53160215	1.53438531	1.53444594	1.53630894
x=0.200	1.53036993	1.53054469	1.52855978	1.53201051	1.53160588
x=0.400	1.529	1.531	1.530	1.530	1.515
x=0.600	1.52553568	1.53063266	1.52482547	1.52875091	1.52841866

Table 8: Mean towing speed [m/s], SDV zone β=20°.

4 Results and Discussion

First an overview of the flow behaviour along the hull will be given for all drift angles, then the measurement station x=0.400 will be treated in detail. The volume analysis from that station will serve as a guide for further work, beyond the current study.

To be consistent with the naming conventions from earlier studies, for β = 10° and 20°, vortices originating from the starboard side will be dubbed leeward (LW) vortices and vortices originating from the port side will be dubbed windward (WW).

$\beta = -1°$

Figure 23 gives an overview of the vortex progression for stations x=0.06 - 0.400. The progression of the SDV alone is shown in figure 24. 2D streamlines of β=-1° for stations x=0.060 - 0.935 are shown in figures 25 - 32, and streamlines superimposed on the Q=100 iso-surface, coloured by H_N, for stations x=0.060 - 0.800 are found in figures 33 - 39. Looking at the 2D streamlines we find no indication of vortices at the first two stations. However, the Q iso-surfaces of x=0.100 reveal a vortical structure separating from the sonar dome, called the sonar dome vortex (SDV). CFD

simulations predict the inception of the SDV at approximately x=0.065 (Bhushan et al., 2013) at this drift angle. However, because of the laser reflections from the model, which decreases resolution close to the hull surface, the TPIV measurement is not able to detect the vortices until they have separated from the hull. This means that the exact inception point of the SDV is impossible to determine in the current experimental work.

At x=0.120 the 2D streamlines show that two vortices have has separated from the hull, both assumed to be SDV's. At the neutral angle the flow is symmetric, so we expect one vortex to form at either side of the sonar dome. The fact that we can see two vortices indicates that -1° is not the true neutral angle. If it were we should only see one when looking at the starboard half of the hull. A third vortex is also observed, which has the same rotation as the starboard SDV. This is called the fore-body keel vortex (FBKV), and it is weaker than the SDV. The elliptic shape stream-line patterns of the FBKV and the starboard side SDV, observed both at x=0.120 and x=0.200 , indicate that they could be merging (Meunier et al., 2005). Indeed, at the next measurement station x=0.400 the FBKV is no longer detected. We cannot be sure, however, that a merging event has taken place. It could also be that the weaker FBKV has dissipated due to the presence of the strong SDV. CFD analysis does show that the SDV and FBKV wrap around each other and merge eventually, but to de-termine exactly what has happened, we would need a better measurement resolution along the x-axis. That means more measurement stations in between the existing ones.

At x=0.400 we observe the starboard SDV as well as parts of the port-side SDV. Whereas we expect these vortices to be a side-by-side counter-rotating pair, we observe that the port-side vortex is displaced along the z-axis. This is assumed to be a result of asymmetry (which is, after all, the reason for observing both vortices in the first place), which causes a slight crossflow, pushing the port side SDV downwards, away from the hull. CFD results and experimental data from INSEAN predict the presence of a second vortex beside SDV at this station(see Appendix A), but this vortex cannot be seen from the streamlines in the current study. However, when advancing to the volume flow analysis, we shall see that the Q iso-surfaces reveal a structure which could be a weak vortex with the same rotation as

the SDV (see fig. 130). Moving on to x=0.600 we observe that a vortex has started forming at the bilge keel, the so-called bilge-keel vortex (BKV). The sonar dome vortex is still clearly present. At stations x=0.800 and 0.935 the streamlines no longer reveal any clear vortical structures. We assume that both the SDV and the much weaker BKV have dissipated at this point. Please note that for stations x=0.600, 0.800 and 0.935 the available data is at a drift angle of 0°.
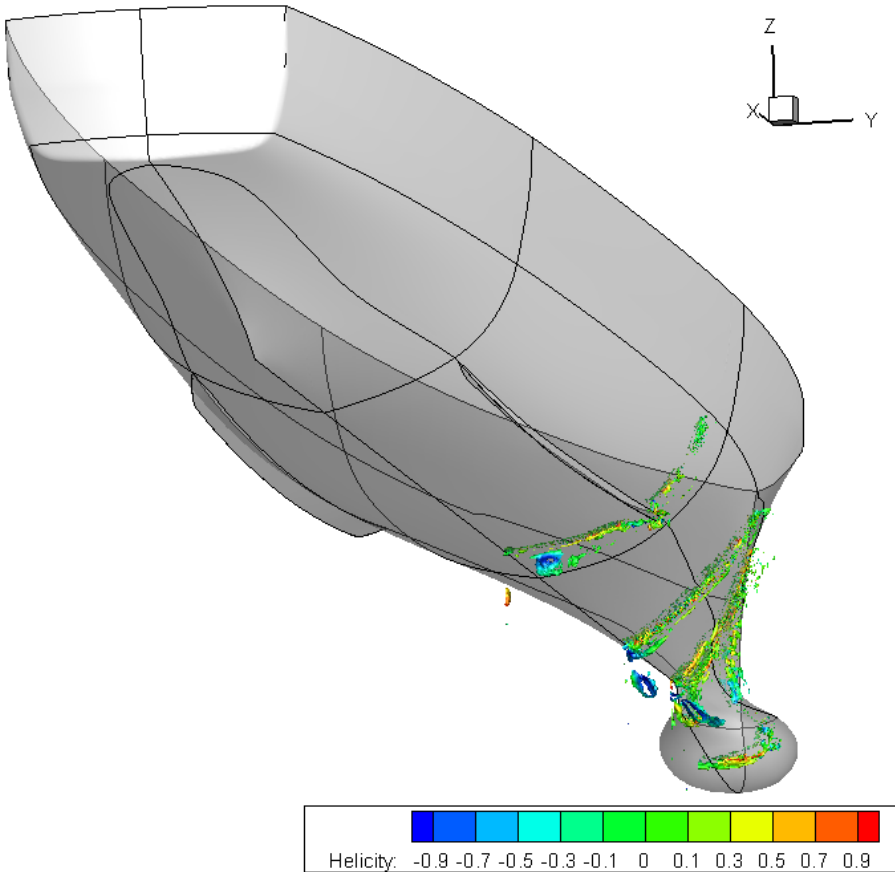
Figure 23: Overview of vortices from x=0.060-0.400. Iso-surfaces of Q=100, coloured by H_N, $\beta = -1°$.
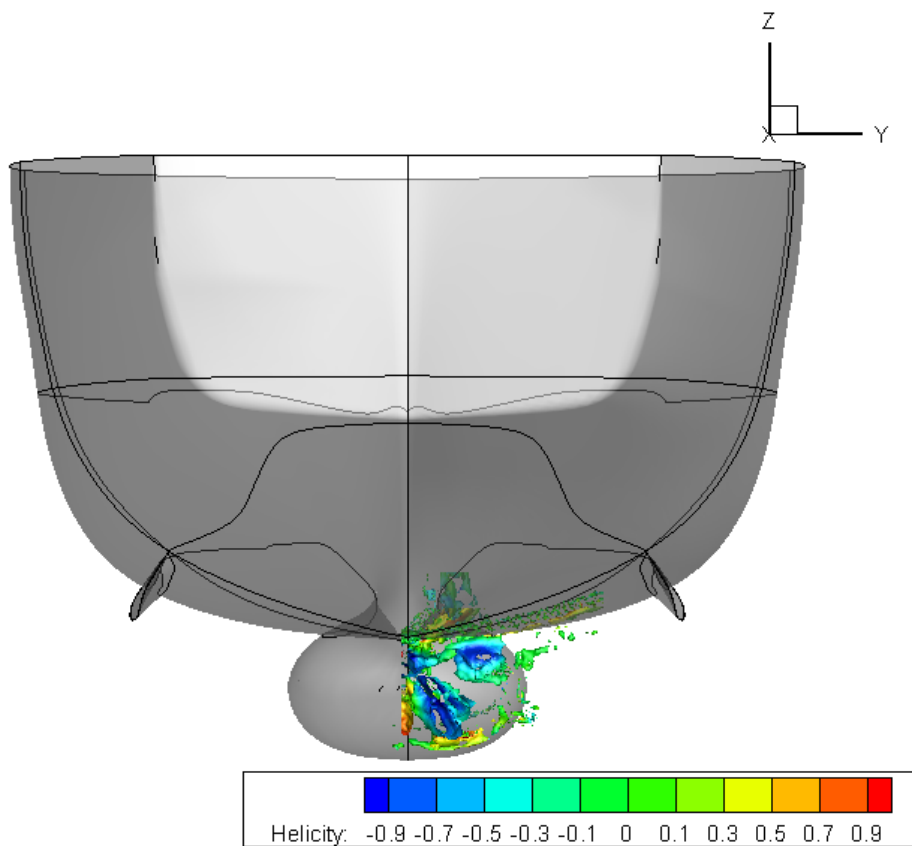
Figure 24: Overview of SDV progression from x=0.060-0.400. Iso-surfaces of Q=100, coloured by H_N, $\beta = -1°$.
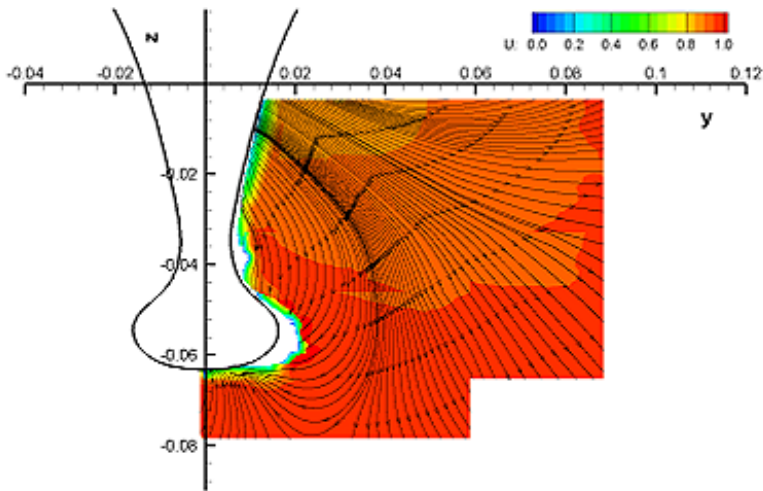
Figure 25: $\beta = -1°$ 2D streamlines at x=0.060.
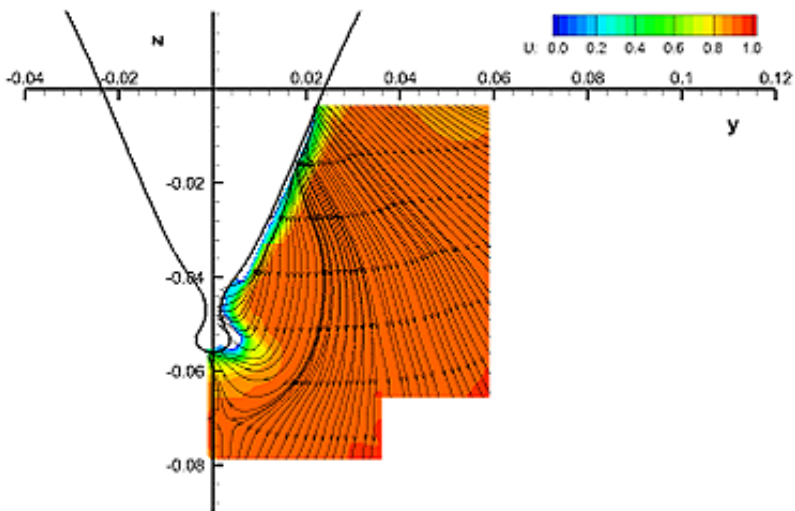
Figure 26: $\beta = -1°$ 2D streamlines at x=0.100.
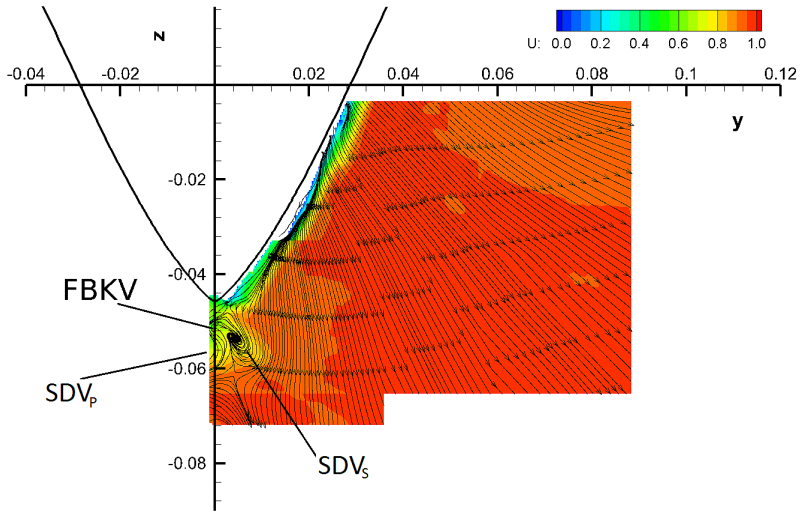
Figure 27: $\beta = -1°$ 2D streamlines at x=0.120.
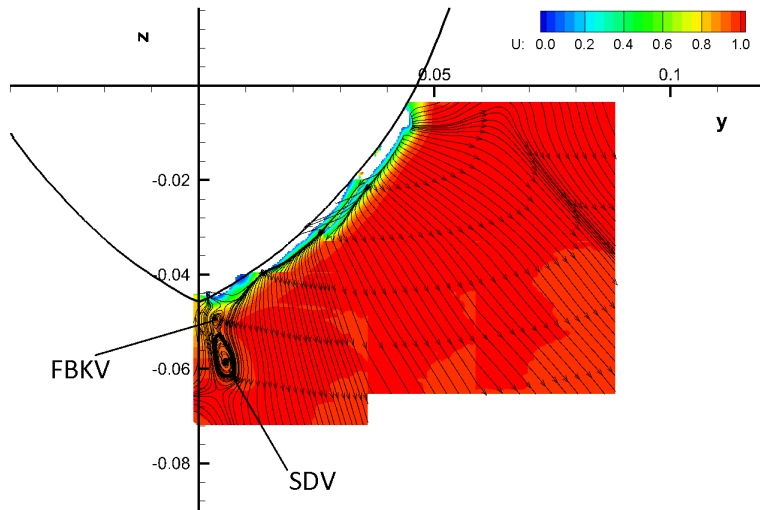
Figure 28: $\beta = -1°$ 2D streamlines at x=0.200.
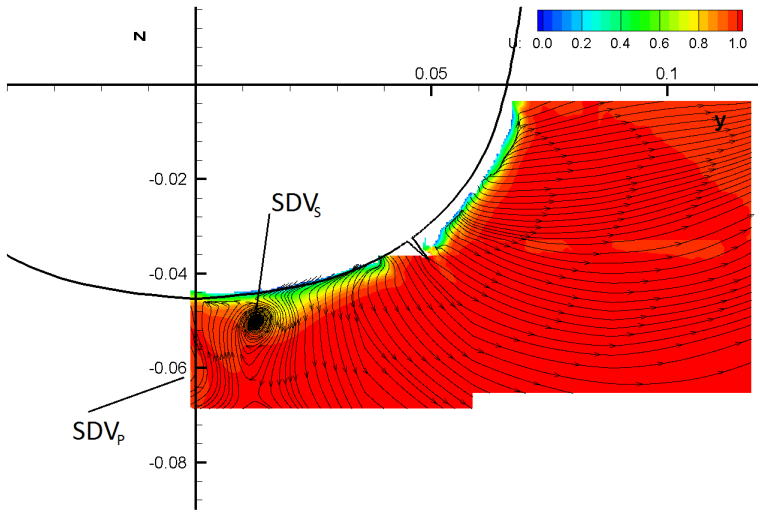
Figure 29: $\beta = -1°$ 2D streamlines at x=0.400.
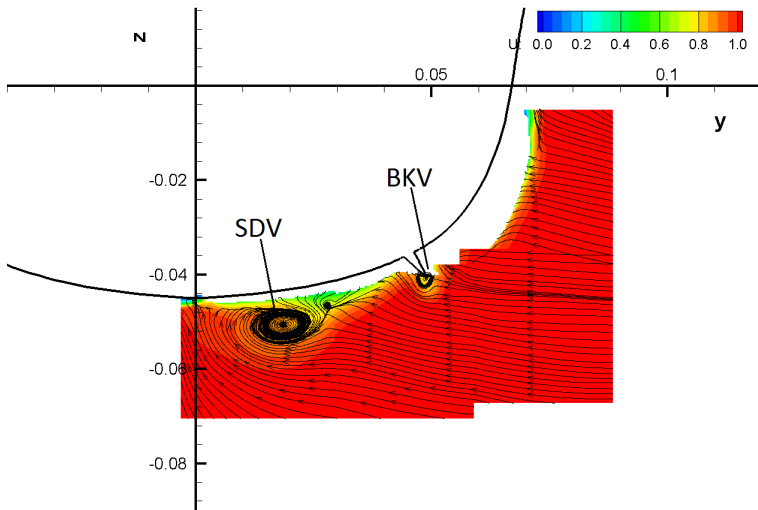
Figure 30: $\beta = 0°$ 2D streamlines at x=0.600.
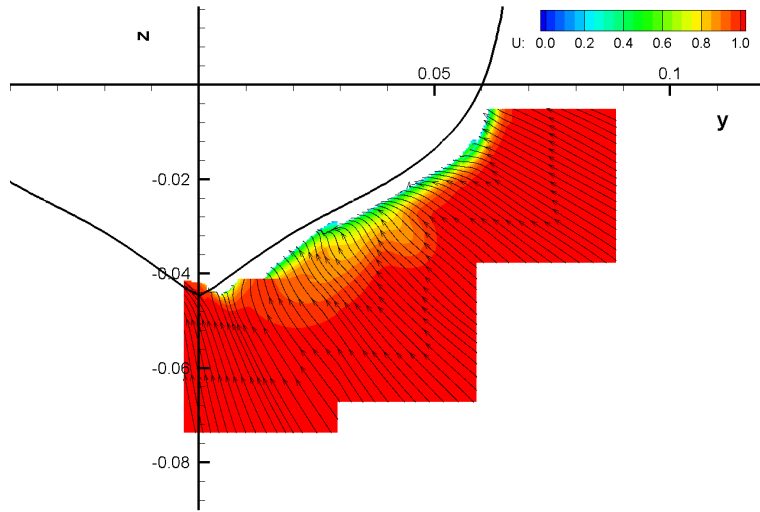
Figure 31: $\beta = 0°$ 2D streamlines at x=0.800.
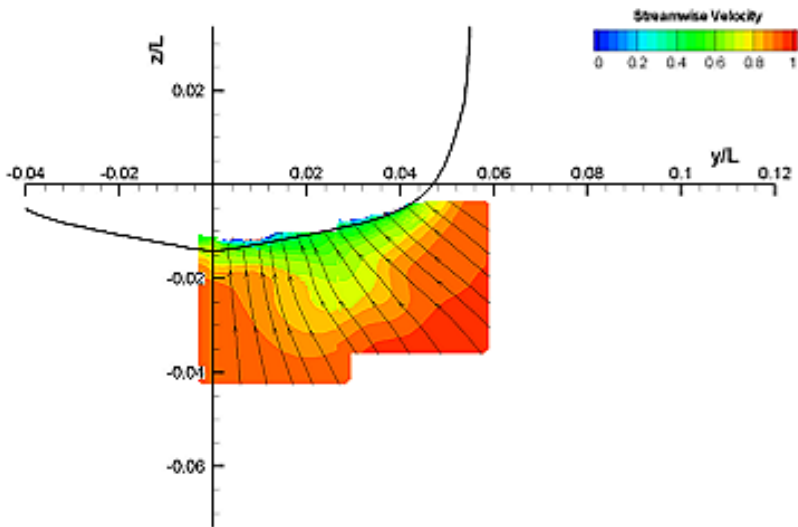
Figure 32: $\beta = 0°$ 2D streamlines at x=0.935.
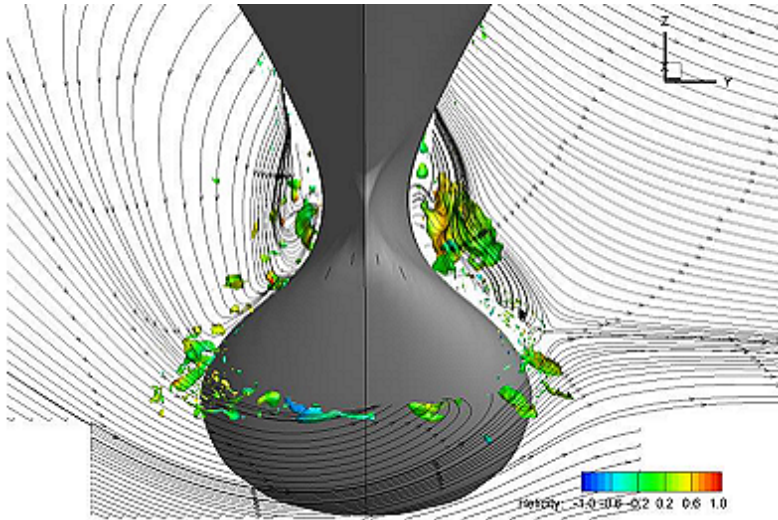
Figure 33: $\beta = -1°$ streamlines with iso-surfaces of Q=100, coloured by H_N. x=0.060.
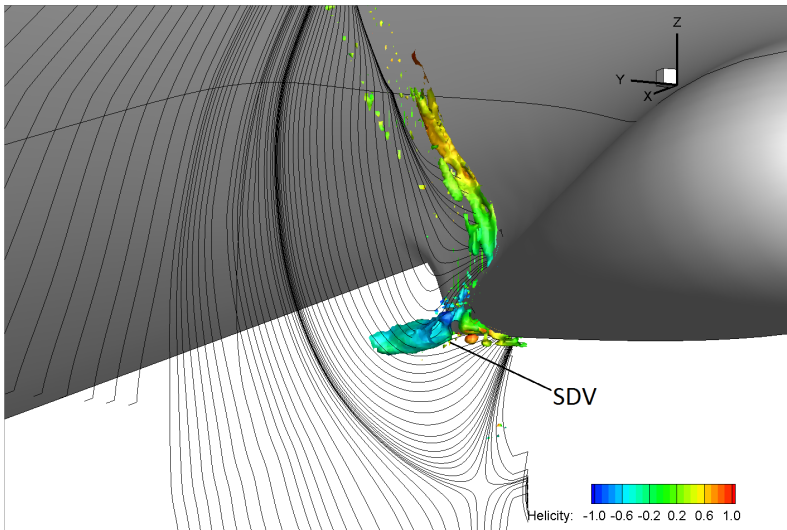
Figure 34: $\beta = -1°$ streamlines with iso-surfaces of Q=100, coloured by H_N. x=0.100.
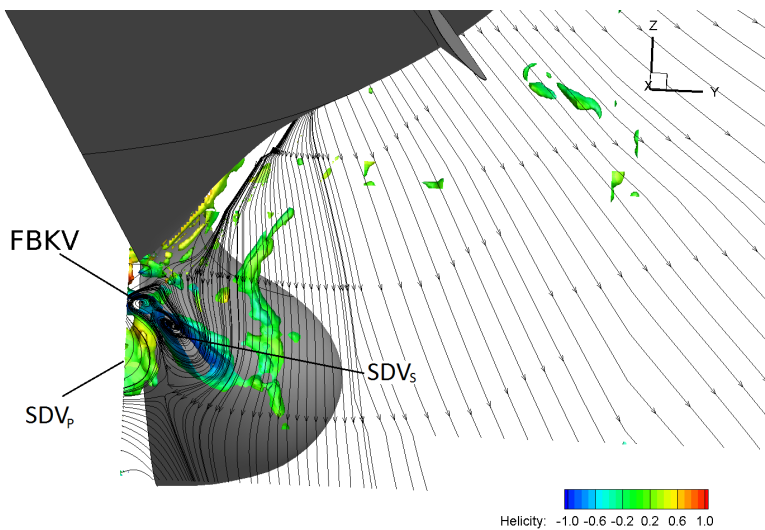
Figure 35: $\beta = -1°$ streamlines with iso-surfaces of Q=100, coloured by H_N. x=0.120.
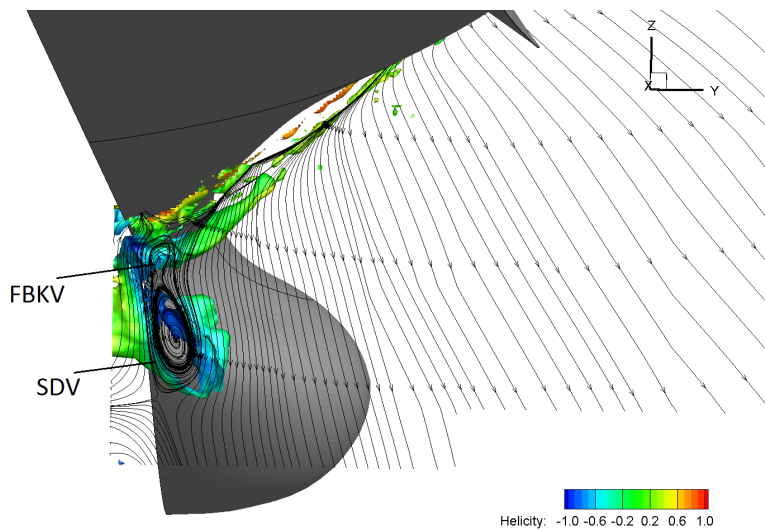
Figure 36: $\beta = -1°$ streamlines with iso-surfaces of Q=100, coloured by H_N. x=0.200.
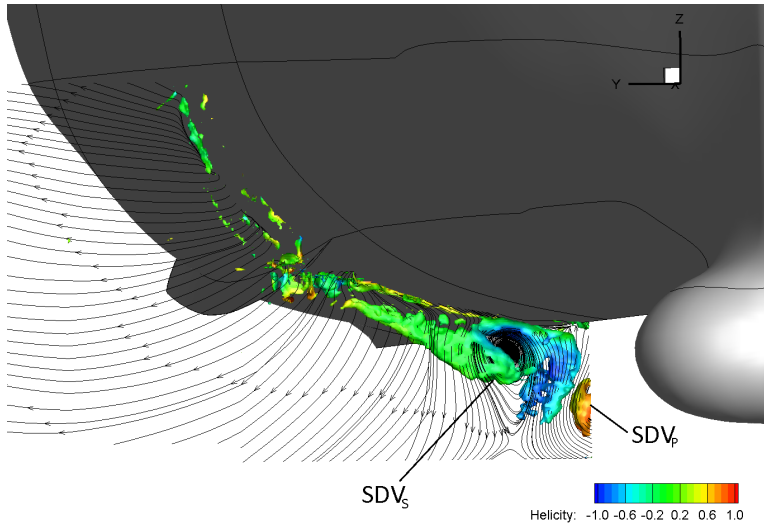
Figure 37: $\beta = -1°$ streamlines with iso-surfaces of Q=100, coloured by H_N. x=0.400.
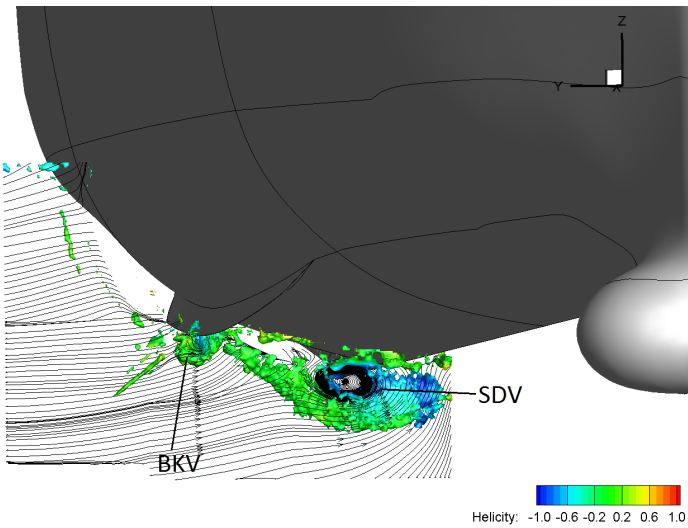
Figure 38: $\beta = 0°$ streamlines with iso-surfaces of Q=100, coloured by H_N. x=0.600.
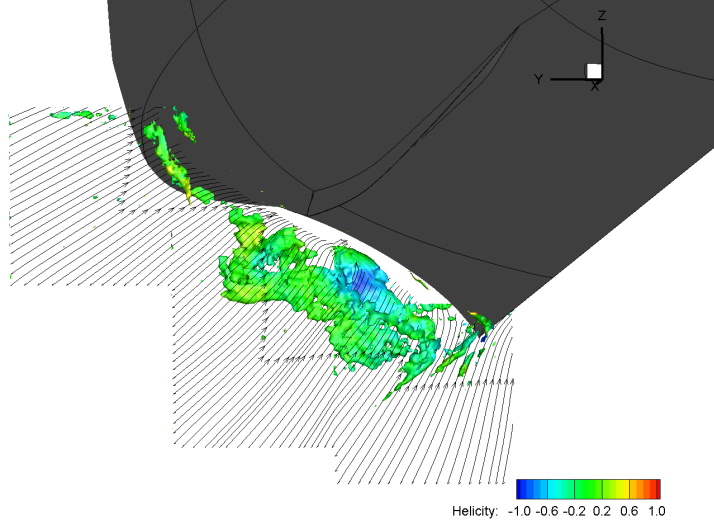
Figure 39: $\beta = 0°$ streamlines with iso-surfaces of Q=100, coloured by H_N. x=0.800.

$\beta = 10°$

Figure 40 gives an overview of the vortex progression along all stations. The progression of the SDV alone is shown in figure 41. 2D streamlines of β=10° for stations x=0.060 - 0.935 are shown in figures 42 - 49, and streamlines superimposed on the Q=100 iso-surface, coloured by H_N, are found in figures 50 - 57.

For x=0.060 there are no clearly observable vortical structures, but as we move on to x=0.100 we see two vortices forming on the sonar dome. It is interesting to note that whereas the SDV's for β=-1° were counter-rotating, the separate SDV's of β=10° have the same rotation. This is due to the strong crossflow occurring at larger drift angles. It can also be observed that the leeward vortex appears to be stronger than the windward one, which is subjected to considerable strain from the crossflow. The SDV's remain separate until downstream of x=0.120. At x=0.200 they have merged into one vortex.

At x=0.600 the leeward BKV is only just visible from the 2D stream-lines, but it cannot be seen at any other stations. The strength of the

BKV is considerably lower than the SDV, so it is assumed that its immediate proximity to the SDV causes it to either be swallowed by the stronger vortex as it departs from the hull, or simply dissipate. Interestingly, the Q=100 iso-surfaces show another vortex below the BKV, rotating in the opposite direction of the SDV, which is not at all indicated by the streamlines. Whether or not this is an actual structure would be better determined by doing a detailed measurement of the area. As mentioned in section 2.1, the Q-criterion requires that the user sets a threshold above which the structures revealed are assumed to be real vortices. The danger of setting a relatively low threshold is that background noise could be perceived as weak vortical structures. As we move downstream along the hull, we see that the SDV moves away from the centreline of the hull. At the same time, vortices generated on the port side of the hull move towards the centreline. At x=0.935 we observe that the port-side bilge keel vortex has migrated towards the centreline and is now present in our field-of-view. In addition we observe another vortex, which is not observed at any other station. Judging by its relative position to the centreline it is assumed that it this vortex is generated by the cross-flow over the after-body keel, so it shall be called the after-body keel vortex (ABKV). Had it been generated further upstream, one must assume that the offset with respect to the centreline would have been larger (as for the SDV). Unfortunately, there is no available CFD analysis for comparison at this point, so this should be included in future work.
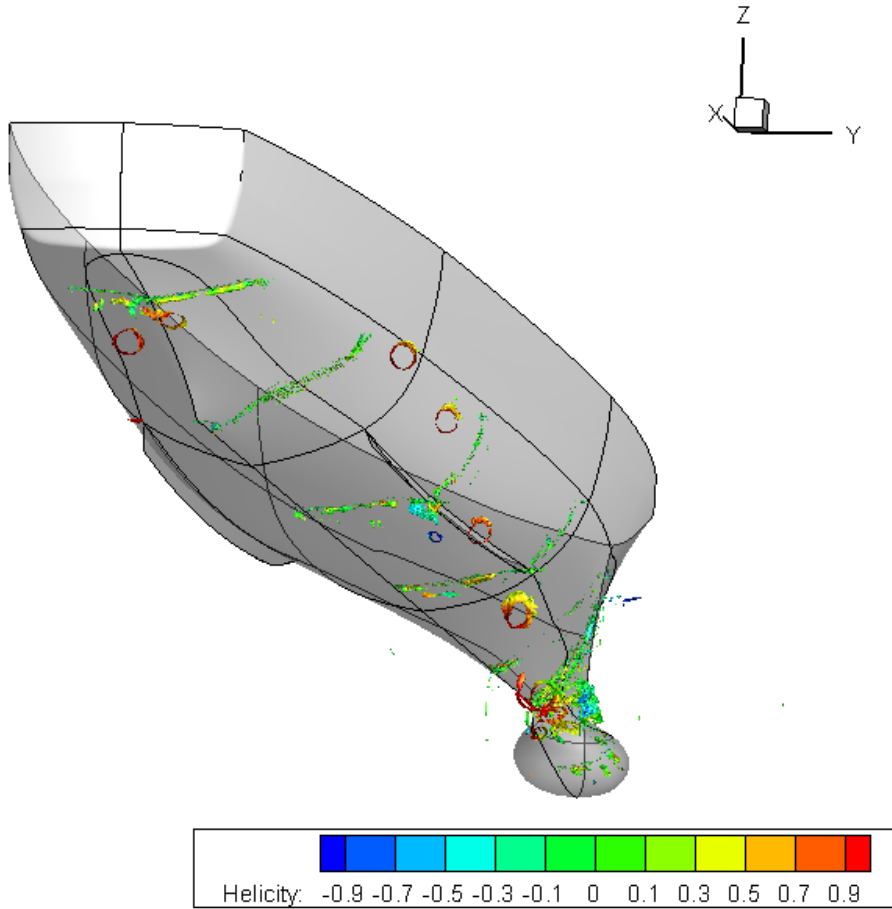
Figure 40: Overview of vortex progression. Iso-surfaces of Q=100, coloured by H_N, $\beta = 10°$.
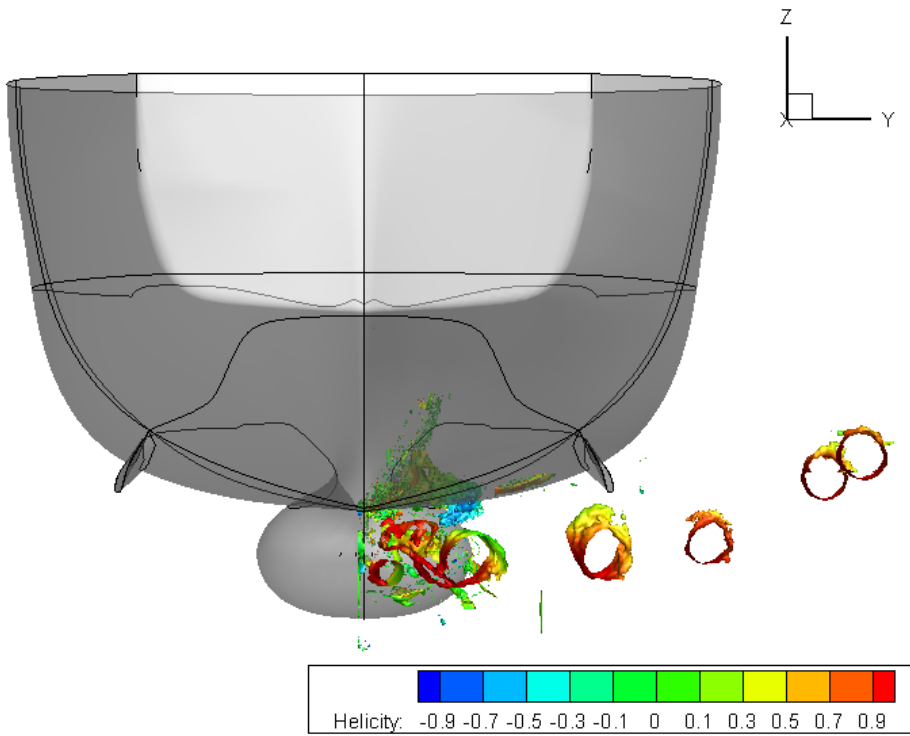
Figure 41: Overview of SDV progression. Iso-surfaces of Q=100, coloured by H_N, $\beta = 10°$.
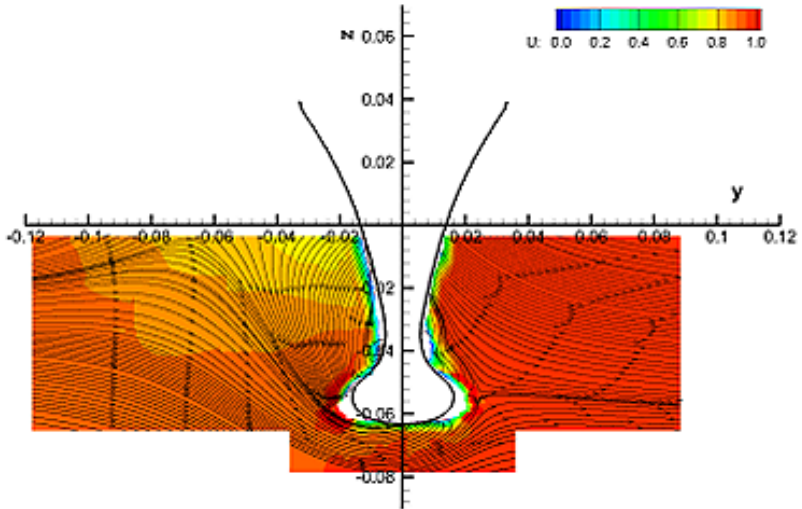
Figure 42: $\beta = 10°$ 2D streamlines x=0.060.
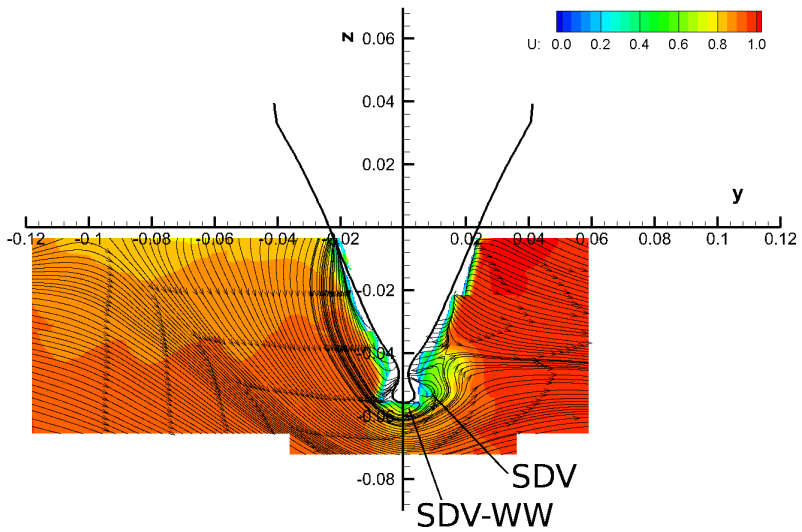
Figure 43: $\beta = 10°$ 2D streamlines x=0.100.
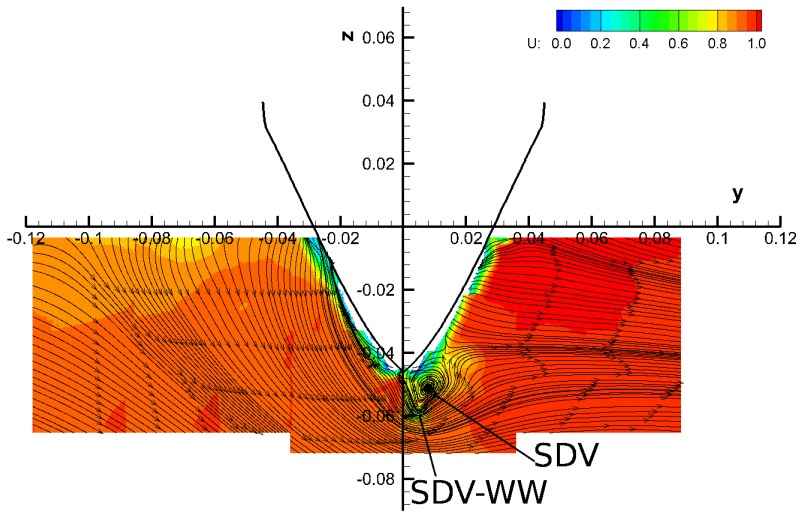
Figure 44: $\beta = 10°$ 2D streamlines x=0.120.
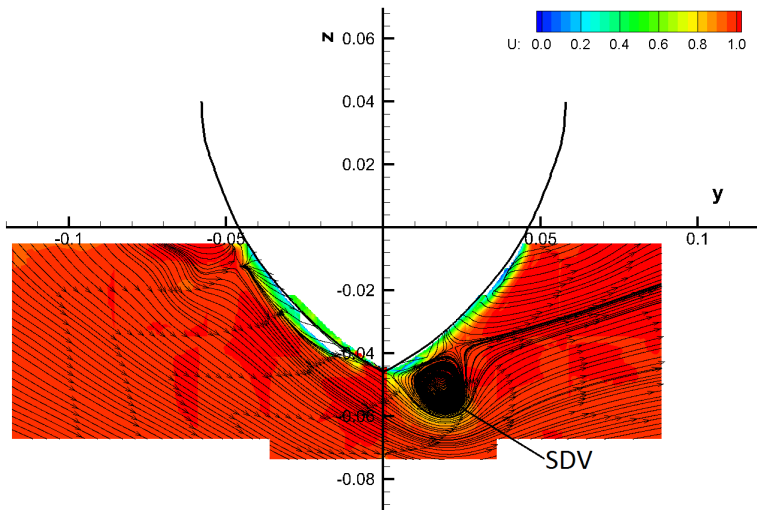
Figure 45: $\beta = 10°$ 2D streamlines x=0.200.
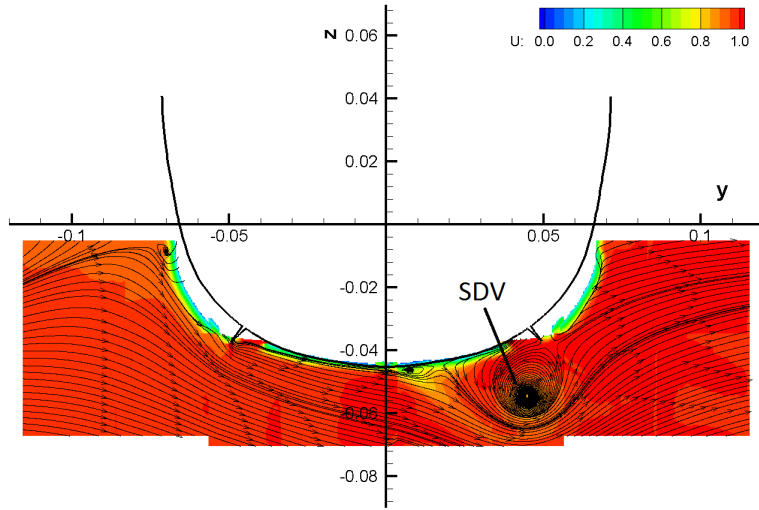
Figure 46: $\beta = 10°$ 2D streamlines x=0.100.
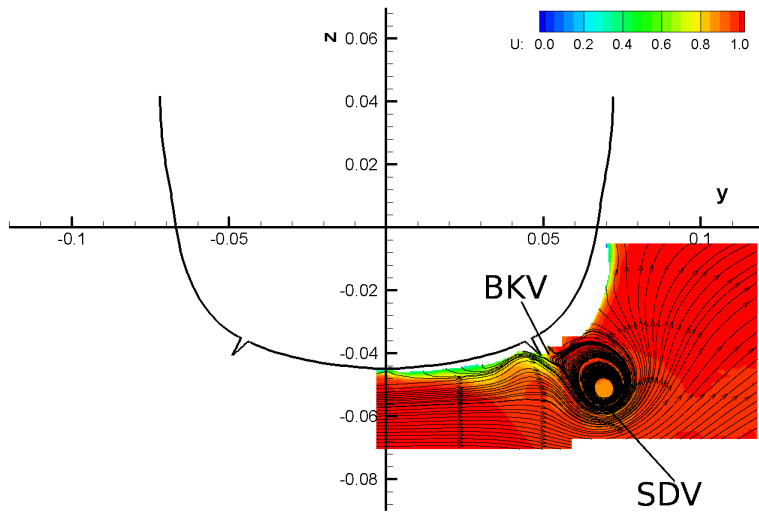
Figure 47: $\beta = 10°$ 2D streamlines x=0.600.
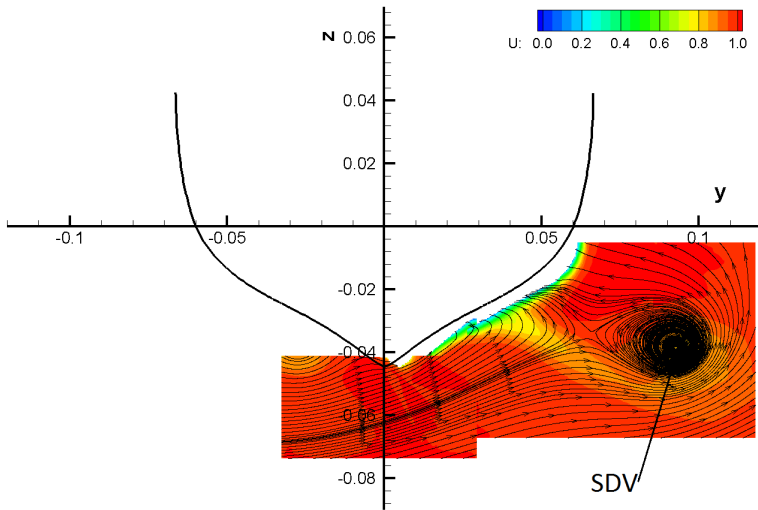
Figure 48: $\beta = 10°$ 2D streamlines x=0.800.
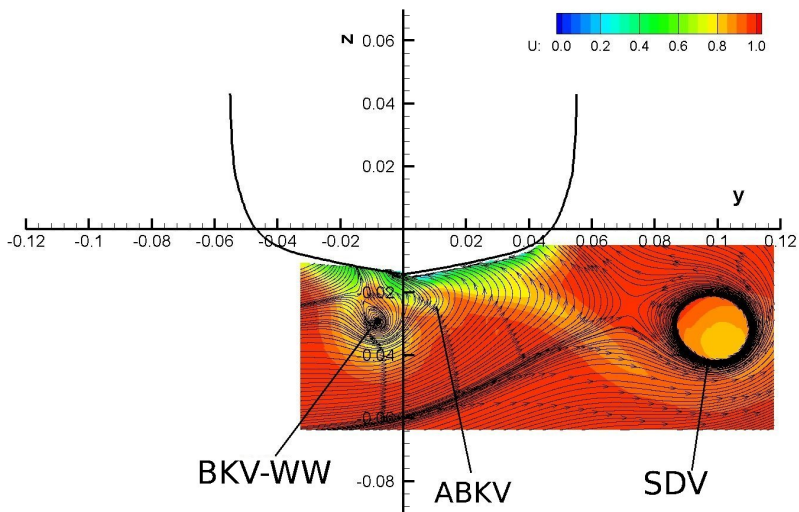
Figure 49: $\beta = 10°$ 2D streamlines x=0.935.
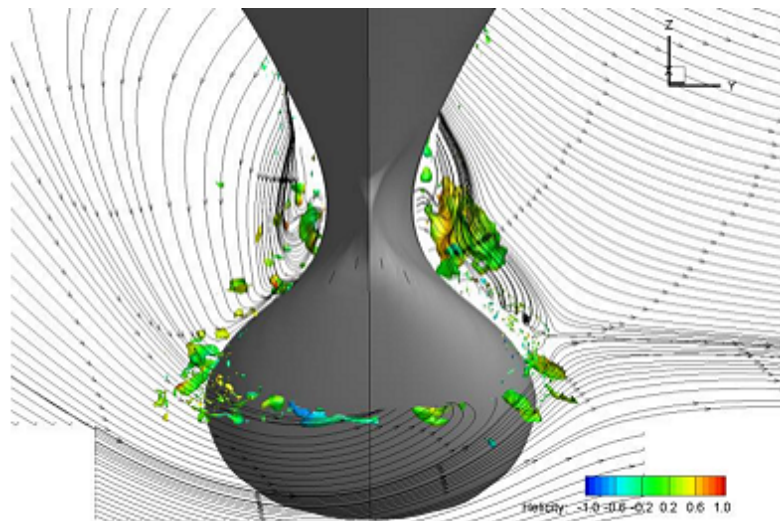
Figure 50: $\beta = 10°$ streamlines with Q=100 iso-surfaces, x=0.060.
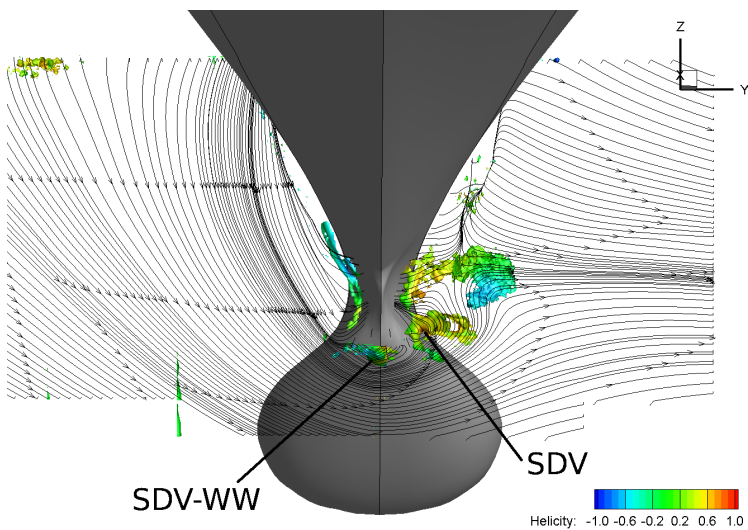
Figure 51: $\beta = 10°$ streamlines with Q=100 iso-surfaces, x=0.100.
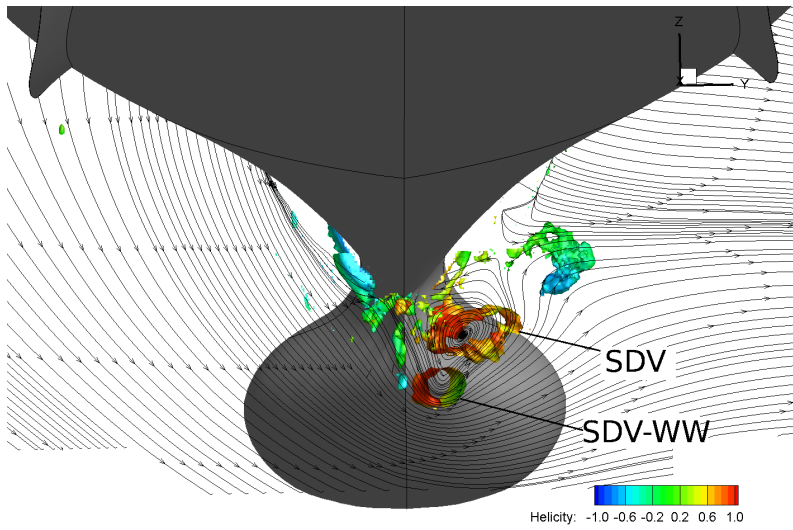
Figure 52: $\beta = 10°$ streamlines with Q=100 iso-surfaces, x=0.120.
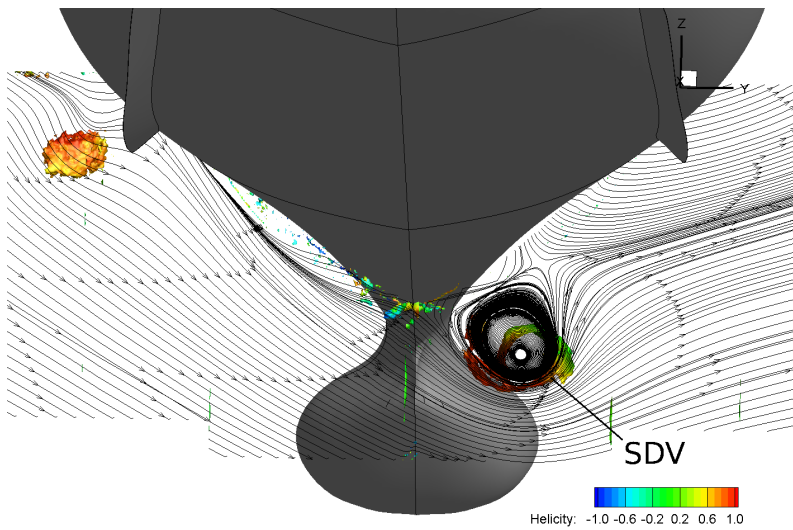
Figure 53: $\beta = 10°$ streamlines with Q=100 iso-surfaces, x=0.200.
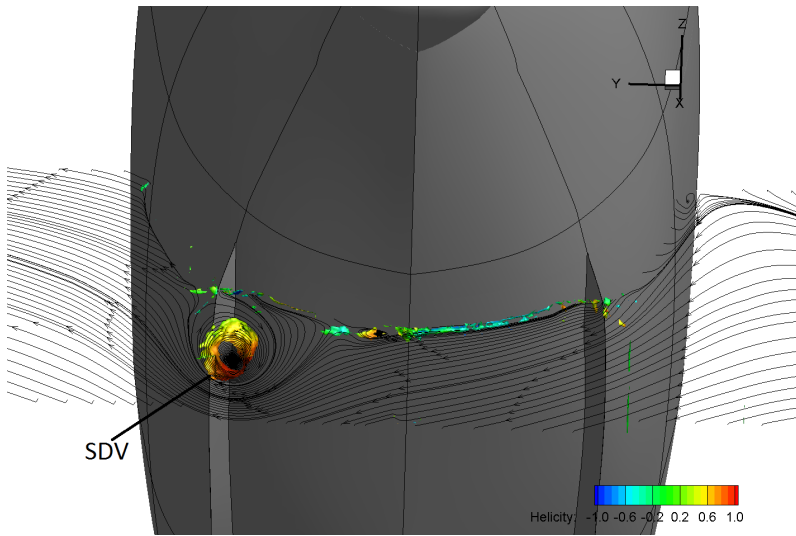
Figure 54: $\beta = 10°$ streamlines with Q=100 iso-surfaces, x=0.400.
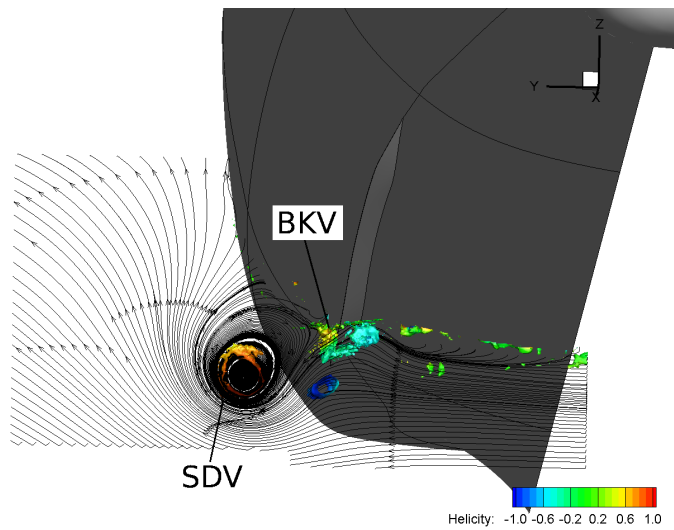
Figure 55: $\beta = 10°$ streamlines with Q=100 iso-surfaces, x=0.600.
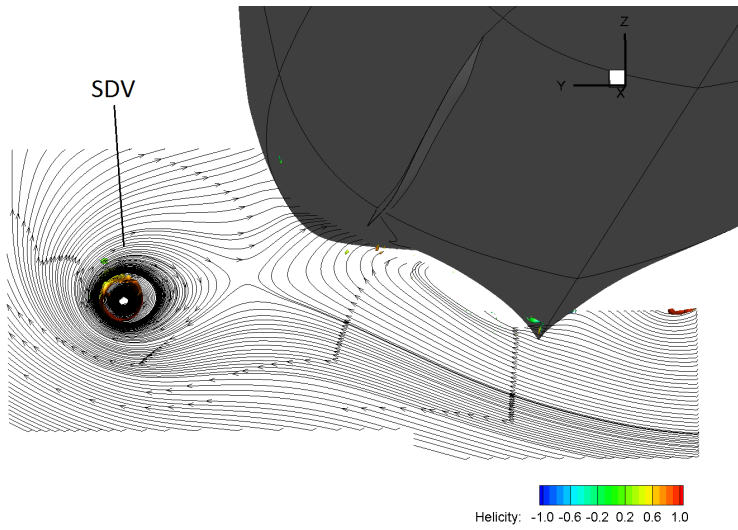
Figure 56: $\beta = 10°$ streamlines with Q=100 iso-surfaces, x=0.800.
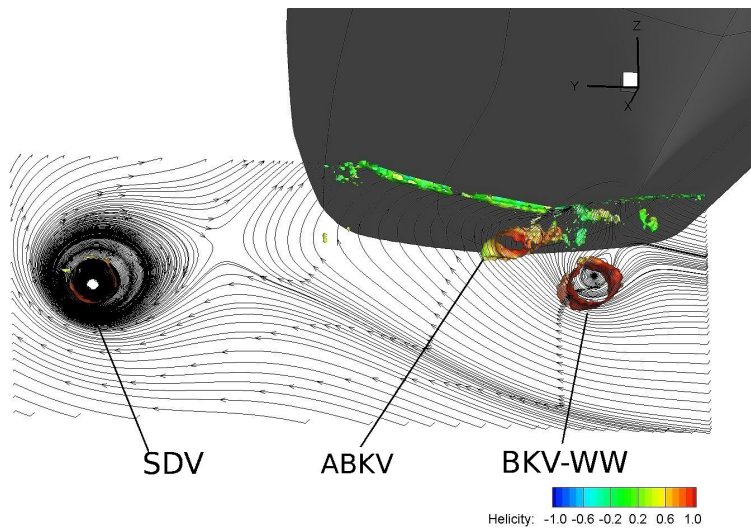
Figure 57: $\beta = 10°$ streamlines with Q=100 iso-surfaces, x=0.935.

$\beta = 20°$

Figure 58 gives an overview of the vortex progression along all stations. The progression of the SDV alone is shown in figure 59. 2D streamlines of β=20° for stations x=0.060 - 0.935 are shown in figures 60 - 67, and streamlines superimposed on the Q=100 iso-surface, coloured by H_N, are found in figures 68 - 75.

Although very weak, the streamlines and Q iso-surfaces indicate the presence of a vortex at x=0.060, which might be the SDV. However, the measurement uncertainty close to the hull is rather large. Also, as we shall come back to in section 4.2, recent CFD analysis suggests that the inception of the SDV occurs close to x=0.080, from which it follows that the observed vortex structure might be something else. At x=0.100 the SDV is clearly visible, and separated from the hull. Only one vortex is observed, so it can be assumed that the windward SDV is rapidly dissipated due to the strain from the strong crossflow.

Only the SDV is completely clear from the 2D streamlines at x=0.200, but looking at the combined streamlines and Q iso-surfaces in figure 71 the streamlines indicate the early formation of two vortices, the wind-and leeward FBKV's. Further downstream, at x=0.400, these structures are quite clear. In addition, we observe vortices at both bilge keels. Contrary to the neutral angle, the leeward FBKV has opposite rotation to the SDV.

At x=0.600 the FBKV's are no longer visible, but we still see the leeward bilge keel vortex. Its rotation seems to be changed from x=0.400, and it now has the same rotation as the SDV. Intuitively, this rotational direction makes sense with respect to the flow from the port-side across the bilge keel. The direction at x=0.400 can be attributed to the close proximity of the FKBV. At x=0.800 BKV-WW is moving towards the centreline. The 3D Q iso-surfaces also indicate the formation of a vortex at the after-body keel. The vortex observed at x=0.935 is believed to be this ABKV, merged with the BKV-WW. Because of the high drift angle, the SDV moves away from the hull quite quickly as we move downstream. At x=0.200 it already has an appreciable offset, and at x=0.800 it has almost entirely disappeared from our field-of-view. Only the outer streamlines are visible, which means more measurements are needed to determine its characteristics at the far downstream stations. From the streamlines at x=0.600-0.935 it looks as though we see a vortex in the upper star-

board corner of the measurement domain. This is believed to result from measurement noise due to the presence of the free surface.
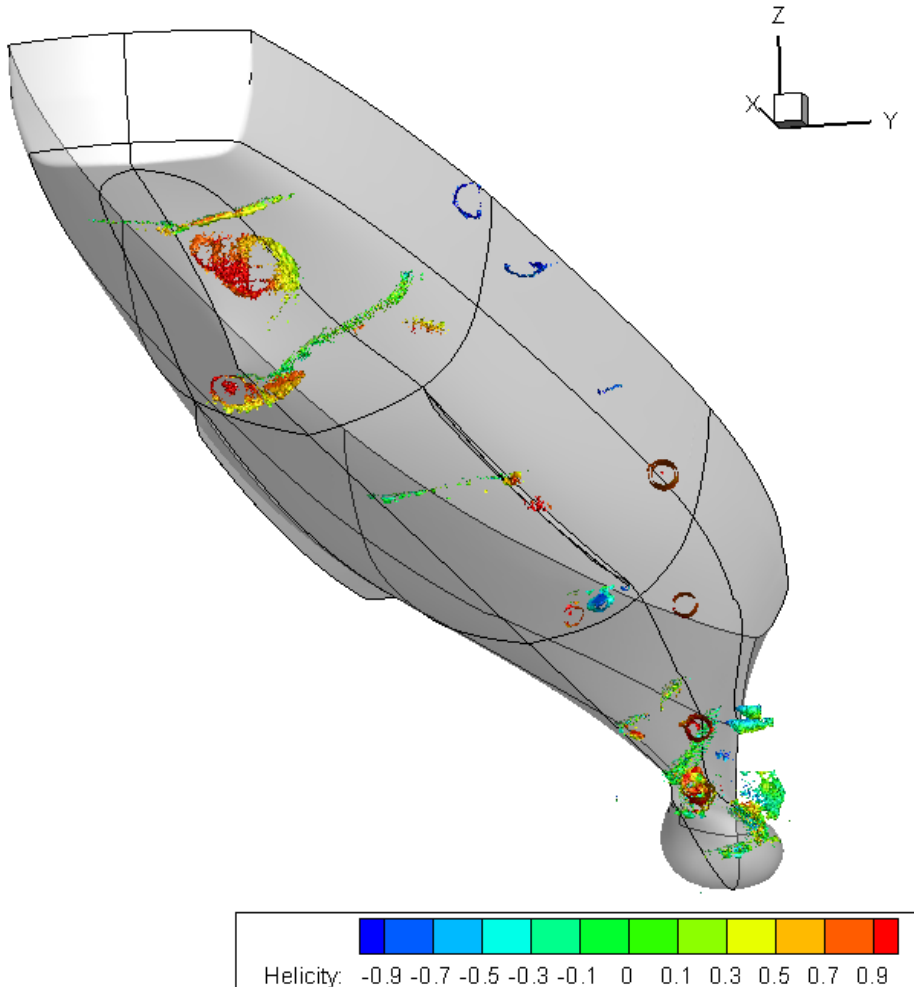
Figure 58: Overview of vortex progression. Iso-surfaces of Q=100, 1000 and 10 000, coloured by H_N, $\beta = 20°$.
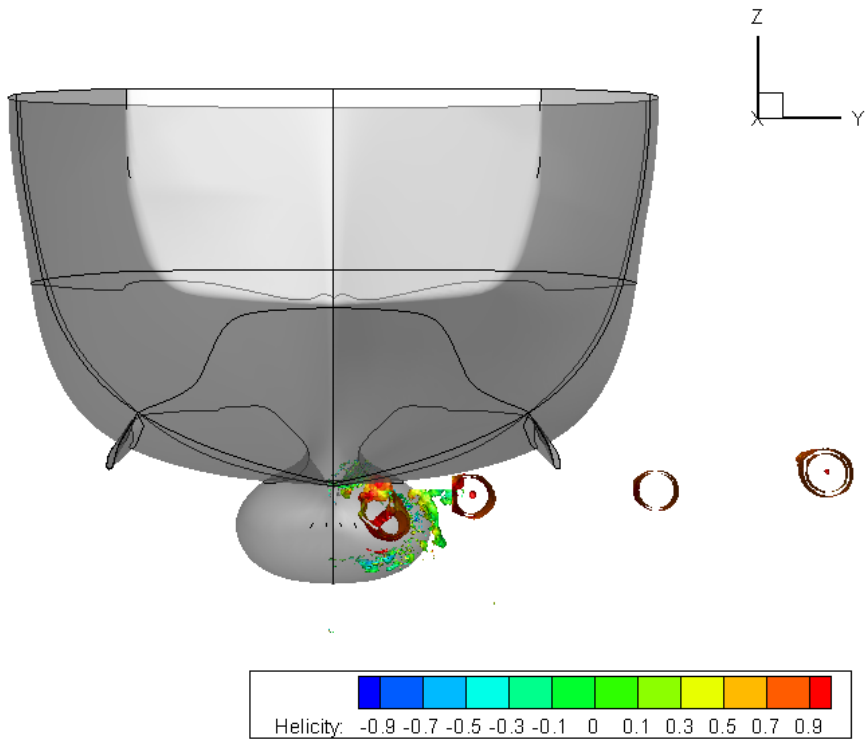
Figure 59: Overview of SDV progression. Iso-surfaces of Q=100, 1000 and 10 000, coloured by H_N, $\beta = 20°$.
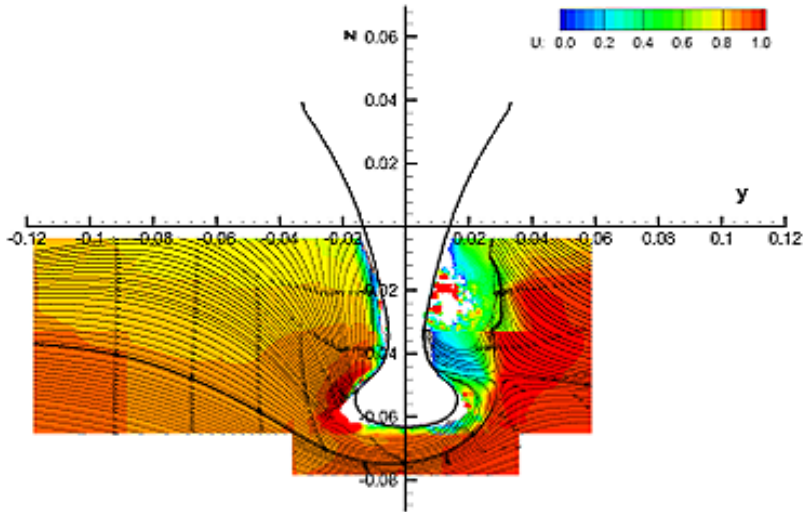
Figure 60: $\beta = 20°$ 2D streamlines at x=0.060.
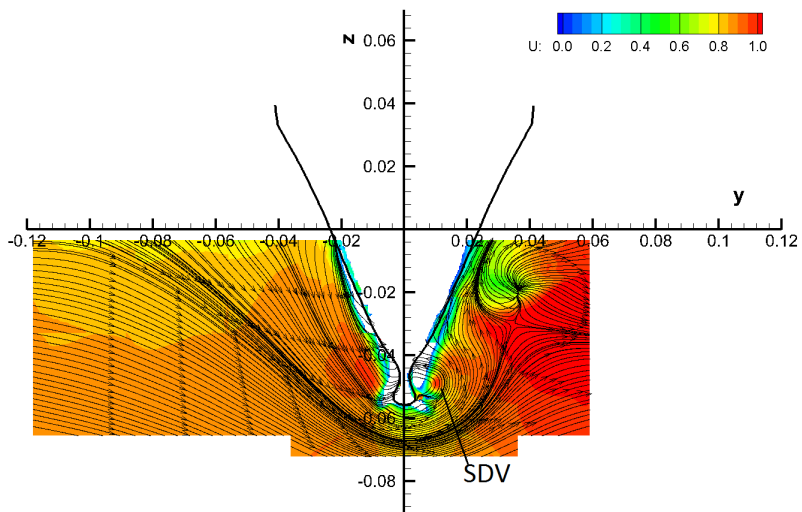
Figure 61: $\beta = 20°$ 2D streamlines at x=0.100.
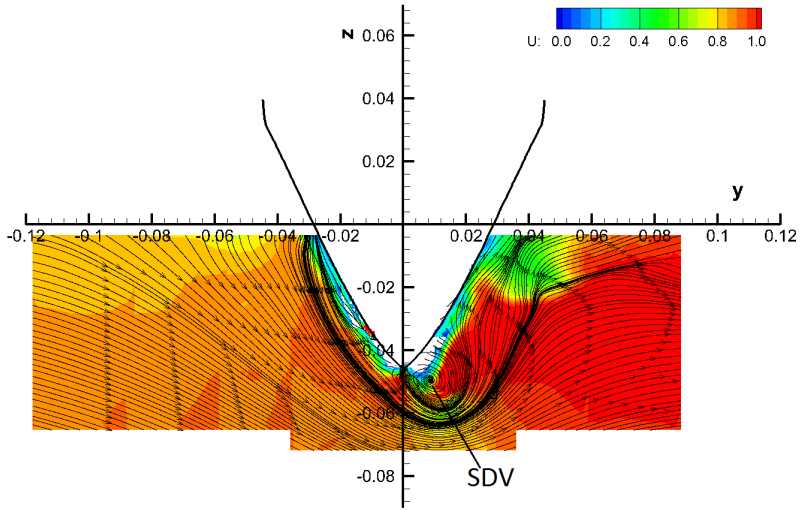
Figure 62: $\beta = 20°$ 2D streamlines at x=0.120.
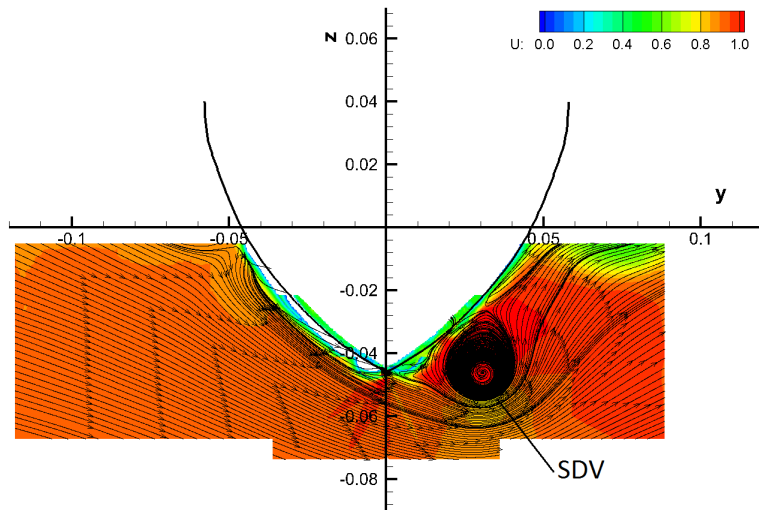
Figure 63: $\beta = 20°$ 2D streamlines at x=0.200.
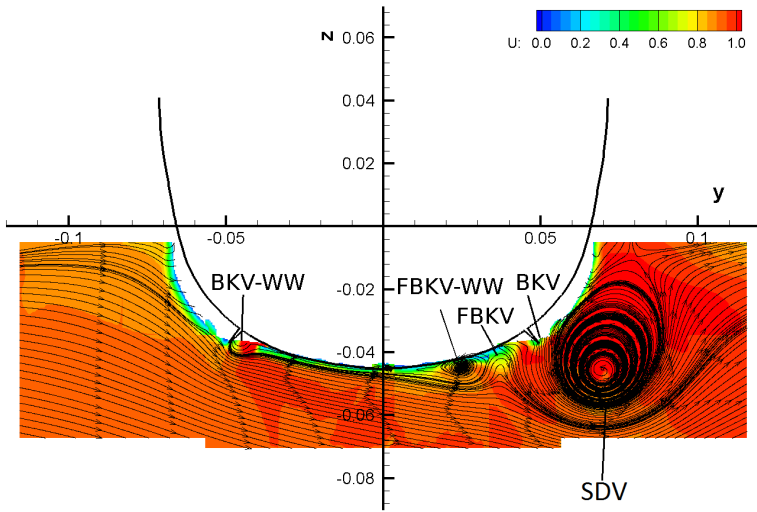
Figure 64: $\beta = 20°$ 2D streamlines at x=0.400.
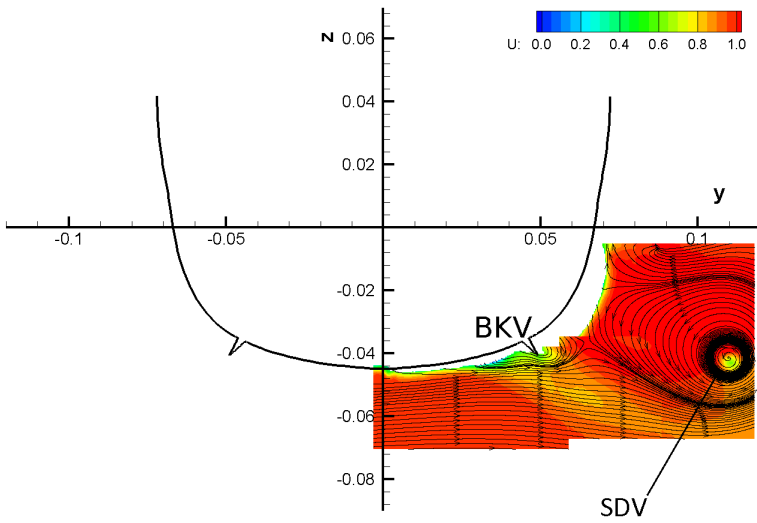
Figure 65: $\beta = 20°$ 2D streamlines at x=0.600.
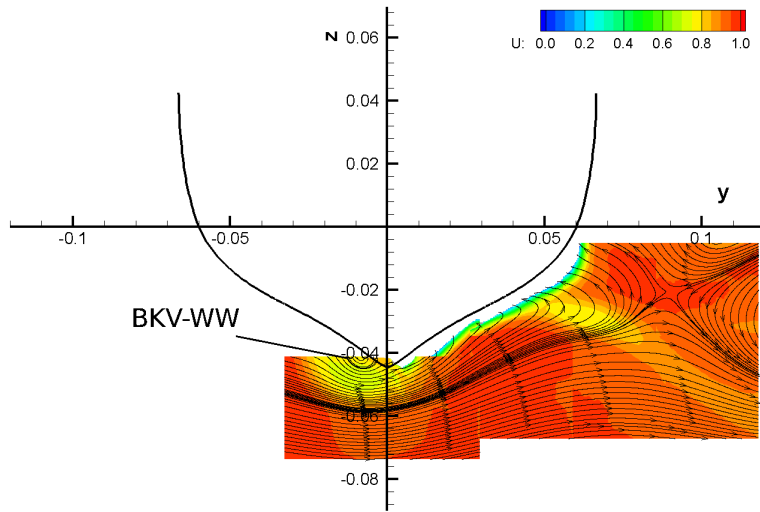
Figure 66: $\beta = 20°$ 2D streamlines at x=0.800.
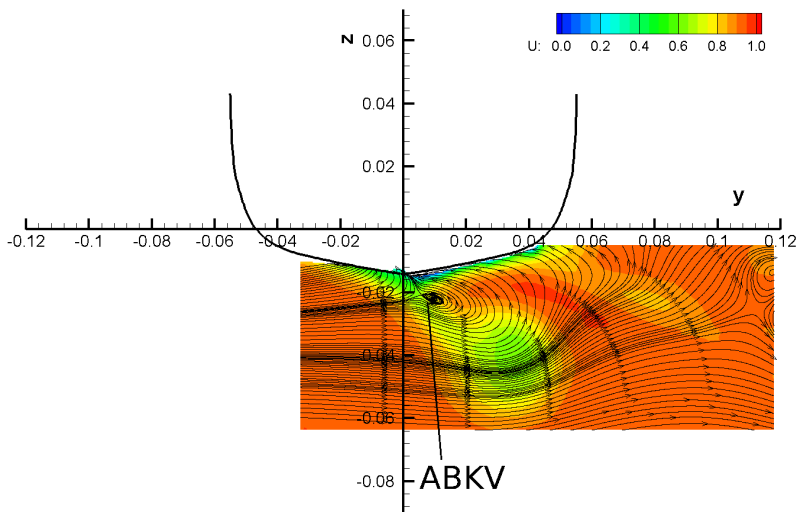
Figure 67: $\beta = 20°$ 2D streamlines at x=0.935.
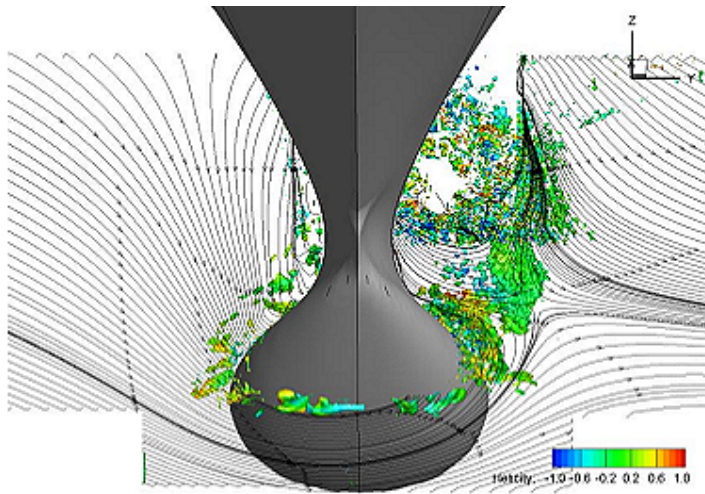
Figure 68: $\beta = 20°$ streamlines with Q=100 iso-surfaces at x=0.060.
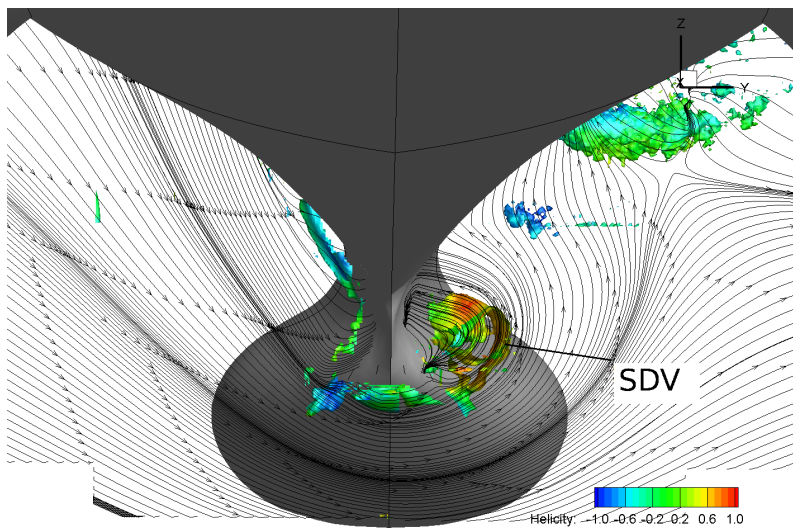
Figure 69: $\beta = 20°$ streamlines with Q=100 iso-surfaces at x=0.100.
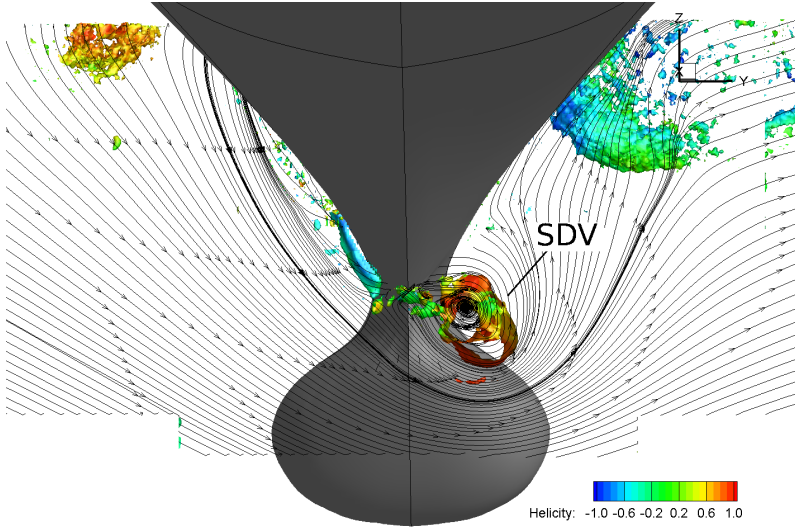
Figure 70: $\beta = 20°$ streamlines with Q=100 iso-surfaces at x=0.120.
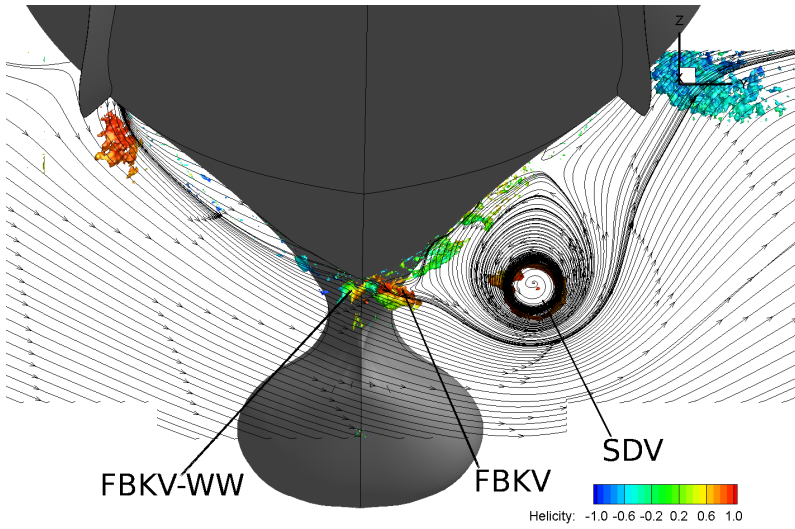
Figure 71: $\beta = 20°$ streamlines with Q=100 iso-surfaces at x=0.200.
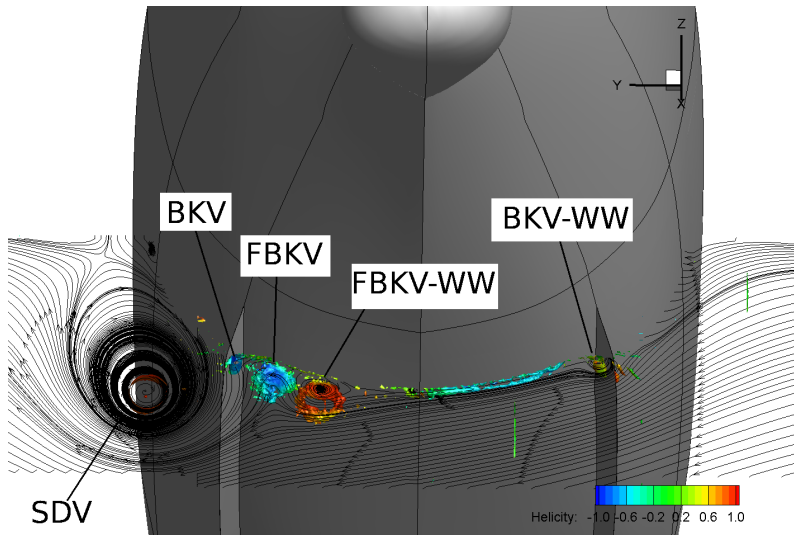
Figure 72: $\beta = 20°$ streamlines with Q=100 iso-surfaces at x=0.400.
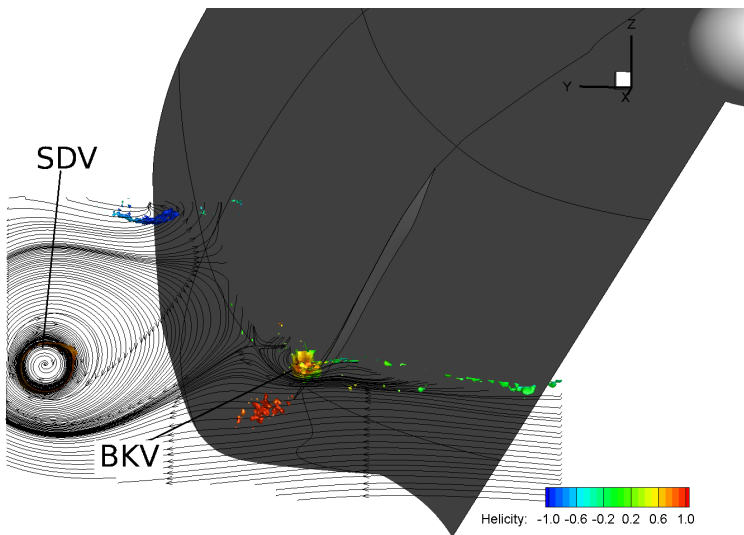
Figure 73: $\beta = 20°$ streamlines with Q=100 iso-surfaces at x=0.600.
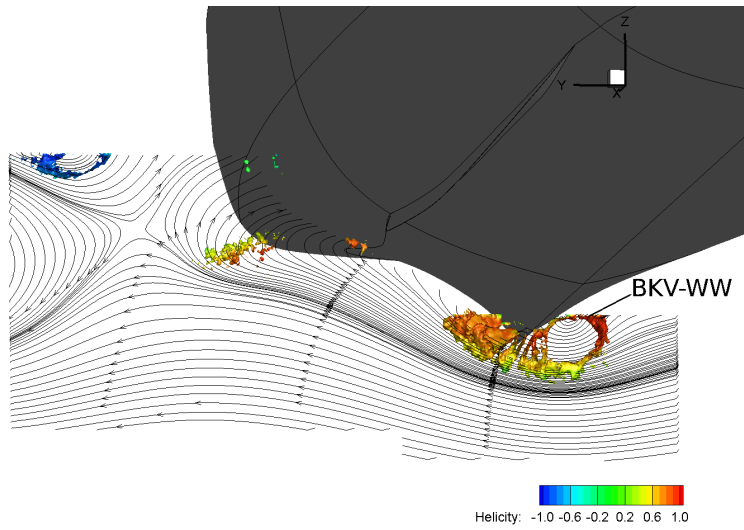
Figure 74: $\beta = 20°$ streamlines with Q=100 iso-surfaces at x=0.800.
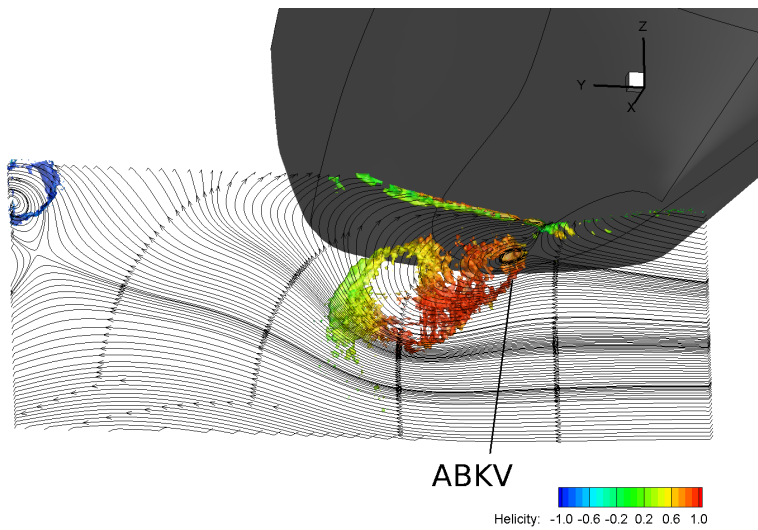
Figure 75: $\beta = 20°$ streamlines with Q=100 iso-surfaces at x=0.935.

4.1 Volume analysis

As we have seen in the previous section, the station x=0.400 displays a number of interesting structures, particularly for the largest drift angle. For this reason, x=0.400 will be the starting point of the detailed analysis. From the tomographic PIV data, we can calculate a number of different variables, many of which are not available from conventional PIV. Examples are the full vorticity and strain matrices and their derived quantities such as Q and λ_2 (see section 2.1.1), as well as the divergence and the 3D turbulent kinetic energy. In the following section we shall take a closer look at these variables, and decide which are the most useful for future work in th DTMB 5415 project.

4.1.1 Mean field

The region around the sonar dome vortex (SDV) will be examined first, for all drift angles, and then the zone containing the FBKV's and starboard side BKV of β=20° will be examined. Figures 76 - 78 show the location of these zones in the measurement plane.
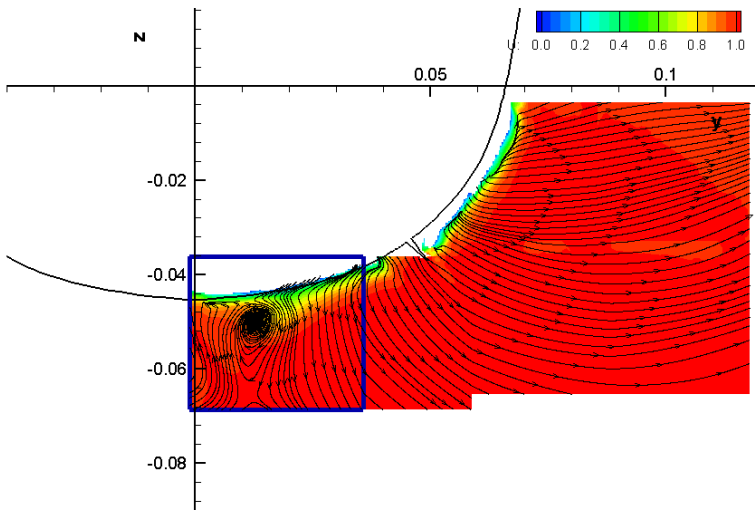
Figure 76: Extracted zone around the SDV, $\beta = -1°$
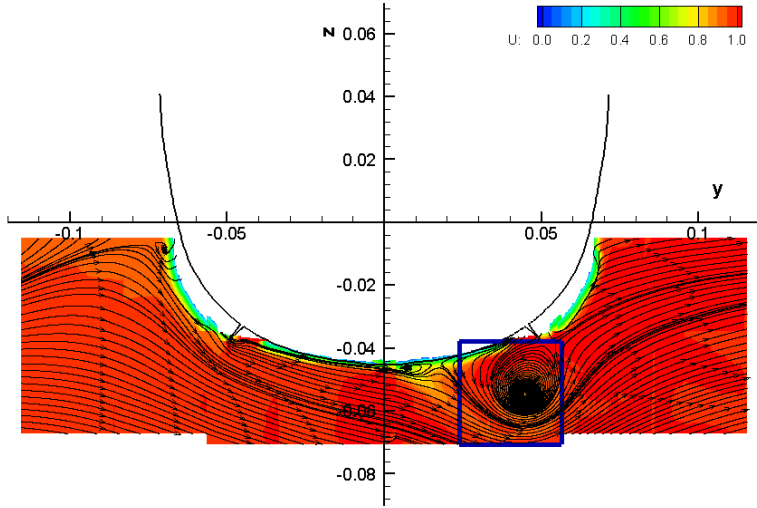
Figure 77: Extracted zone around the SDV, $\beta = 10°$
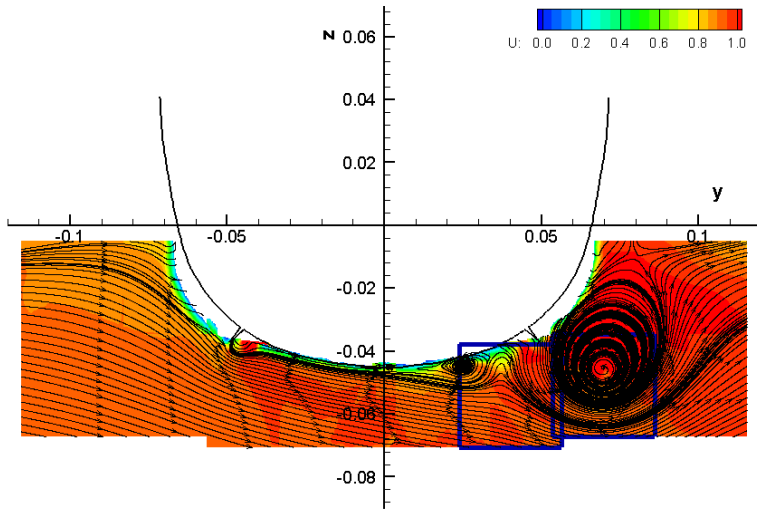
Figure 78: Extracted zone around the SDV (right-hand box), and the FBKV-WW, FBKV and BKV (left-hand box), $\beta = 20°$

First, we take a look at the velocity iso-surfaces, figures 79 - 87. For β=-1°, the streamwise velocity component $\overline{U}$ is close to the free-stream velocity (i.e. the towing speed) for large parts of the domain, but decreases when we approach the hull. There is also a small decrease to the left-hand side of the domain, in the region corresponding to the two SDV's. For β=10° a distinct decrease of the streamwise component is observed towards the hull, and also in the area of the SDV. In the case of β=20°, there is a distinct increase of the streamwise velocity component in the region above the SDV, whereas in the region below it a distinct decrease is observed.

Examining the iso-surfaces of the horizontal crossflow component $\overline{V}$, we see that for both β=10° and 20° the pattern is typical for a single vortex. The velocity minimum is observed in the region above the vortex, and the maximum is found in the region below it. This indicates counter-clockwise rotation in the current frame of reference. Similarly the vertical cross-flow component $\overline{W}$ has its maximum and minimum at the right-hand and left-hand side respectively.

For β=-1°, the pattern is more complex. The horizontal crossflow component is very small, with magnitudes around one tenth of those of the largest drift angle. It is close to zero in most of the right-hand side of the domain, while in the left-hand region small negative values are observed. In the upper part of the domain, towards the hull, small positive values are observed, indicating a clockwise rotation. This notion is supported by the iso-surfaces of the vertical crossflow component, which shows strong positive values in the left-hand region of the domain and negative values in the right-hand region. The magnitude of the positive values is noticeably larger than the magnitude of the negative values, which makes sense in the case of a pair of counter-rotating vortices in the left-hand region, as indicated by the streamlines.

Mass conservation can be used as an indication of measurement accuracy. For a control volume, the change in mass inside the volume must be equal to the mass flux $\mathbf{J}$ across its boundaries, so that

$$\frac{\partial m}{\partial t} = \frac{\partial}{\partial t} \iiint_{\boldsymbol{V}} \rho dV = - \oint \oint_{\boldsymbol{S}} \nabla \cdot \boldsymbol{J} dS. \qquad (37)$$

Using the divergence theorem gives us the relationship between the mass flux and mass density rate of change:

$$\frac{\partial \rho}{\partial t} = -\nabla \cdot \boldsymbol{J} = -\nabla \cdot (\rho \boldsymbol{v}) \tag{38}$$

So, for compressible flow, mass conservation can be expressed as

$$\frac{\partial \rho}{\partial t} + \nabla \cdot (\rho \boldsymbol{v}) = 0. \tag{39}$$

We assume incompressible flow in the current experiment, which means that the continuity equation is simply reduced to the divergence of the velocity vector, given as

$$\frac{\partial u}{\partial x} + \frac{\partial v}{\partial y} + \frac{\partial w}{\partial z} = 0.$$

The divergence of a vector field is a measure of how much the field behaves as a sink or source at a given point. Non-zero divergence, means that there is some loss or creation of mass. With 3D-3C measurements, we can obtain the full divergence of the velocity vector field. Looking at figures 88 -90, we see that the overall divergence, computed from the normalized gradients, is low, if not zero. At drift angles β= -1° and 10°, it increases predictably towards the model hull where data is missing. More alarming are the large values of divergence in the area of the SDV at β= 20°. It is assumed that they are due to a large number of interpolated vectors in the vortex core region, which changes the velocity derivatives.

The averaged Reynolds stress components are given in figures 94 - 111. The concept of Reynolds stress is based on the decomposition of the velocity into its mean and fluctuating components, so that $u_i = \overline{U}_i + u_i'$, and the definition is

$$\tau_{ij}' = \overline{u_i' u_j'}, \tag{40}$$

assuming constant ρ. The physical interpretation of the Reynolds stresses is the rate at which the *ith* component of momentum per unit volume is transported in the *jth* direction by the velocity fluctuations u_j' (Bernard, 1998), i.e. turbulent transport. For example, the Reynolds shear stress component $\overline{u'v'}$ represents transport of streamwise momentum in the cross-stream direction.

The magnitudes of both the normal stresses and the shear Reynolds stresses increase substantially with the drift angle, as the problem becomes

less and less streamlined. At the neutral angle, the DTMB 5415 hull already has distinct bluff body features owing to the sonar dome, which can be compared to a sphere in uniform flow. Increasing the drift angle, and thus the projected area, enhances the pressure drag, feeding the turbulence.

Bernard et al. (1993) examined the role of vortices in the production of Reynolds stresses in near-wall region of turbulent channel flow. It was concluded that Reynolds stress production is inseparable from the dynamics of quasi-streamwise vortical structures in the wall region. Thus, it can be expected that the maxima of the Reynolds stresses are located in the vicinity of the SDV core in this study. This is the case for the two larger drift angles. For β=-1°, however, we consistently observe maxima in a region between the SDV and the hull. This indicates that shear created by the proximity of the SDV to the wall gives the largest contribution to the Reynolds stresses, in this case.

The turbulent kinetic energy (TKE) is presented in figures 91 -93. TKE can generally be quantified by the means of the normal Reynolds stresses as

$$k = \frac{1}{2}\left[\overline{u'u'} + \overline{v'v'} + \overline{w'w'}\right].$$ (41)

Ignoring the areas close to the hull, we observe that the largest values of TKE can be found, not surprisingly, close to the vortex core. This is very clear for β= 10° and 20°. At β=-1°, where the vortex is quite weak compared to the other drift angles, the energy is generally very low. Observe that for 'classically' shaped vortices, here understood as vortices that have a clear circular structure with a defined core region, the iso-surfaces of the turbulent kinetic energy predict the vortex structure rather well (compare the TKE of β=10° with the Q iso-surfaces in fig. 125). For more complicated structures, however, the results are not as good. Comparison with the Q iso-surfaces for β=20° show us that k gives a rather oblong structure with a sort of tail, as opposed to the circular structure shown by Q. This may be due to measurement error, seeing as the calculated divergence is also rather large in the area area of the tail. It is worth noting that both Q and TKE predict local maxima in two areas outside what one would perceive as the geometrical core of the vortex structure. We shall come back to this peculiar feature.

Iso-surfaces of the vorticity components are given in figures 112 - 120,

and the vorticity magnitudes are given in figures 121-123. In Cartesian coordinates, vorticity is given as

$$[\omega_x, \ \omega_y, \ \omega z] = \left[\frac{\partial w}{\partial y} - \frac{\partial v}{\partial z}, \ \frac{\partial u}{\partial z} - \frac{\partial w}{\partial x}, \ \frac{\partial v}{\partial x} - \frac{\partial u}{\partial y} \right] \tag{42}$$

From 2D PIV, the vorticity about the x-axis is already available. However, the remaining two components, which require the out-of-plane velocity, can only be computed from volumetric data. Tomographic PIV, being a 3D-3C technique, is thus very well suited for the task, keeping in mind that volumetric techniques that require the use of several planes can only provide the averaged 3C vorticity field without a compromise in accuracy due to time delay(even if very small).

Considering first the mean-field of ω_x, we see that the largest values appear for β=20°. As was the case with the TKE, the maxima are located on a circular band surrounding the geometrical centre of the structure. Values here are considerably higher, in fact, than at the centre. Moving on to β=10°, we see that the maximum value is approximately half of the maximum for the largest drift angle. Here the maximum is quite clearly located at the geometrical centre of the structure, showing that, for this particular case, using the points of maximum vorticity in each x-plane to locate the vortex core would be a feasible method. Naturally, this could not be known a priori, an obvious drawback, and whether the method works for the instantaneous field remains to be seen. For β=-1° we see evidence of the two counter-rotating SDV's. Vorticity values are low, only about a tenth of the magnitude of the largest drift angle.

ω_y appears less intuitive than ω_x, which is commonly used. For the two larger drift angles, the magnitude of ω_y is considerable lower than that of ω_x, but for β=-1° it is of the same order, indicating that swirling motion in the y-plane is an important part of the flow. For all angles, the maxima of ω_y are in the vicinity of the SDV.

The magnitudes of ω_z are also significantly smaller than ω_x for β=10° and 20°, but only somewhat smaller for β=-1°. Only the largest drift angle has clearly defined local maxima of ω_z, located in the vicinity of the SDV. For all drift angles, the values are mostly negative or small positive.

Summarizing, we have observed that local maxima of all vorticity components are in the vicinity of the SDV, indicating that it has swirl compo-

nents in all three coordinate planes, although for $\beta{=}10°$ and $20°$ rotation about the x-axis is clearly dominant. However, close to the neutral angle, the magnitudes of all three components are quite similar which implies that SDV has a more complicated rotational movement.

It has already been concluded that vorticity is generally not a robust method for identification of vortices. Therefore, two additional variables have been computed: Q and λ_2 (see section 2.1.1 for a thorough description).

The iso surfaces of Q>0 and $\lambda_2 < 0$ are shown in figures 124 -126 and 127 -129 respectively. For $\beta{=}10°$ and $20°$ the SDV is clearly identified by both criteria, and there is little difference in the structure and magnitude. For the smaller drift angle the values are approximately a fifth of those of the larger. For $\beta{=}$-$1°$ both Q and λ_2 the starboard side- and parts of the port side SDV. For Q, however, it looks as though there might be a third vortex between them, albeit weaker. It can be seen as a roundish shape with a 'tongue' sticking down, directly left of the SDV. This is not as clear from the iso-surfaces of λ_2. The shape of the SDV's are similar for both criteria, but λ_2 seems to be more sensitive to measurement noise, particularly in the region close to the ship model hull.

For the largest drift angle the maximum values are located outside of, rather than at the geometrical centre of the vortex structure. The same feature was observed for the iso-surfaces of TKE and ω_x. Thus, we must conclude that the structure is quite complicated and deviates from the classical notion of a vortex, as represented by the SDV of $\beta{=}10°$. Further information must come from observing the instantaneous structures.

In figures 130 -132, the iso-surfaces of $Q > 0$ have been coloured by H_N. For an observer looking towards the bow of the ship model, positive H_N means that the vortex has a counter-clockwise rotation, while negative values of H_N signify clockwise rotation.

We see that the SDV's of the two larger drift angles exhibit consistently large positive values of H_N, i.e. counter-clockwise rotation in the current frame of reference. Looking at $\beta = $-$1°$, several interesting features can be identified. Firstly, applying H_N ascertains the fact that we have a counter-rotating vortex pair, with the starboard side SDV rotating clockwise, and the port-side SDV rotating anti-clockwise. Secondly, for the starboard side SDV there seems to be two regions with large values of $|H_N|$, some distance

apart, which nourishes the suspicion of a third, rather weak vortex close to the starboard SDV. This vortex does not show up when looking at the 2D streamlines, but it has been documented by CFD and EFD analysis. If this is indeed a vortex, the most likely explanation is that the FBKV has not merged with the SDV, but dissipation has weakened it to the point where it is no longer detectable from the streamlines.

We are also able to consider the individual strain components. Although the strain is implicitly contained in the Q-criterion, looking at strain production has a value onto itself for turbulent flow. Turbulence is dominated by energy cascading to increasingly smaller scales, with dissipation as the final result, and the dissipation is directly associated with strain, not with vorticity (Tsinober, 1998).

Figures 133 - 150 display the strain components for all drift angles. For the normal strain components, it is observed that the streamwise strain s_{11} is largest for $\beta = 10°$, whereas the cross-flow components s_{22} and s_{33} increase with the drift angle. The spatial configuration of the strain is largely similar for $\beta = 10°$ and $20°$, owing to the presence of the strong SDV at both drift angles. However, the presence of the model hull is seen for $\beta = 10°$. Looking for example at s_{22}, the strong symmetry of the isosurfaces, as observed for $\beta = 20°$ (fig. 144), is somewhat skewed for $\beta = 10°$ (fig. 143).

For $\beta = -1°$ the normal strains seem to be strongest in the region between the port- and starboard side SDV's (neglecting the region very close to the model hull where the measurement uncertainty gives implausibly high values of the derivatives), which indicates that there is some interaction between the two vortices. The shear strains increase towards the hull.

In the above discussion, we have seen that the strength and size of the vortical structures increase rapidly with the drift angle. The Reynolds stresses have their maxima in the vicinity of the SDV core for the two larger drift angles, but close to the neutral angle the proximity of the SDV to the hull causes increased shear which enhances the production of Reynolds stress in the region between them. ω_x is seen to give a reasonably good representation of the structure of the vortices. It is also seen that the maxima of TKE, $|\omega|$ and Q coincide well for the two larger drift angles, although the agreement is not so good close to the neutral angle. While the

vorticity fields of β=10° and 20° are clearly dominated by ω_x, for β=-1° all three components of ω are of similar magnitude.

The strains are seen to increase with the drift angle. The strain field is very similar for the two largest drift angles, where the flow is dominated by the SDV, although a slight skewness can be observed for β=10° due to influence from the hull. The maxima of the strains are found in the vicinity of the SDV for these two angles.

For β=-1°, the normal strains have maxima in the region between the port- and starboard side SDV's, whereas the shear strains have maxima towards the hull.

The Q-criterion seems to give the most robust representation of the vortical structures in the flow. Q>0 and λ_2<0, do not exhibit significant differences for the mean field, although λ_2 appears to be more sensitive to measurement noise. At β=-1° the Q-criterion, coloured by H_N, indicates the presence of a weak vortex wedged between the port- and starboard side SDV's. This vortex, which is not detected from the streamlines, might be the FBKV which has not yet dissipated or merged with the SDV.

The velocity iso-surfaces are presented, but these do not yield information which is not also contained in the additional variables.

Variables such as turbulent kinetic energy, vorticity, Q and λ_2 seem to be best suited to describe the flow, and further analysis will be restricted to these few. λ_2 is strictly speaking not vital, as we have Q, but we shall keep it for comparison, lest there be any significant difference between the results from the two criteria. For future comparison between CFD and EFD results, as well as between EFD results for different facilities, it should be noted that if the discrepancies are large for variables containing velocity derivatives, simply comparing the measured and simulated velocity iso-surfaces could be quite useful.

Now, we proceed to examine the second interesting region at β=20°, henceforth called zone 02, which holds wind- and leeward FBKV and the leeward BKV.

From figures 152 - 154 it is apparent that ω_x is the strongest of the vorticity components, but that ω_y and ω_z are of the same order of magnitude.

The BKV and leeward FBKV seem to rotate in the same direction, while the windward FBKV rotates opposite of the other two. This is

confirmed by applying the normalized helicity density to the Q iso-surfaces. Figure 157 shows that the BKV and leeward FBKV rotate clockwise in the current frame of reference, while the windward FBKV rotates counter-clockwise.

Iso-surfaces of λ_2, shown in figure 158, are in good agreement with the Q iso-surfaces.

From figure 151 we see that the BKV is by far the strongest of the three vortices in this region, having a TKE magnitude ten times bigger than the FBKV's. The same trend is evident from the Q iso-surfaces in figure 156. Comparison with the SDV (fig 126) shows that the maximum Q values of the BKV are approximately one sixth of the maximum SDV Q values.
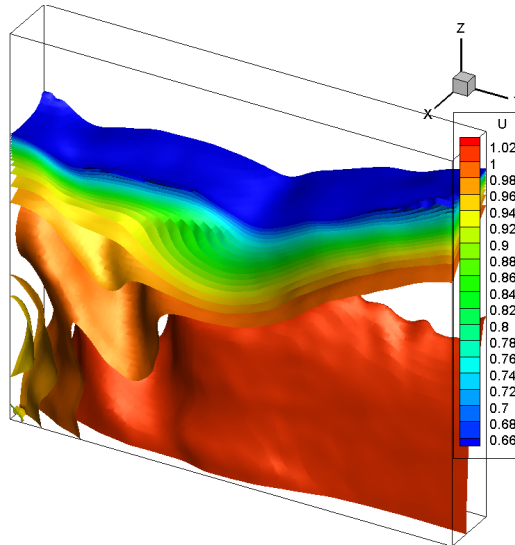
Figure 79: $\overline{u}$ iso-surfaces at x=0.4, $\beta = -1°$.
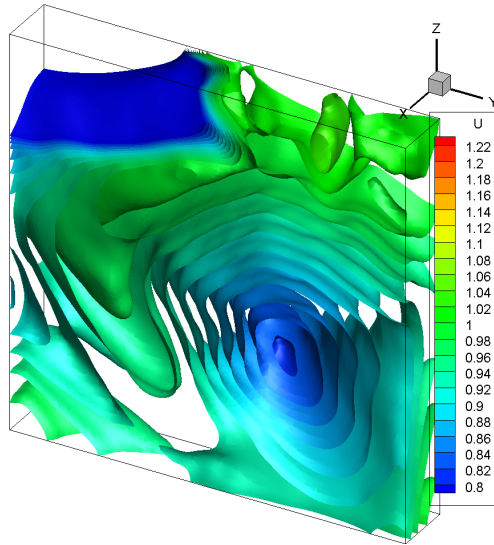
Figure 80: $\overline{u}$ iso-surfaces at x=0.4, $\beta = 10°$.
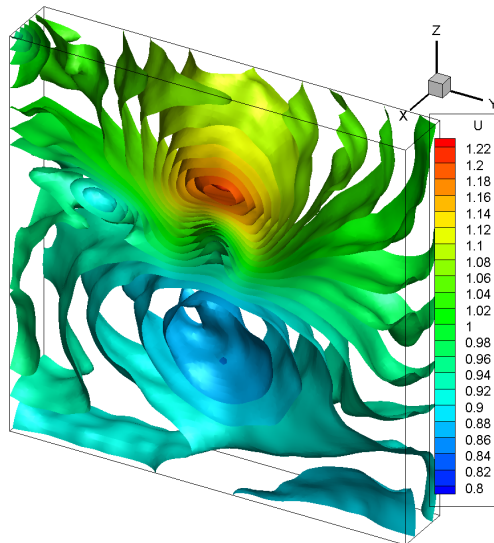
Figure 81: $\overline{u}$ iso-surfaces at x=0.4, $\beta = 20°$.
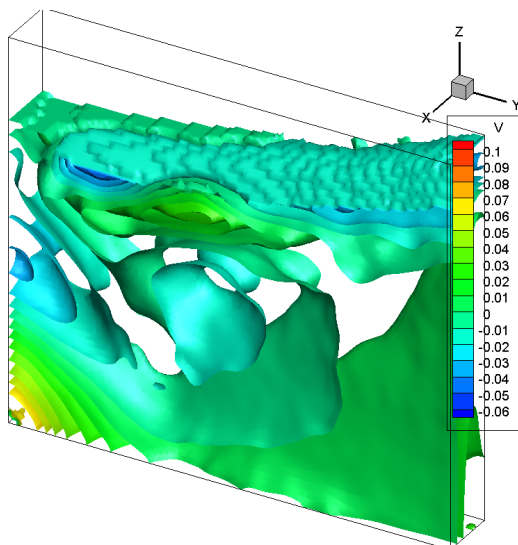
Figure 82: $\overline{v}$ iso-surfaces at x=0.4, $\beta = -1°$.
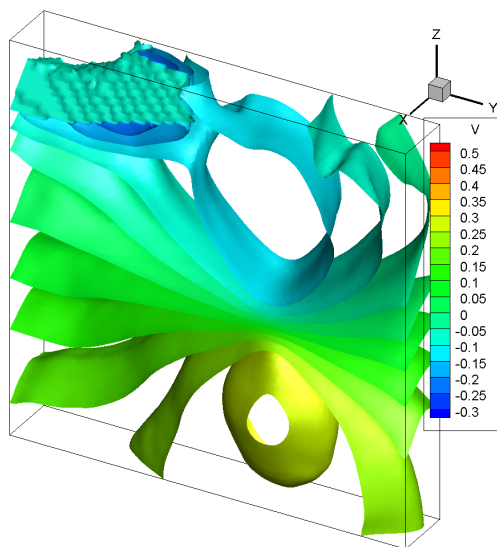
Figure 83: $\overline{v}$ iso-surfaces at x=0.4, $\beta = 10°$.
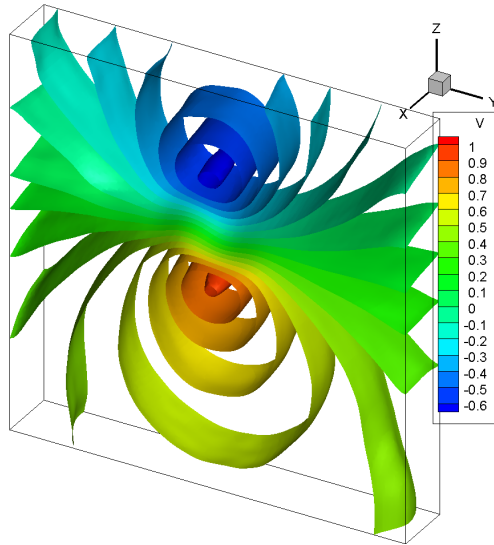
Figure 84: $\overline{w}$ iso-surfaces at x=0.4, $\beta = 20°$.
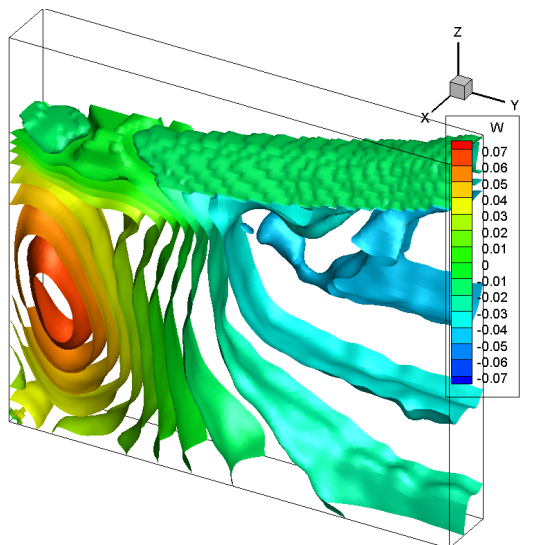
Figure 85: $\overline{w}$ iso-surfaces at x=0.4, $\beta = -1°$.
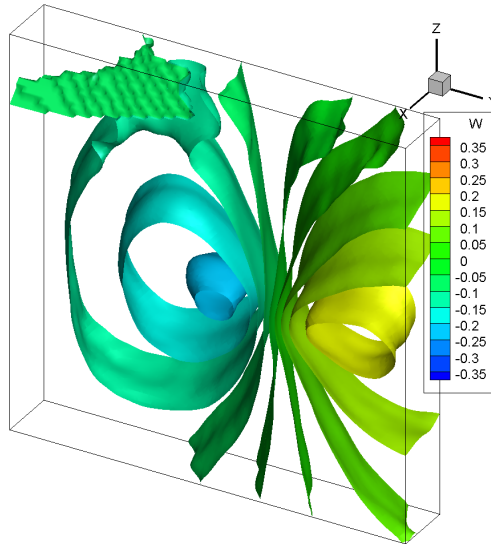
Figure 86: $\overline{w}$ iso-surfaces at x=0.4, $\beta = 10°$.
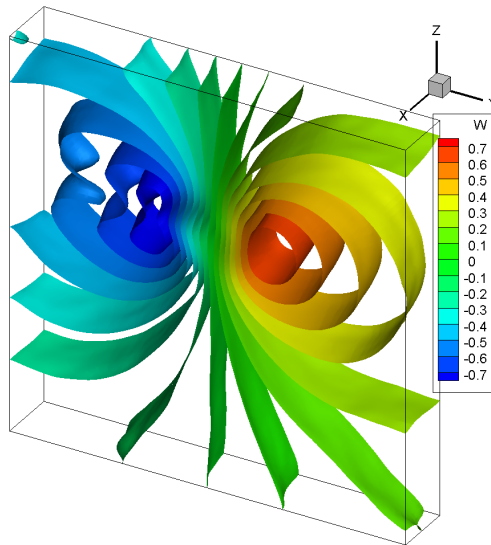
Figure 87: $\overline{w}$ iso-surfaces at x=0.4, $\beta = 20°$.
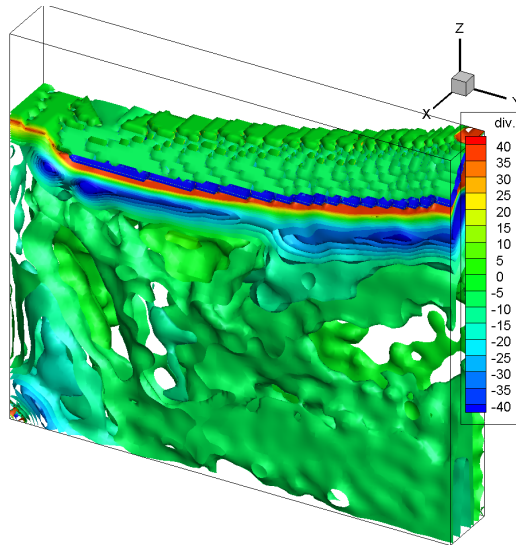
Figure 88: Divergence iso-surfaces at x=0.400, $\beta = -1°$.
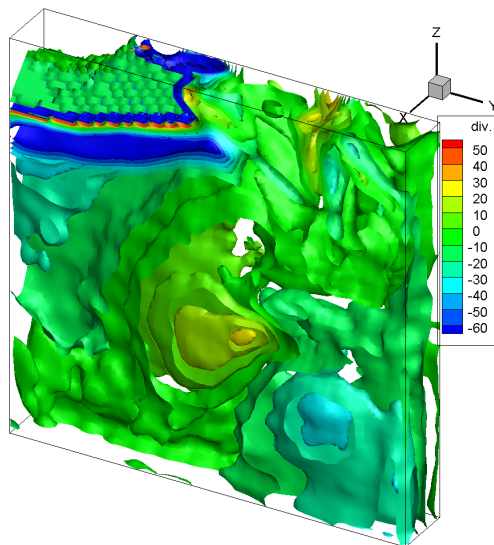
Figure 89: Divergence iso-surfaces at x=0.400, $\beta = 10°$.
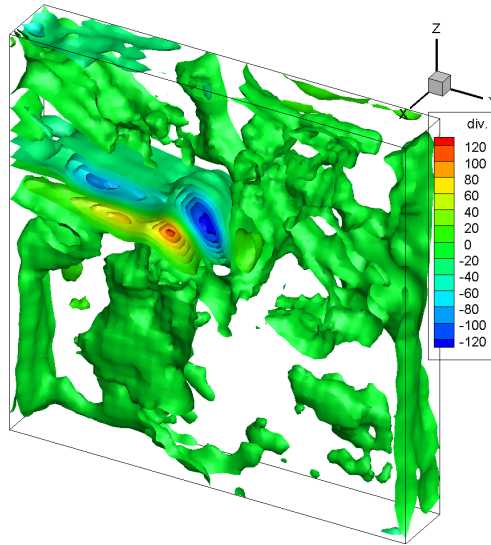
Figure 90: Divergence iso-surfaces at x=0.400, $\beta = 20°$.
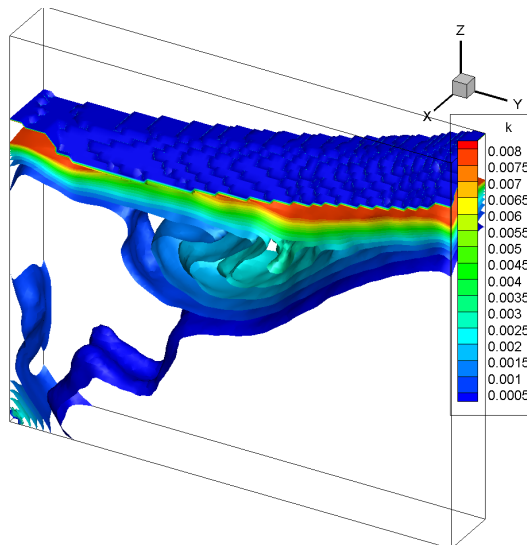
Figure 91: k iso-surfaces at x=0.400, $\beta = -1°$.
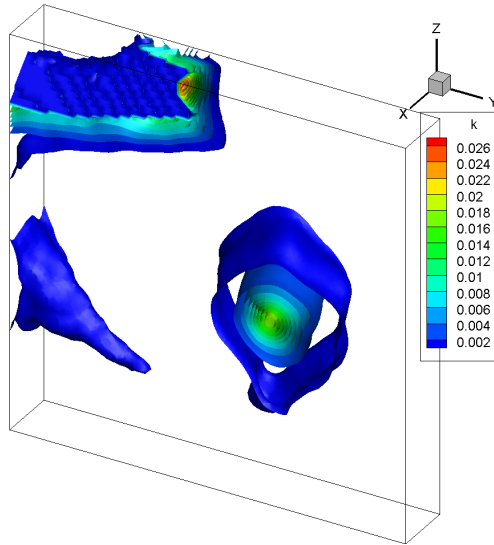
Figure 92: k iso-surfaces at x=0.400, $\beta = 10°$.
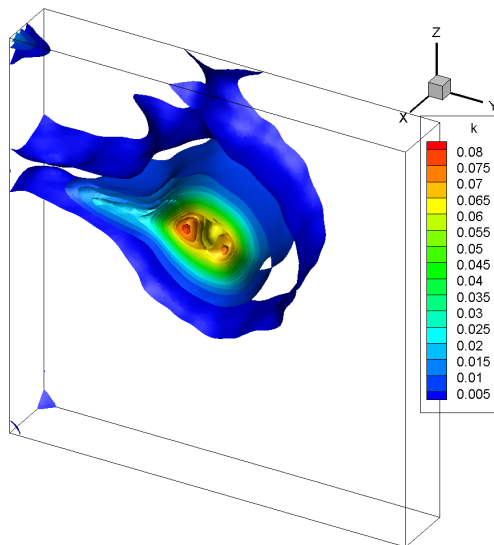
Figure 93: k iso-surfaces at x=0.400, $\beta = 20°$.
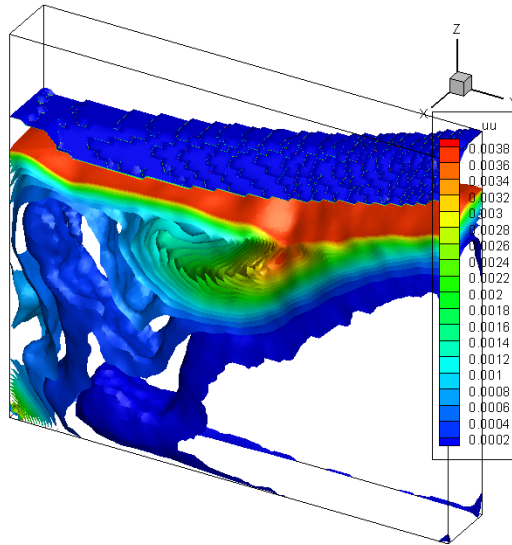
Figure 94: $\overline{u'u'}$ iso-surfaces at x=0.400, $\beta = -1°$.
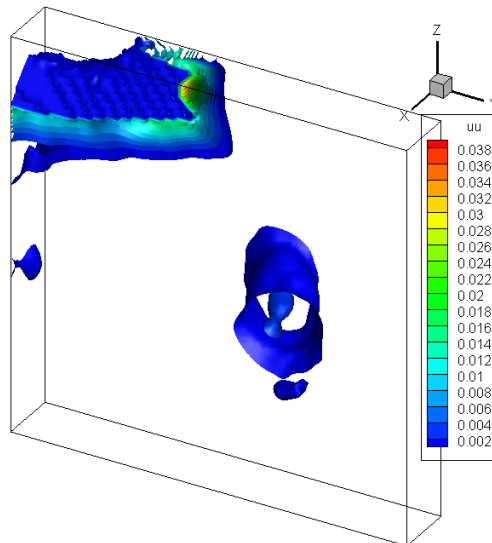
Figure 95: $\overline{u'u'}$ iso-surfaces at x=0.400, $\beta = 10°$.
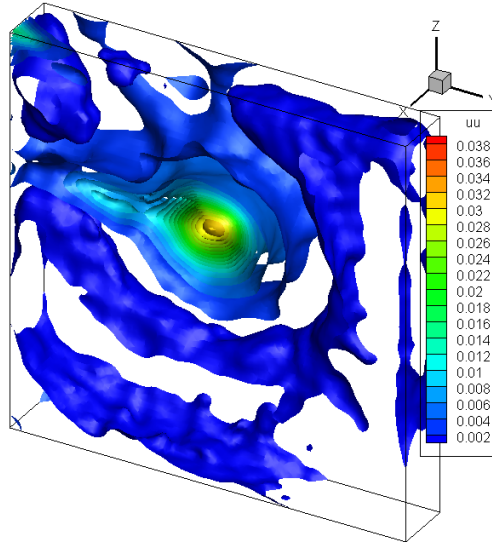
Figure 96: $\overline{u'u'}$ iso-surfaces at x=0.400, $\beta = 20°$.
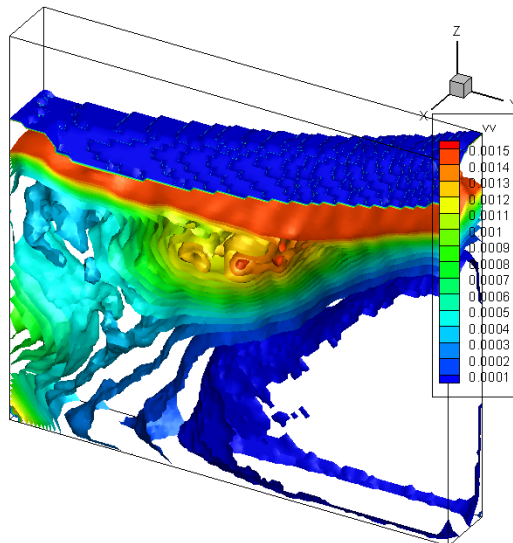
Figure 97: $\overline{v'v'}$ iso-surfaces at x=0.400, $\beta = -1°$.
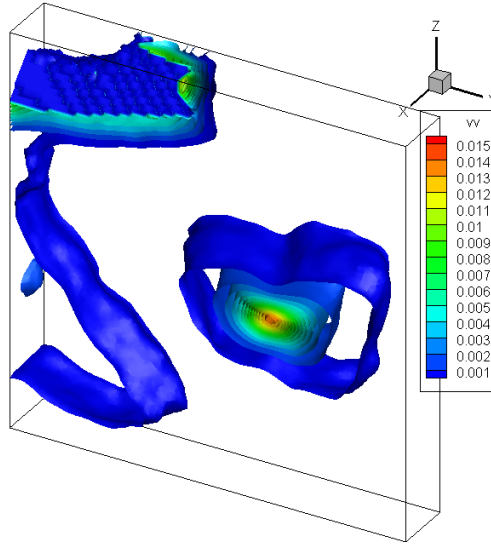
Figure 98: $\overline{v'v'}$ iso-surfaces at x=0.400, $\beta = 10°$.
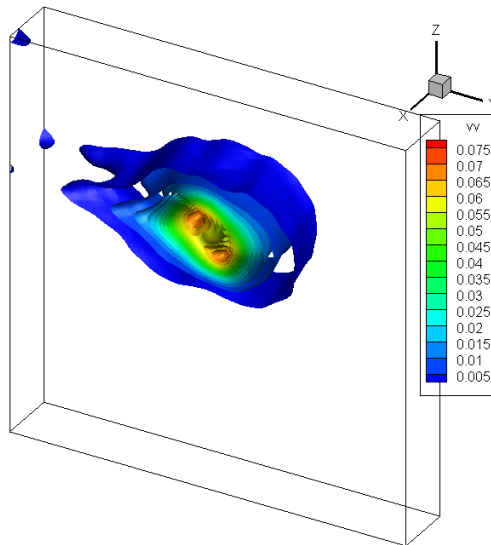
Figure 99: $\overline{v'v'}$ iso-surfaces at x=0.400, $\beta = 20°$.
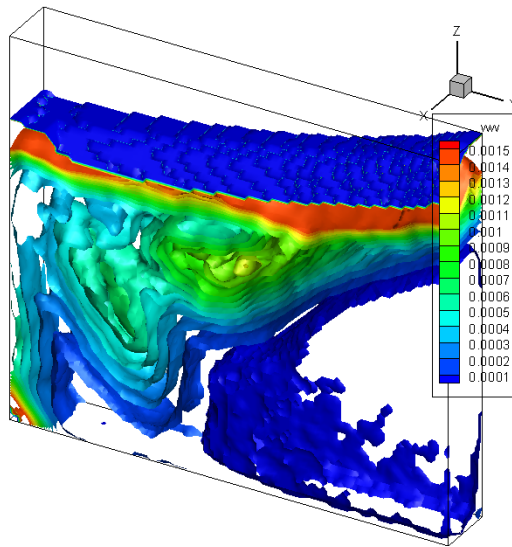
Figure 100: $\overline{w'w'}$ iso-surfaces at x=0.400, $\beta = -1°$.
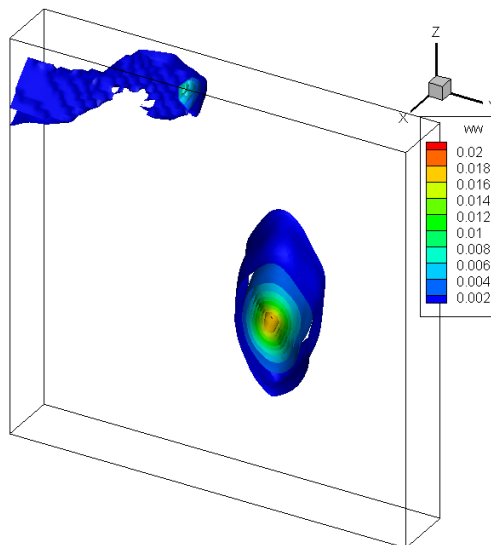
Figure 101: $\overline{w'w'}$ iso-surfaces at x=0.400, $\beta = 10°$.
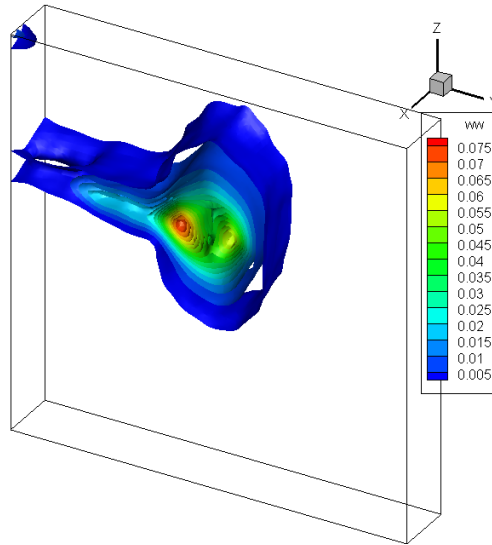
Figure 102: $\overline{w'w'}$ iso-surfaces at x=0.400, $\beta = 20°$.
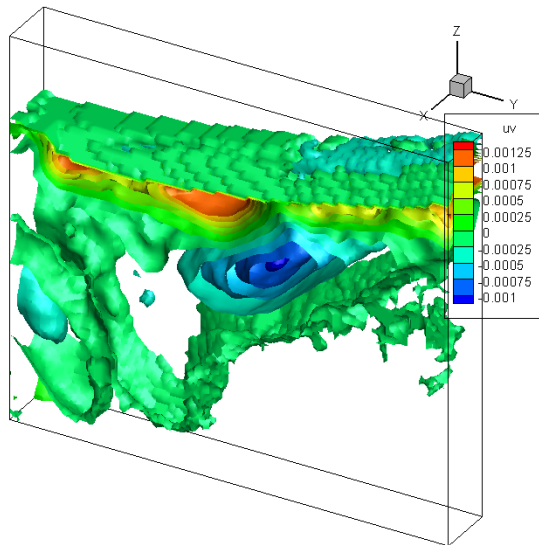
Figure 103: $\overline{u'v'}$ iso-surfaces at x=0.400, $\beta = -1°$.
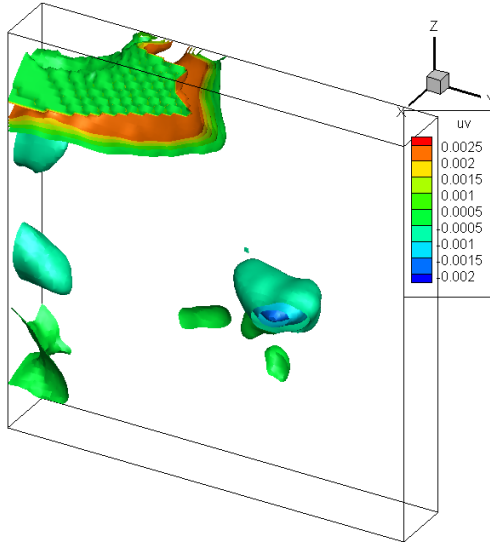
Figure 104: $\overline{u'v'}$ iso-surfaces at x=0.400, $\beta = 10°$.
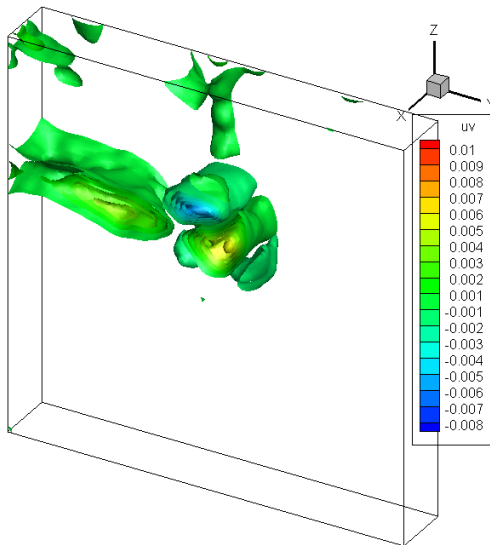
Figure 105: $\overline{u'v'}$ iso-surfaces at x=0.400, $\beta = 20°$.
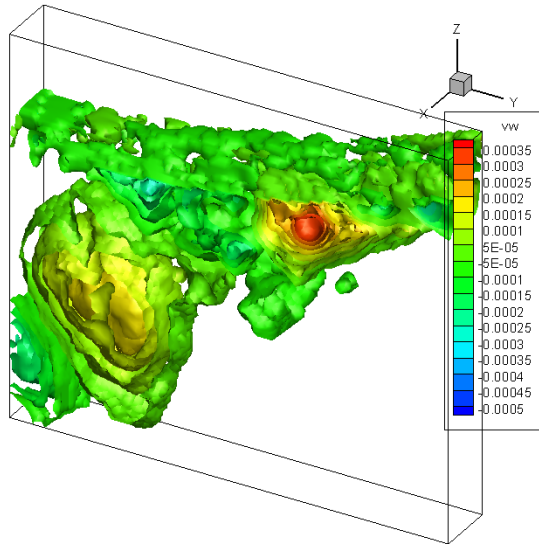
Figure 106: $\overline{v'w'}$ iso-surfaces at x=0.400, $\beta = -1°$.
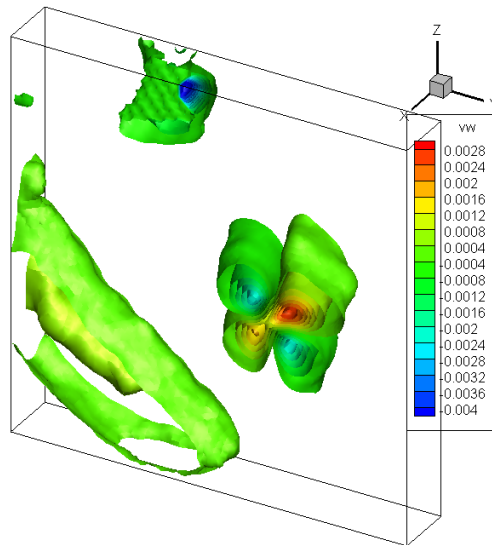
Figure 107: $\overline{v'w'}$ iso-surfaces at x=0.400, $\beta = 10°$.
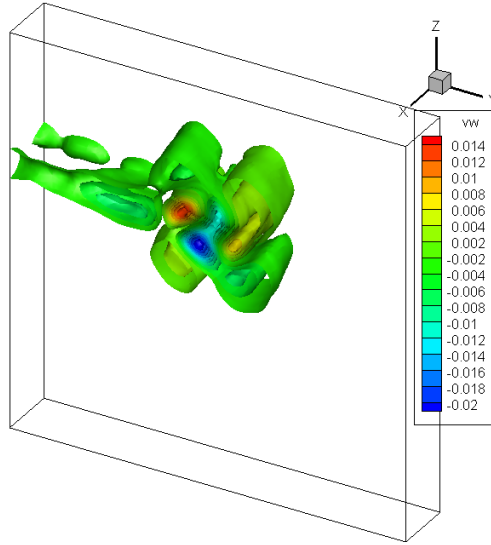
Figure 108: $\overline{v'w'}$ iso-surfaces at x=0.400, $\beta = 20°$.
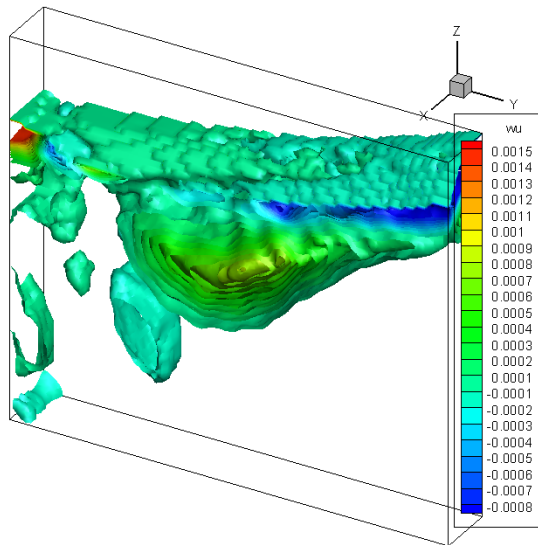
Figure 109: $\overline{w'u'}$ iso-surfaces at x=0.400, $\beta = -1°$.
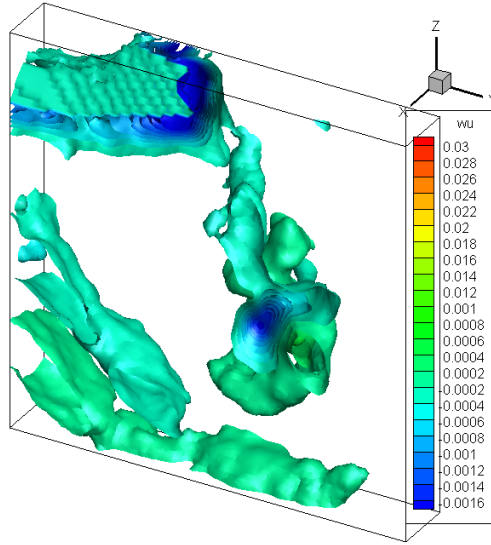
Figure 110: $\overline{w'u'}$ iso-surfaces at x=0.400, $\beta = 10°$.
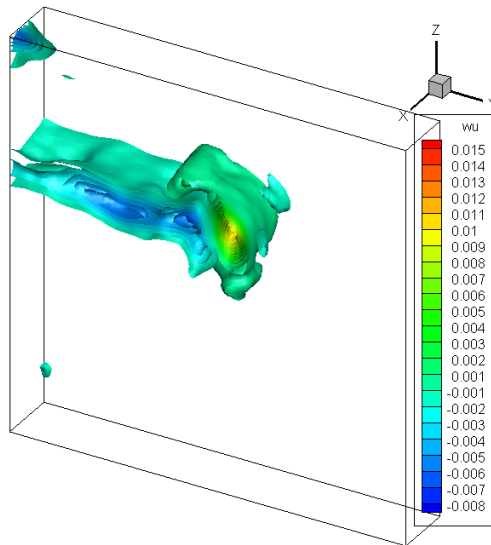
Figure 111: $\overline{w'u'}$ iso-surfaces at x=0.400, $\beta = 20°$.
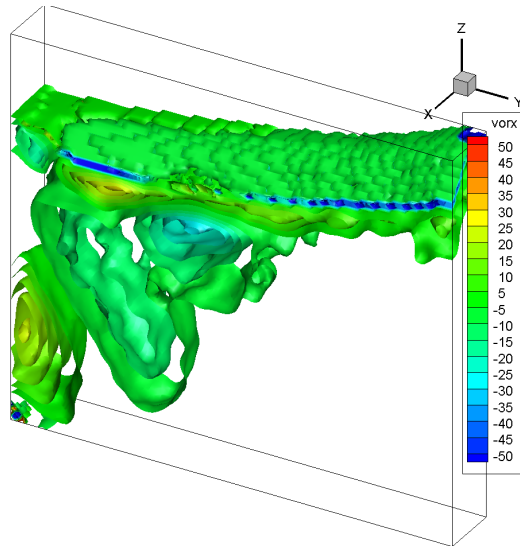
Figure 112: ω_x iso-surfaces at x=0.400, $\beta = -1°$.

Figure 113: ω_x iso-surfaces at x=0.400, $\beta = 10°$.

104
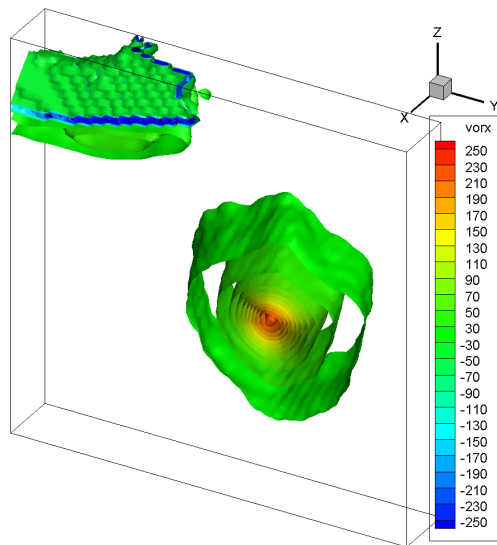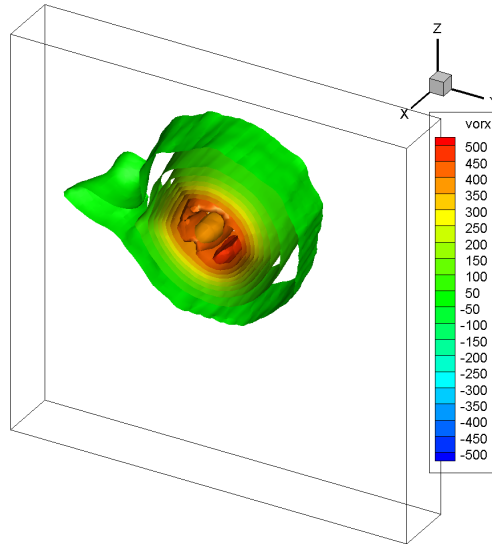
Figure 114: ω_x iso-surfaces at x=0.400, $\beta = 20°$.
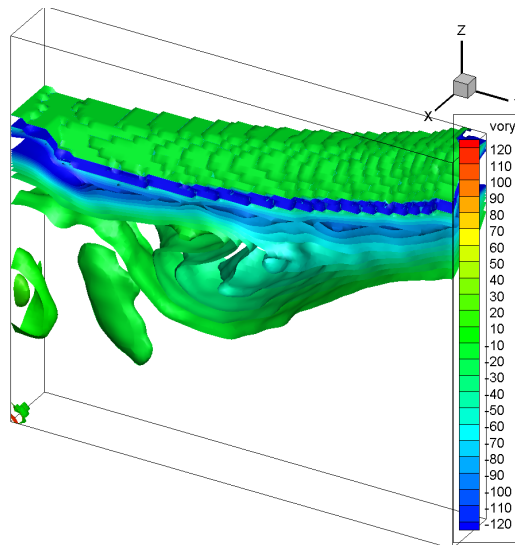
Figure 115: ω_y iso-surfaces at x=0.400, $\beta = -1°$.
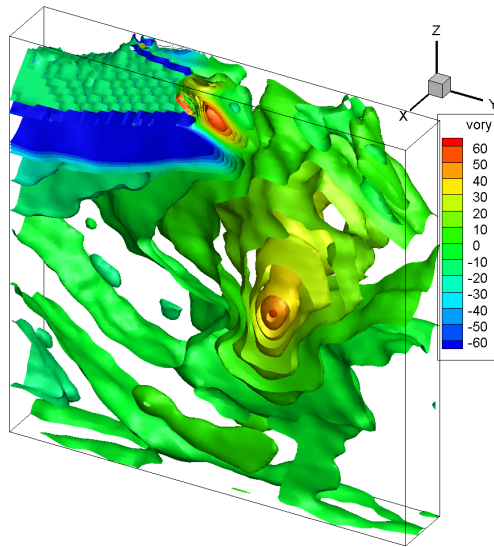
Figure 116: ω_y iso-surfaces at x=0.400, $\beta = 10°$.
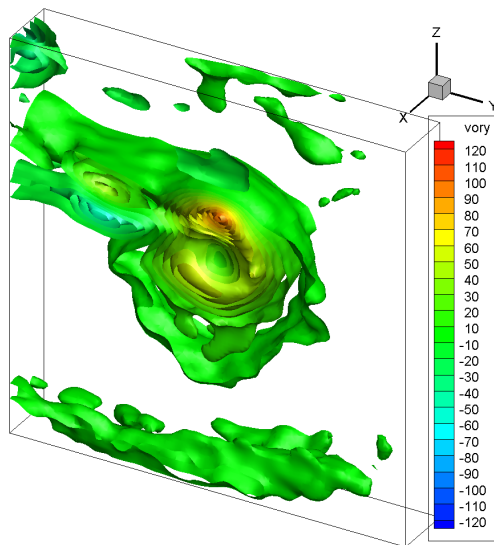
Figure 117: ω_y iso-surfaces at x=0.400, $\beta = 20°$.
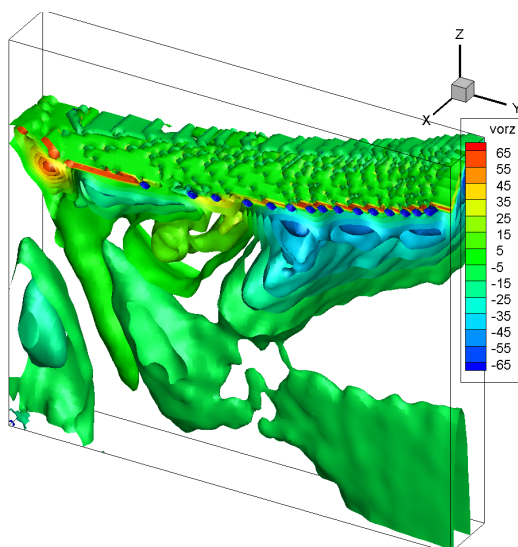
Figure 118: ω_z iso-surfaces at x=0.400, $\beta = -1°$.
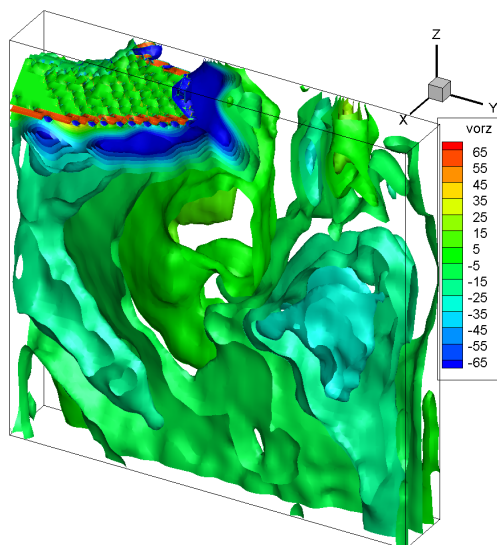
Figure 119: ω_z iso-surfaces at x=0.400, $\beta = 10°$.
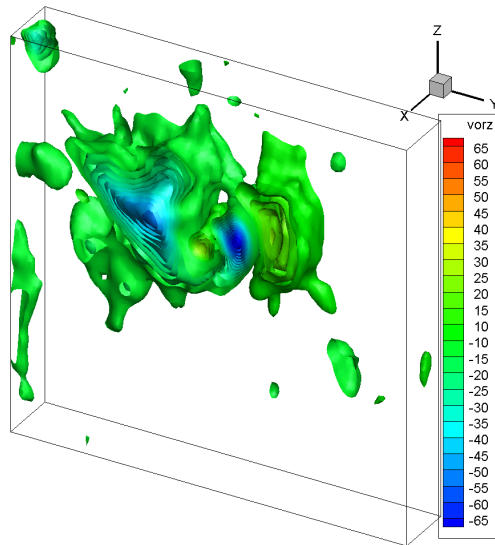
Figure 120: ω_z iso-surfaces at x=0.400, $\beta = 20°$.
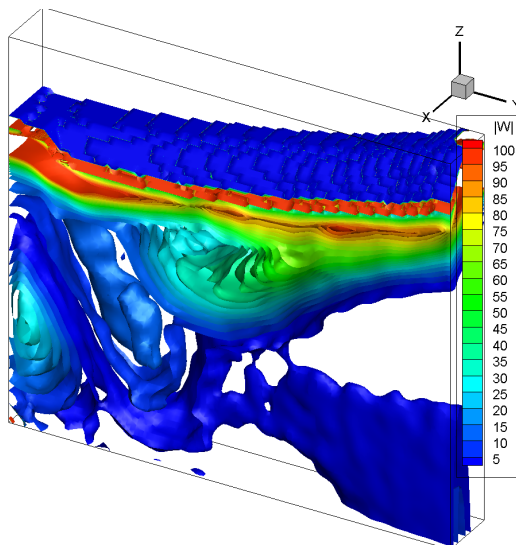
Figure 121: $|\omega|$ iso-surfaces at x=0.4, $\beta = -1°$.
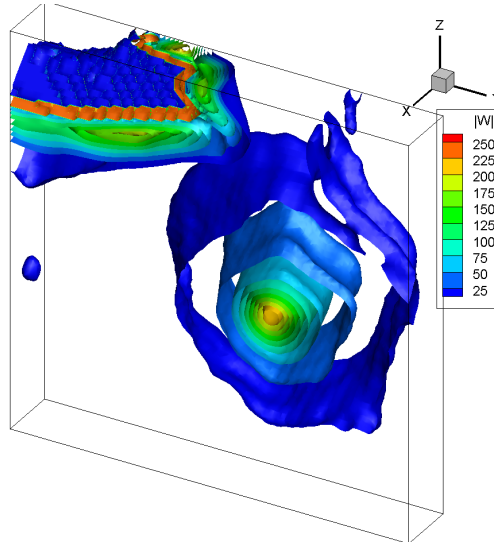
Figure 122: $|\omega|$ iso-surfaces at x=0.4, $\beta = 10°$.
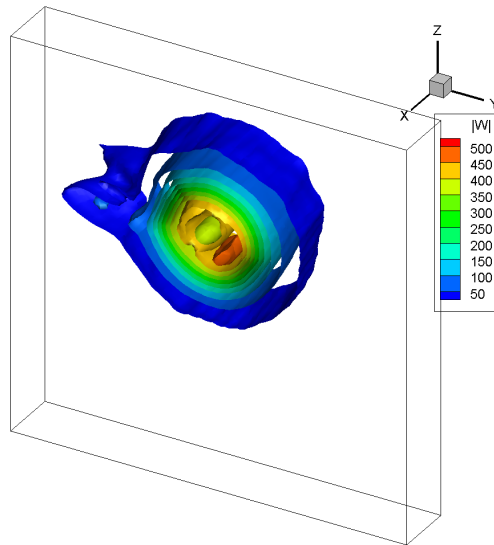
Figure 123: $|\omega|$ iso-surfaces at x=0.4, $\beta = 20°$.
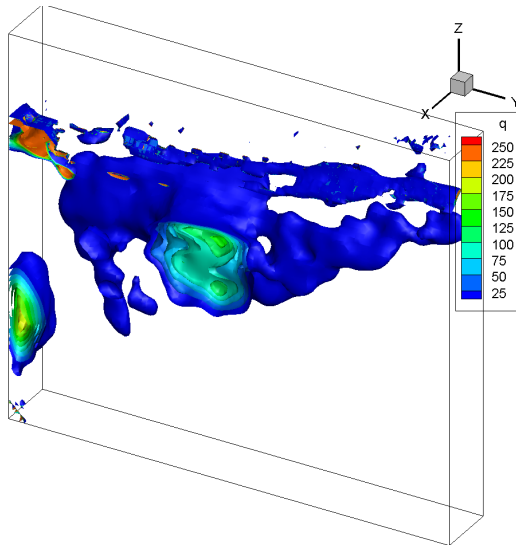
Figure 124: Q iso-surfaces at x=0.400, $\beta = -1°$.
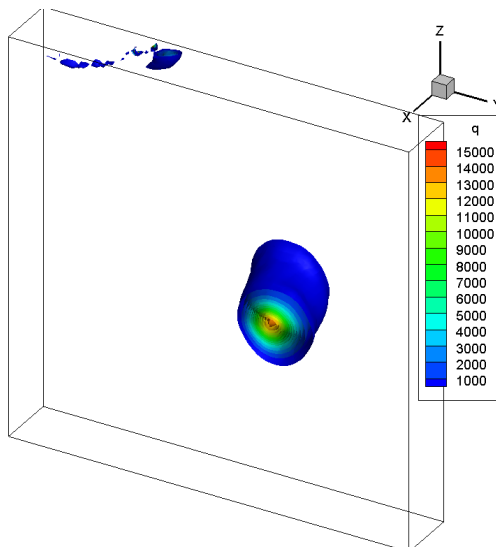
Figure 125: Q iso-surfaces at x=0.400, $\beta = 10°$.
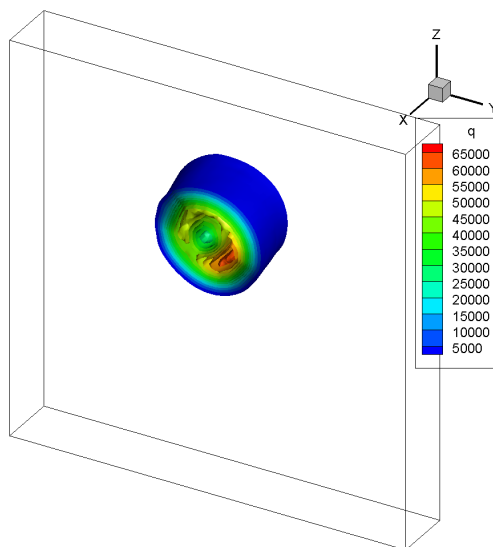
Figure 126: Q iso-surfaces at x=0.400, $\beta = 20°$.
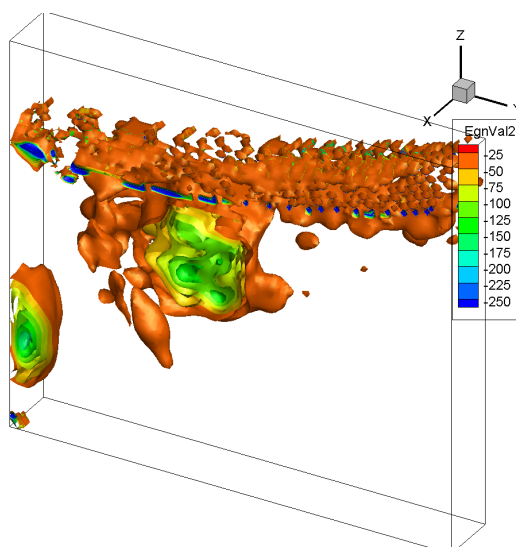
Figure 127: λ_2 iso-surfaces at x=0.400, $\beta = -1°$.
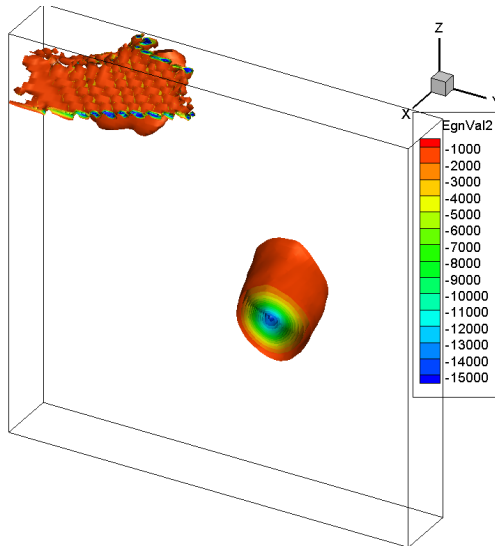
Figure 128: λ_2 iso-surfaces at x=0.400, $\beta = 10°$.
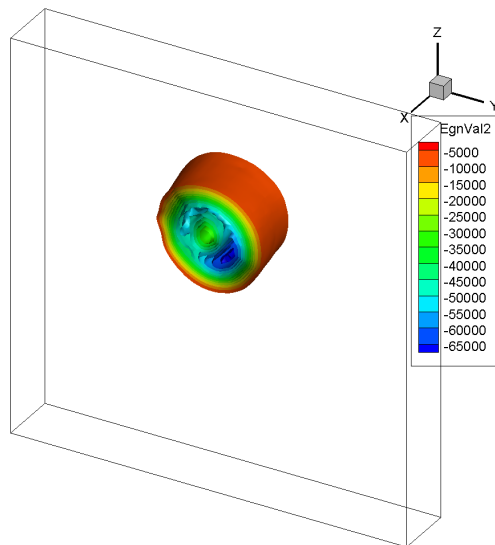
Figure 129: λ_2 iso-surfaces at x=0.400, $\beta = 20°$.
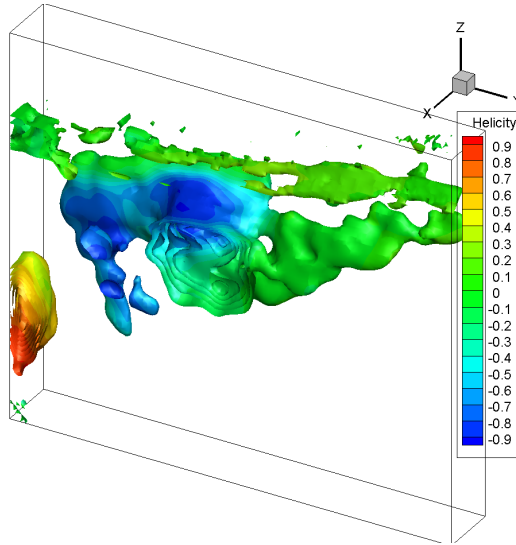
Figure 130: Q iso-surfaces at x=0.400 coloured by H_N, $\beta = -1°$.
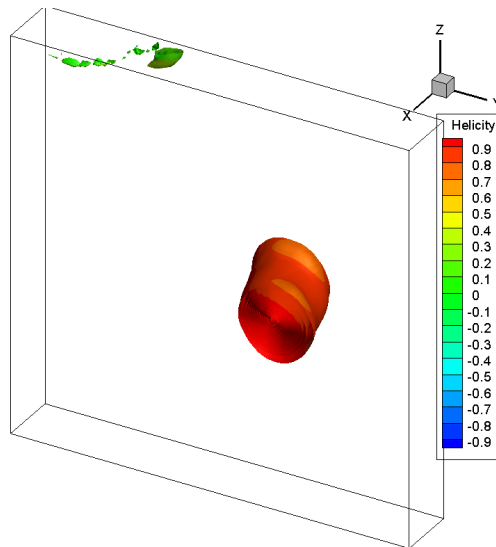
Figure 131: Q iso-surfaces at x=0.400 coloured by H_N, $\beta = 10°$.
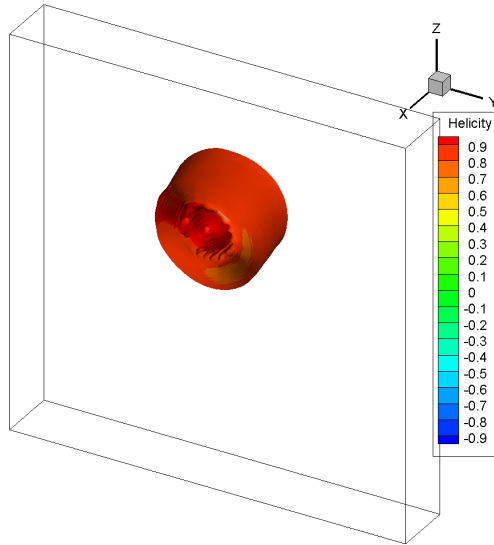
Figure 132: Q iso-surfaces at x=0.400 coloured by H_N, $\beta = 20°$.
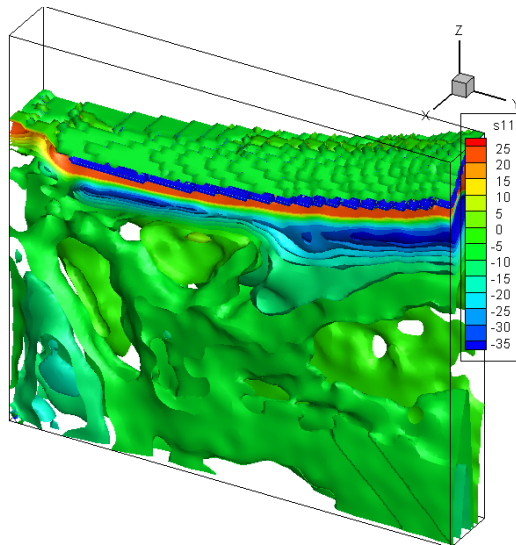
Figure 133: $\boldsymbol{S}_{11}$ iso-surfaces at x=0.400, $\beta = -1°$.
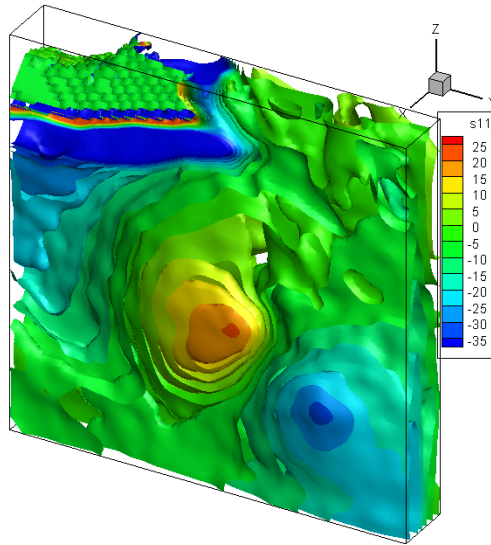
Figure 134: S_{11} iso-surfaces at x=0.400, $\beta = 10°$.
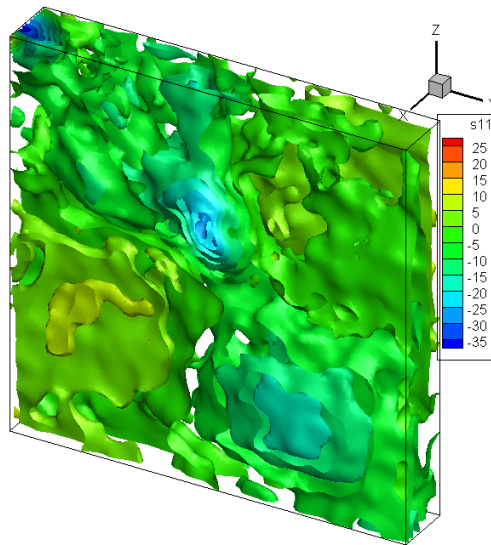
Figure 135: S_{11} iso-surfaces at x=0.400, $\beta = 20°$.
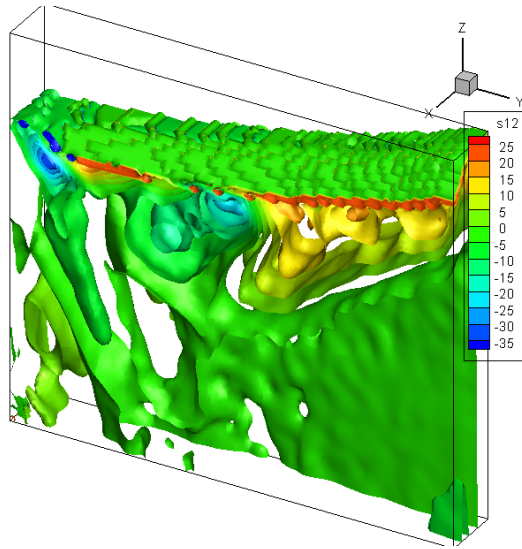
Figure 136: S_{12} iso-surfaces at x=0.400, $\beta = -1°$.
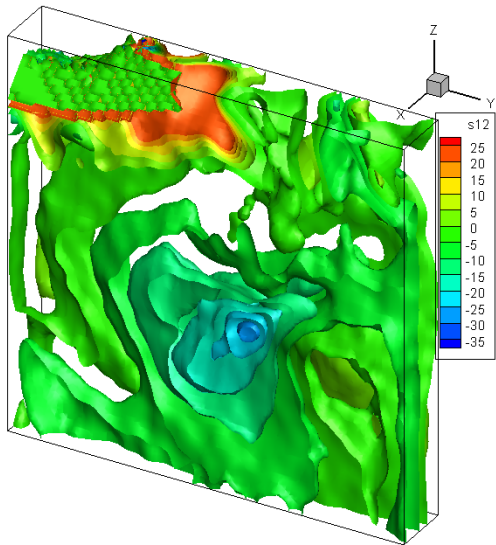
Figure 137: S_{12} iso-surfaces at x=0.400, $\beta = 10°$.
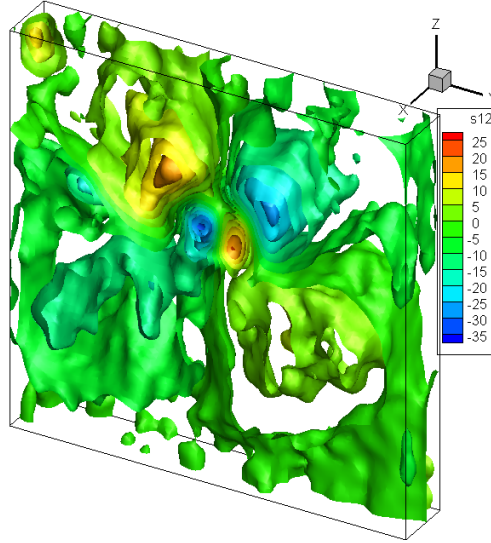
Figure 138: S_{12} iso-surfaces at x=0.400, $\beta = 20°$.
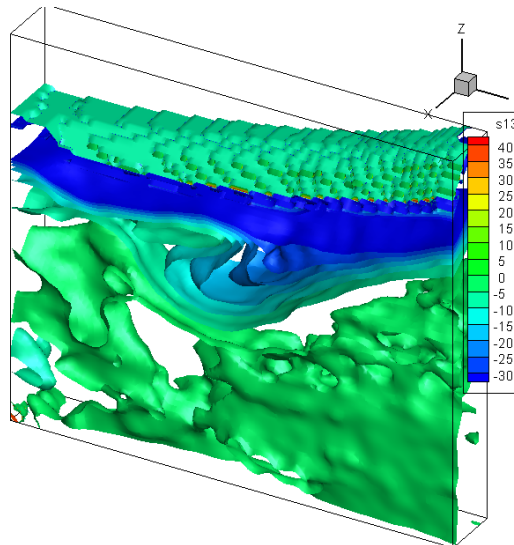
Figure 139: S_{13} iso-surfaces at x=0.400, $\beta = -1°$.
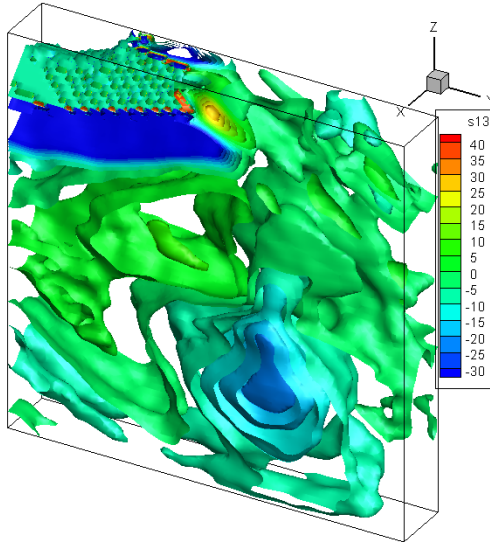
Figure 140: S_{13} iso-surfaces at x=0.400, $\beta = 10°$.
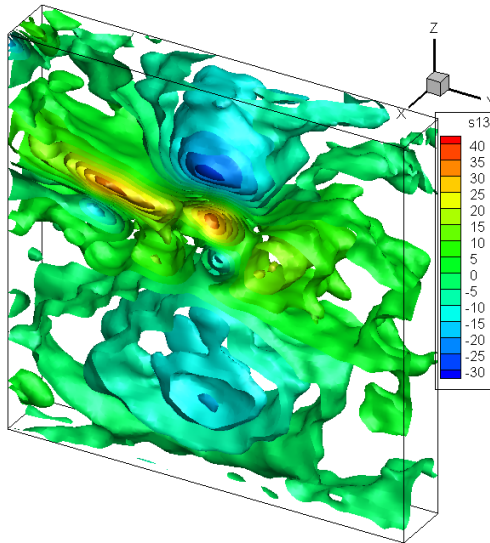
Figure 141: S_{13} iso-surfaces at x=0.400, $\beta = 20°$.
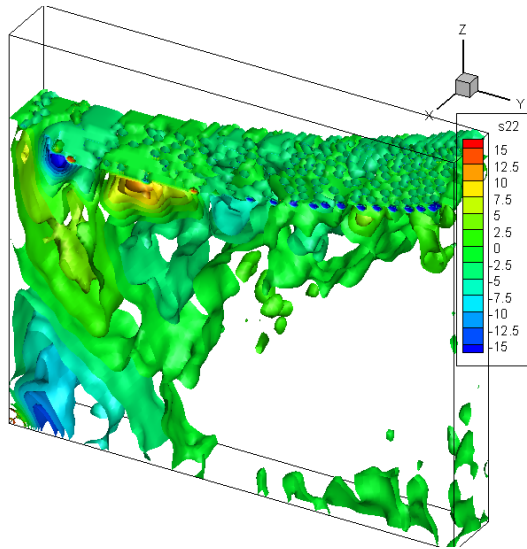
Figure 142: S_{22} iso-surfaces at x=0.400, $\beta = -1°$.
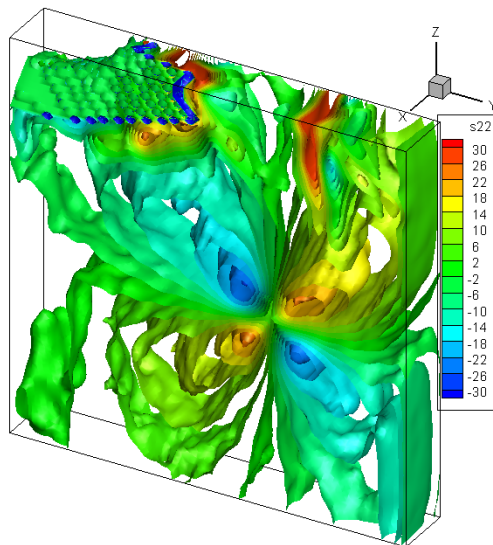
Figure 143: S_{22} iso-surfaces at x=0.400, $\beta = 10°$.
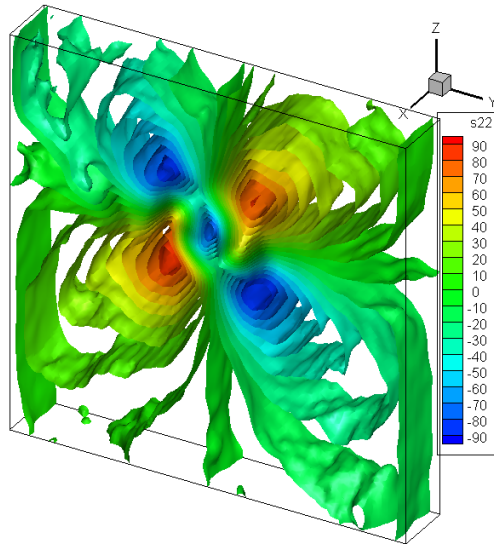
Figure 144: S_{22} iso-surfaces at x=0.400, $\beta = 20°$.
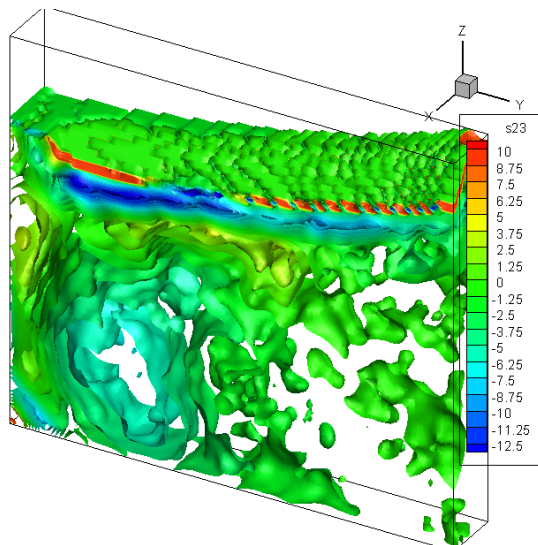
Figure 145: S_{23} iso-surfaces at x=0.400, $\beta = -1°$.
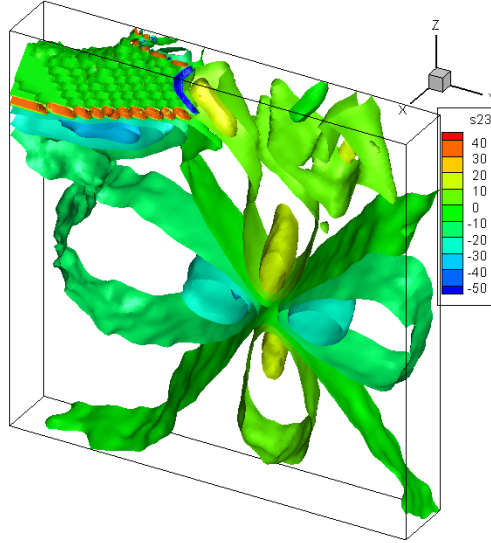
Figure 146: S_{23} iso-surfaces at x=0.400, $\beta = 10°$.
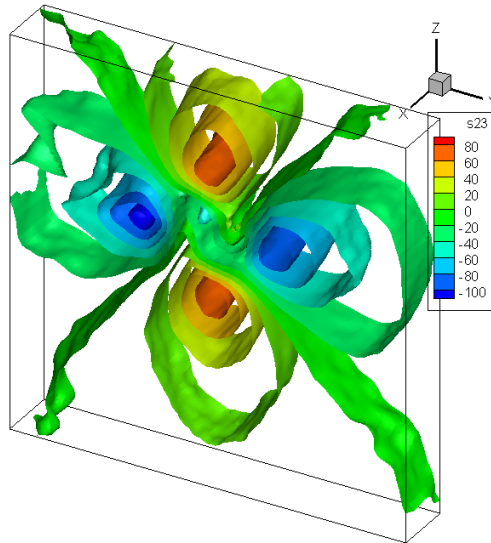
Figure 147: S_{23} iso-surfaces at x=0.400, $\beta = 20°$.
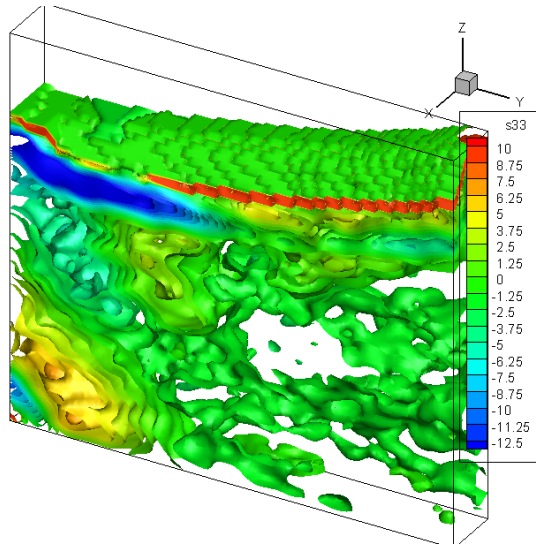
Figure 148: S_{33} iso-surfaces at x=0.400, $\beta = -1°$.
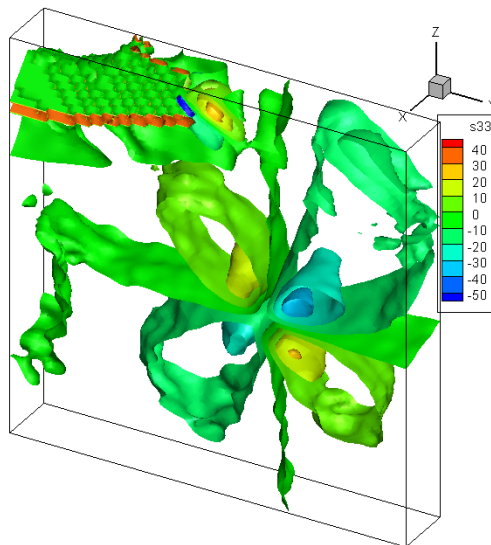
Figure 149: S_{33} iso-surfaces at x=0.400, $\beta = 10°$.
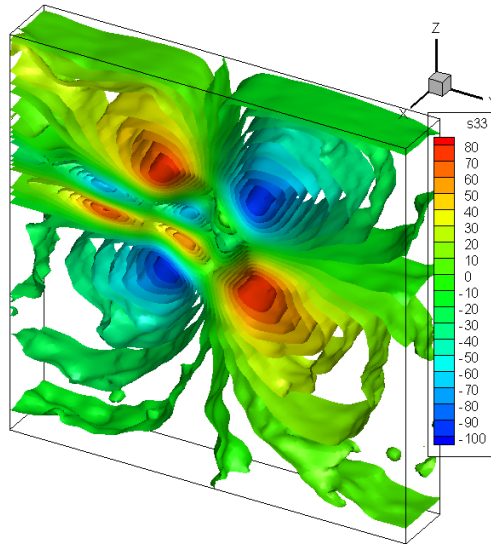
Figure 150: S_{33} iso-surfaces at x=0.400, $\beta = 20°$.
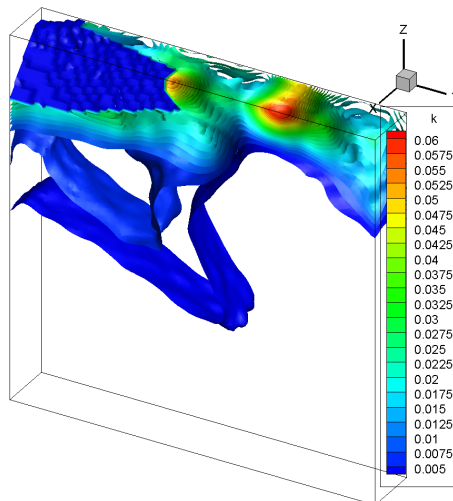
Figure 151: TKE iso-surfaces for β=20°, zone 02 at x=0.400.
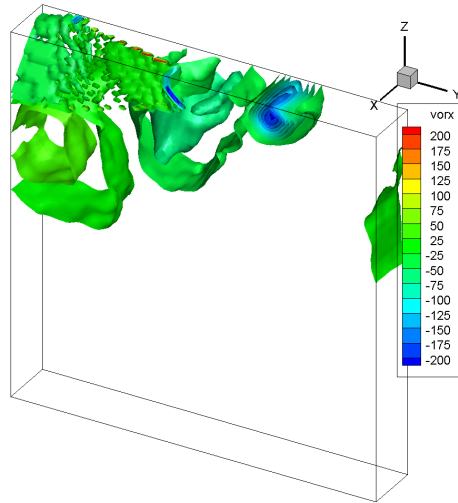
Figure 152: ω_x iso-surfaces for β=20°, zone 02 at x=0.400.
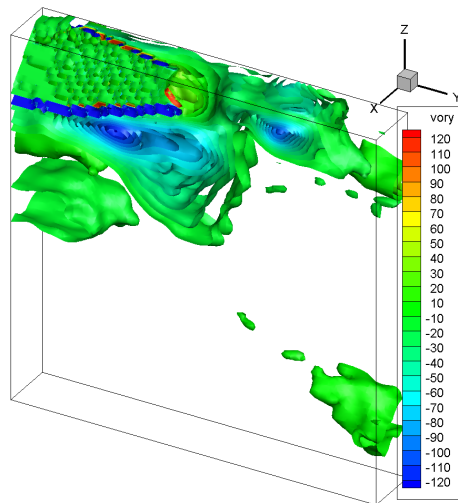
Figure 153: ω_y iso-surfaces for β=20°, zone 02 at x=0.400.
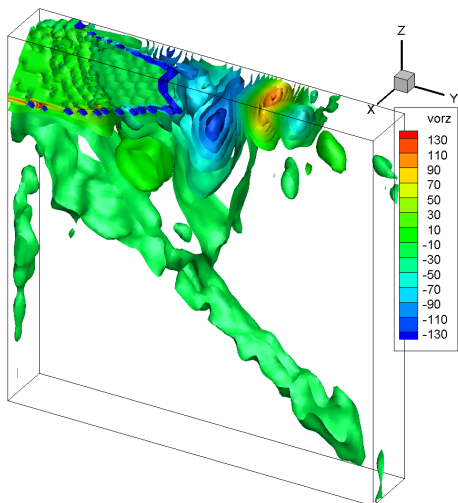
Figure 154: ω_z iso-surfaces for β=20°, zone 02 at x=0.400.
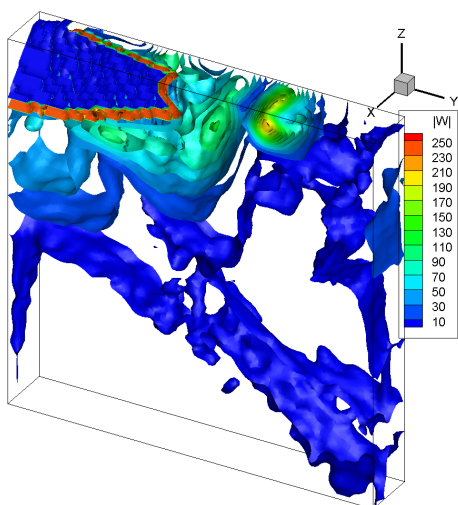
Figure 155: $|\omega|$ iso-surfaces for β=20°, zone 02 at x=0.400.
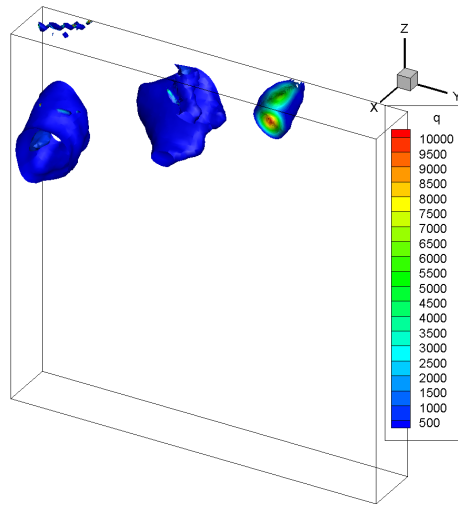
Figure 156: Q iso-surfaces for β=20°, zone 02 at x=0.400.
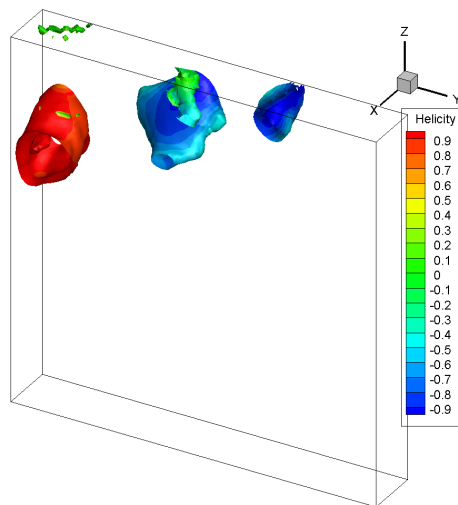
Figure 157: Q iso-surfaces coloured by the H$_N$ for β=20°, zone 02 at x=0.400.
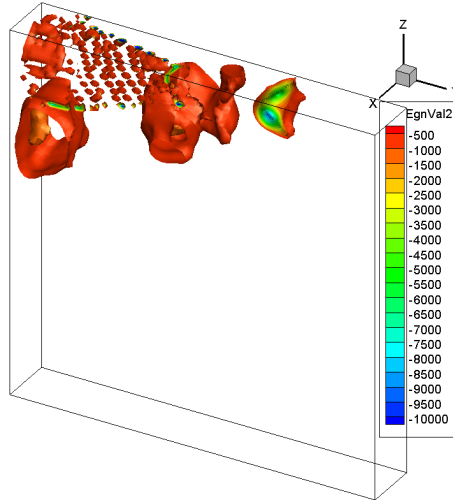
Figure 158: λ_2 iso-surfaces for β=20°, zone 02 at x=0.400.

4.1.2 Instantaneous field

In this section instantaneous quantities will be presented. Focus will be on the vortices, and comparison of instantaneous vortical structures, mainly represented by Q iso-surfaces, with the mean-field structures. Because of the sheer amounts of available data, we are not able to present entire time-series of iso-surfaces, but video compilations will be made available for all drift angles.

Figure 161 shows a selection of instantaneous Q iso-surfaces of β=-1°. The vortical structures that were found from the mean field analysis cannot be distinguished from the plot. The flow field is dominated by small vortex filaments, and it is hard to make out any large-scale swirling motion. However, in the bottom left corner of the domain (exemplified in figures 161h and 161i) strongly oblique vortex filaments, their core lines almost perpendicular to the streamwise direction, indicate the presence of swirling flow. Admittedly, it might have passed undetected had we not known from the mean streamlines and iso-surfaces that large-scale vortices were indeed present.

The spatial organization of the turbulent flow bears a certain similarity to the turbulent boundary layer of a flat plate, although the strain field

from the SDV's influence the small-scale coherent structures. Turbulent boundary layers are dominated by quasi-streamwise vortices and hairpin vortices, observed as single vortices or hairpin packets (Adrian, 2007). The experimental setup unfortunately limits the ability to analyse in detail the development of the small-scale structures in the boundary layer of the model hull. The two major restrictions of the current data set are the frame rate and the orientation of the measurement volume. Since the primary FOV is perpendicular to the main flow direction, we are prevented from fully observing the streamwise development of the flow. Moreover, wall-bounded turbulence is commonly investigated with typical frame rates of $1[kHz]$, a substantial improvement in the temporal resolution of the current study. Nevertheless, some typical features of turbulent boundary layers can be observed. Figure 159 shows a hairpin vortex developing at the hull surface, and Figure 160 we see quasi-streamwise vortices in the outer region of the boundary layer.
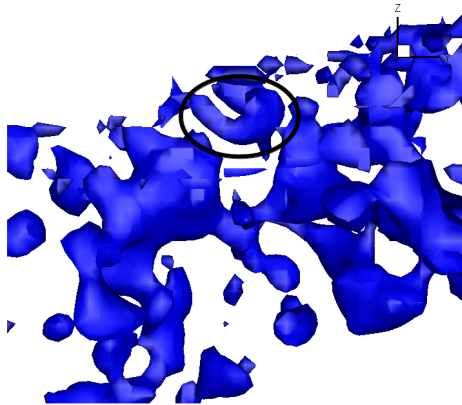
Figure 159: Hairpin structure in the boundary layer, outlined by black ellipse, at β=-1°, x=0.400.
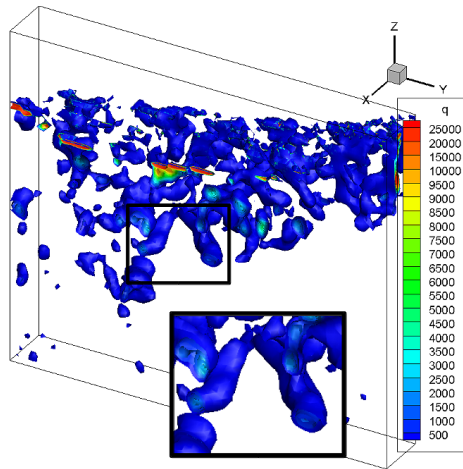
Figure 160: Quasi-streamwise vortices at β=-1°, x=0.400.

(a) t=0.07692[s]   **(b)** t=0.15385[s]   **(c)** t=0.23077[s]

(d) t=0.30769[s]   **(e)** t=0.38462[s]   **(f)** t=0.46154[s]

(g) t=0.53846[s]   **(h)** t=0.61538[s]   **(i)** t=0.69231[s]
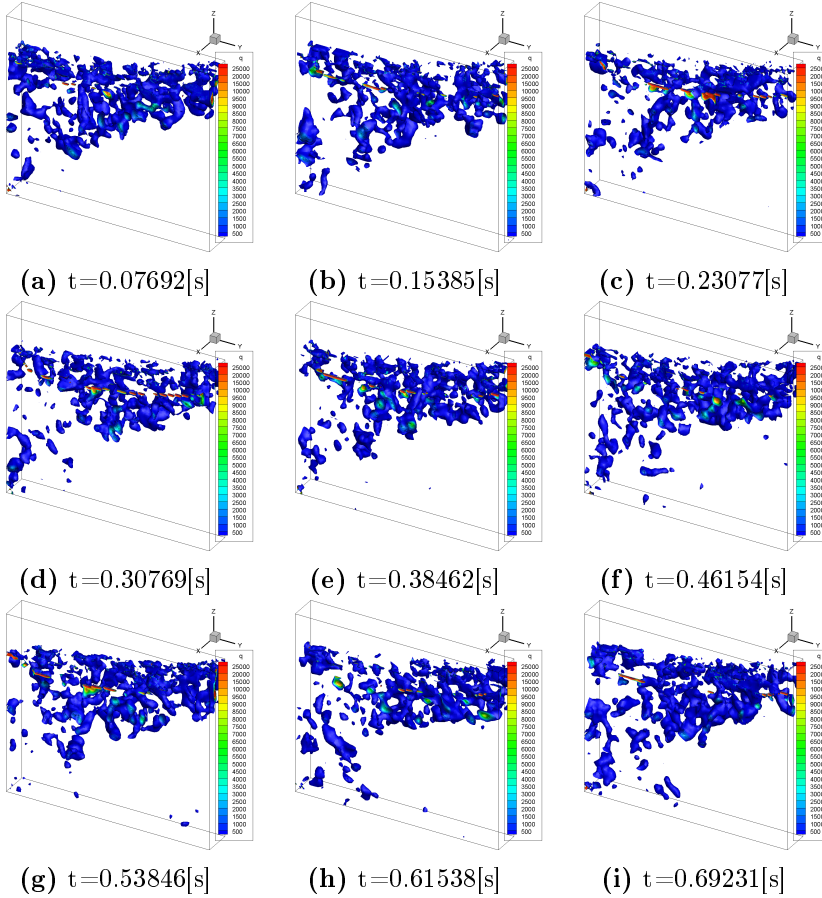
Figure 161: Instantaneous Q iso-surfaces, β=-1°, Run01, x=0.400

The instantaneous structures of β= 10° are shown in fig 163. The SDV is clearly visible from the Q iso-surfaces, and a number of smaller vortex filaments spiral around it. In time, the vortex core region seems to vary periodically between a compact circular tube shape with high values of Q, and a deformed shape where several cores are sometimes seen within the same structure. The deformation of the core region coincides with a dense packing of oblique vortex filaments around it, whereas this clustering is less dense in the case of the compact core shape. Whether this deformation/restoration of the core region is truly a periodic phenomenon must be

decided from analysis of the velocity time series in suitable points, but this is left for future work. In figure 162 we see that the vortex has deformed so that a secondary, weaker core region appears. The primary vortex is surrounded by oblique vortex filaments, with angles of approximately 45° to the primary vortex core line.
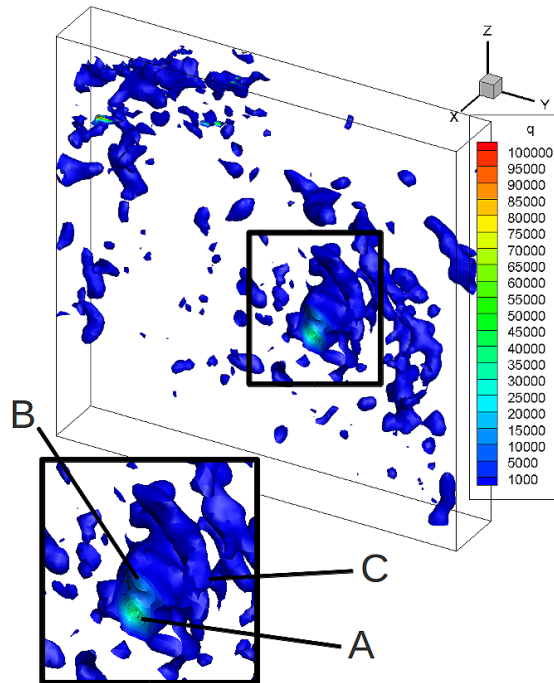
Figure 162: Instantaneous Q iso-surface of $\beta = 10°$, x=0.400. A: primary core. B: secondary core. C: Oblique vortex filament

(a) t=0.07692[s] **(b)** t=0.15385[s] **(c)** t=0.23077[s]

(d) t=0.30769[s] **(e)** t=0.38462[s] **(f)** t=0.46154[s]

(g) t=0.53846[s] **(h)** t=0.61538[s] **(i)** t=0.69231[s]

(j) t=0.76923[s] **(k)** t=0.84615[s] **(l)** t=0.92308[s]
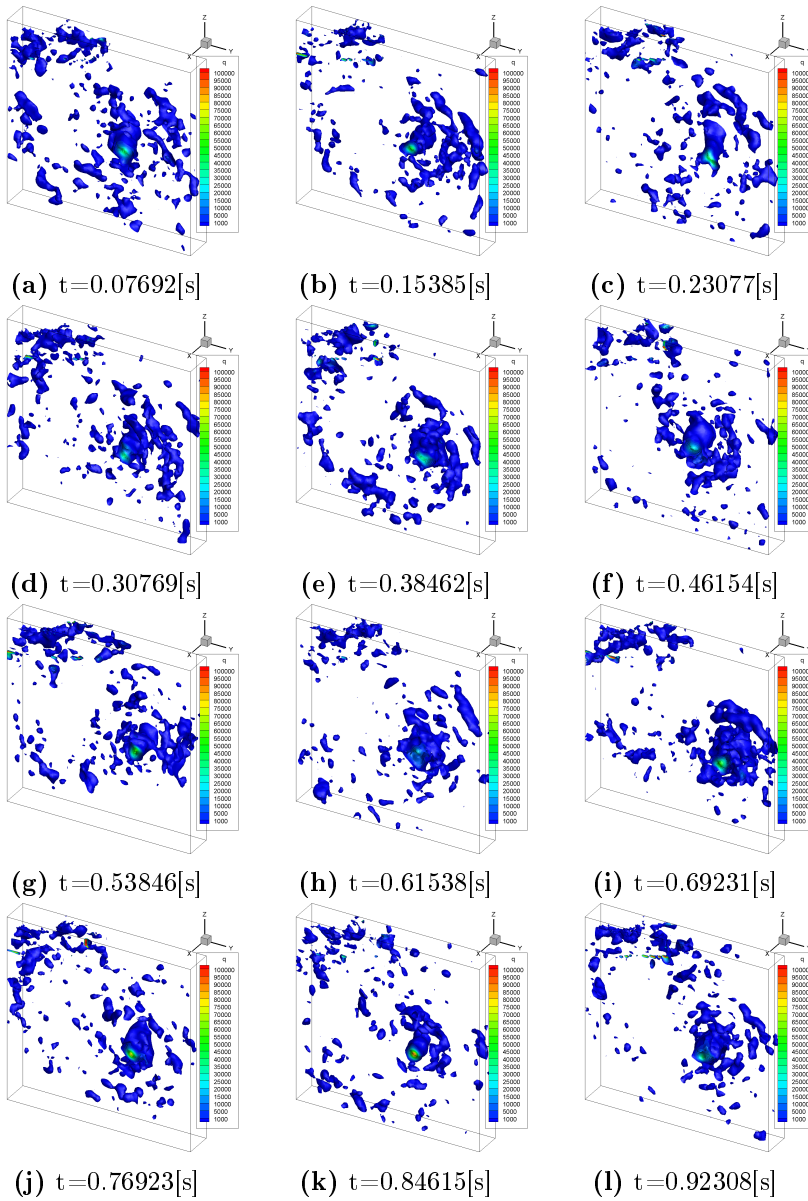
Figure 163: Instantaneous Q iso-surfaces, β=10°, Run01, x=0.400

Now we move on to β=20°. The complicated nature of the SDV, which

132

was partly revealed in the mean field analysis, is apparent from the instantaneous structures(see fig. 164). The swirling region seems to be a conglomeration of several vortex tubes. Instead of a clearly defined core several regions of high Q-values are observed, rotating around a common centre, merging and separating and deforming in time. In addition, numerous weaker vortex filaments swirl around the SDV, their density increasing and decreasing in a seemingly periodic manner. The frequency content of the SDV at β=20° will be examined in section 4.2.

(a) t=0.07692[s]   (b) t=0.15385[s]   (c) t=0.23077[s]

(d) t=0.30769[s]   (e) t=0.38462[s]   (f) t=0.46154[s]

(g) t=0.53846[s]   (h) t=0.61538[s]   (i) t=0.69231[s]
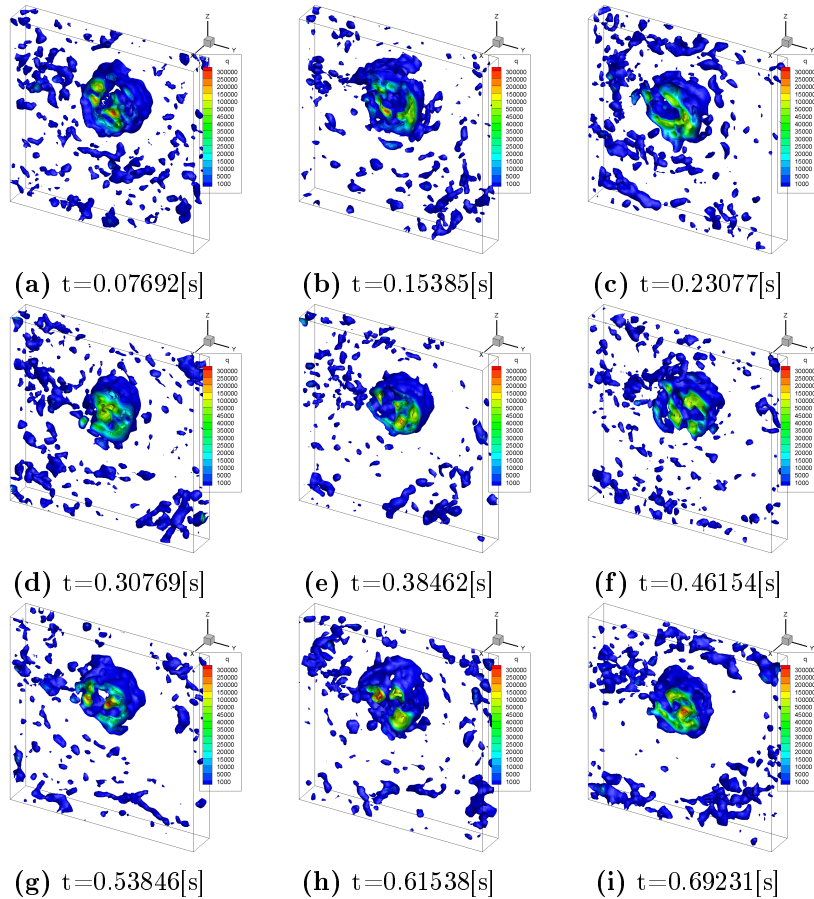
Figure 164: Instantaneous Q iso-surfaces, β=20° zone01, Run01, x=0.400. Detail from fig. 161h

The port- and starboard FBKV and BKV that emerged from the mean Q iso-surfaces are not distinguishable in the instantaneous plots. Instead we observe a complicated mass of smaller vortex tubes with various orientations. The most interesting distinguishable flow feature is a vortex tube stretching diagonally across the region towards the SDV. The tube seems appear and disintegrate with some regularity, and due to its periodic behaviour, it fails to show up in the mean field. We assume that it is created by interaction with the SDV, which is a lot stronger than the vortices in this region. The formation of the diagonal vortex tube seems to coincide with an increase of vortex filament density in the swirling zone around the SDV, with the tube appearing first, and in the next timestep the increase occurs(see fig. 166). This seemingly periodical phenomenon implies as increase of strength in the SDV. This is confirmed by examining the magnitude of Q.

(a) t=0.07692[s]   **(b)** t=0.15385[s]   **(c)** t=0.23077[s]

(d) t=0.30769[s]   **(e)** t=0.38462[s]   **(f)** t=0.46154[s]

(g) t=0.53846[s]   **(h)** t=0.61538[s]   **(i)** t=0.69231[s]
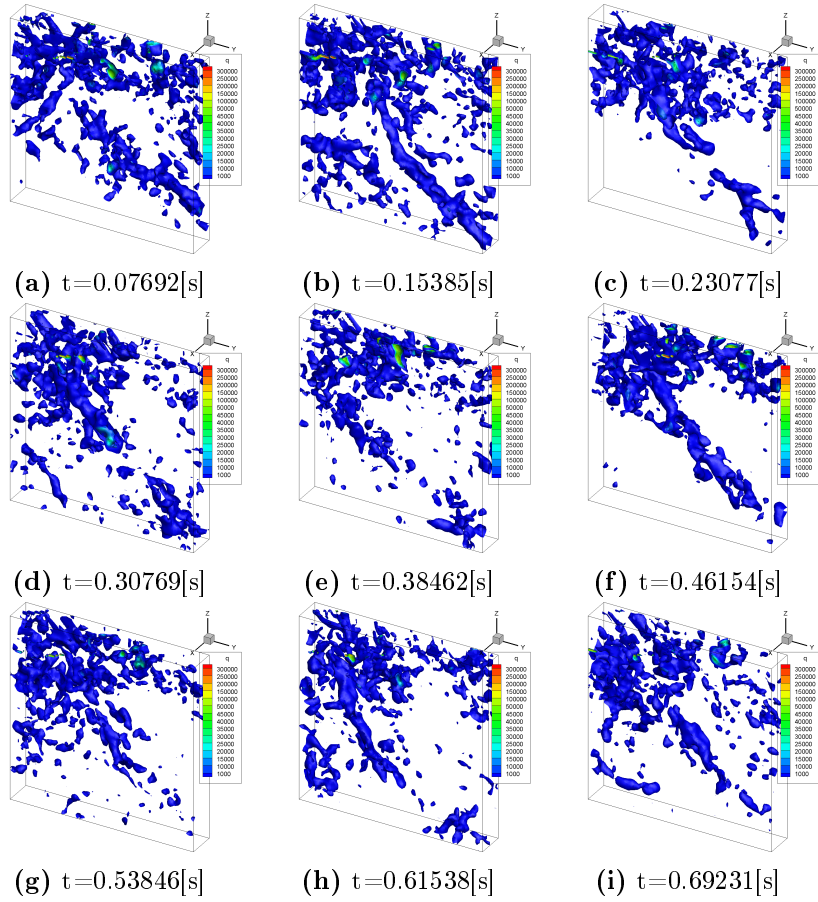
Figure 165: Instantaneous Q iso-surfaces, β=20° zone02, Run01, x=0.400

(a) t=8.30769[s], zone02

(b) t=8.30769[s], zone01

(c) t=8.38462[s], zone02

(d) t=8.38462[s], zone01

(e) t=8.46154[s], zone02

(f) t=8.46154[s], zone01

(g) t=8.53846[s], zone02

(h) t=8.53846[s], zone01
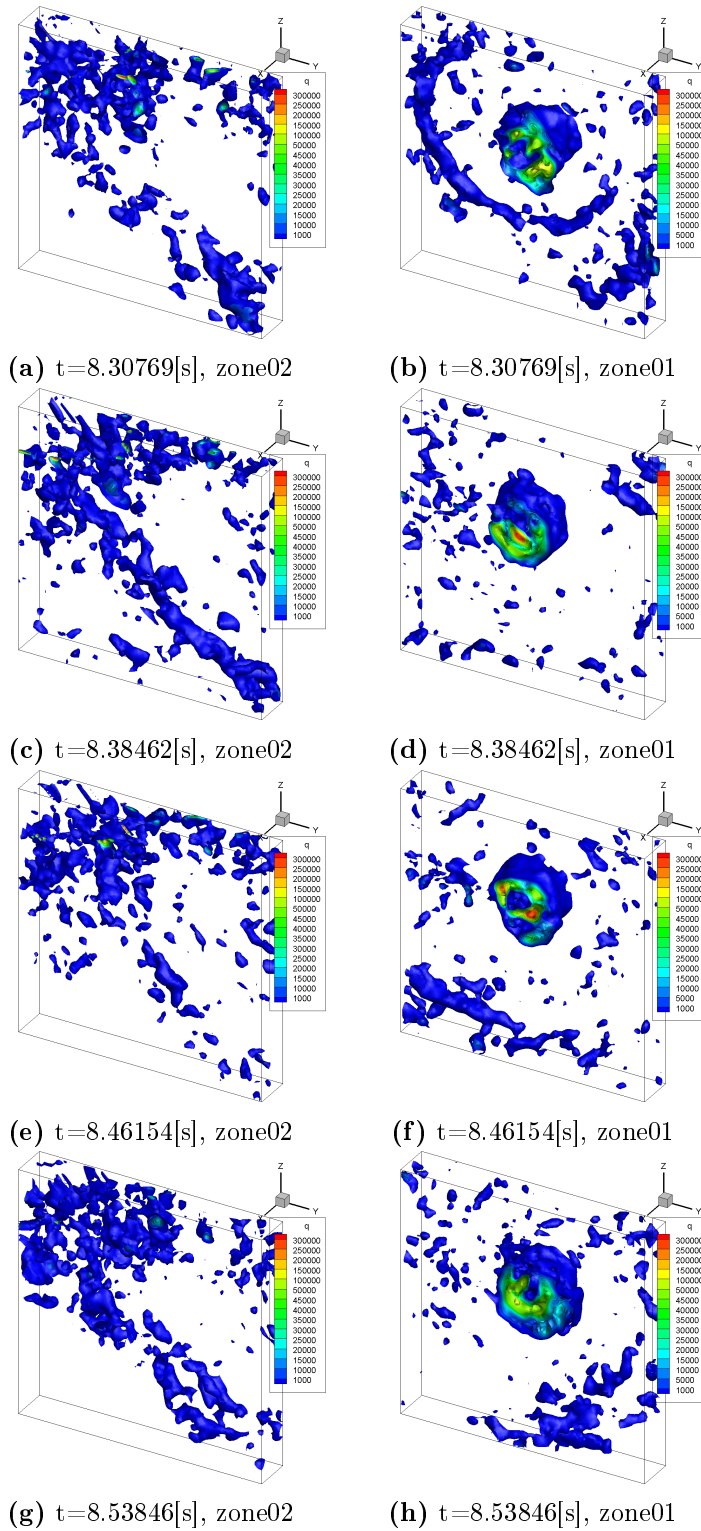
Figure 166: Instantaneous Q iso-surfaces, β=20°, Run01, x=0.400

4.2 Frequency analysis of the SDV at β=20°

CFD analysis (Bhushan, 2010) shows that the SDV at β=20° exhibits helical type instability with a dominant frequency of 2.66[Hz] at x=0.400. The frequency was determined from the pressure fluctuations along the core line of the SDV. To investigate the frequency content of the experimental data, velocity time histories were extracted at five points in the SDV, at six stations along the hull, starting from x=0.060.The points were chosen by visual inspection of the mean Q iso-contours. Point A is the geometrical centre of the structure, and the remaining points are symmetrically distributed around point A. All points are close to the centre-plane of the measurement volume. The configuration of the points are exemplified in figure 167. The coordinates of the points are given for all stations in tables 9 and 10. Based on the configuration of the points chosen for EFD, time-histories of the velocities were also extracted from CFD data(fig 168).
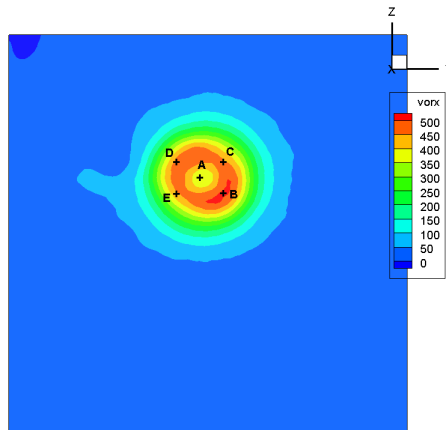
Figure 167: Location of extracted EFD time histories in the SDV at β=20°, x=0.400.

	Point A (x,y,z)	Point B (x,y,z)	Point C (x,y,z)
x=0.060	(0.0595, 0.0223 ,-0.0524)	(0.0595, 0.0223, -0.0544)	(0.0595, 0.0236, -0.0524)
x=0.100	(0.0985, 0.0080, -0.0490)	(0.0985, 0.0093, -0.0503)	(0.0985, 0.0090, -0.0483)
x=0.120	(0.1195, 0.0114, -0.0518)	(0.1195, 0.0141, -0.0537)	(0.1195, 0.0137, -0.0498)
x-0.200	(0.1998, 0.0309, -0.0476)	(0.1998, 0.0326. -0.0489)	(0.1998, 0.0326, -0.0463)
x=0.400	(0.3998, 0.0698, -0.0464)	(0.3998, 0.0675, -0.0447)	(0.3998, 0.0675, -0.0480)
x=0.600	(0.5988, 0.1096, -0.0424)	(0.5988, 0.1112, -0.0444)	(0.5988, 0.1106, -0.0408)

Table 9: EFD points A - C. Locations in the ship coordinate system

	Point D (x,y,z)	Point E (x,y,z)
x=0.06	(0.0595, 0.0193, -0.0527)	(0.0595, 0.0220, -0.0504)
x=0.100	(0.0985, 0.0073, -0.0487)	(0.0985, 0.0070, -0.0500)
x=0.120	(0.1195, 0.0091, -0.0498)	(0.1195, 0.0091, -0.0537)
x=0.200	(0.1998, 0.0293, -0.0460)	(0.1998, 0.0290, -0.0489)
x=0.400	(0.3998, 0.0721, -0.0447)	(0.3998, 0.0721, -0.0480)
x-0.600	(0.5988, 0.1080, -0.0405)	(0.5988, 0.1089, -0.0444)

Table 10: EFD points D and E. Locations in the ship coordinate system
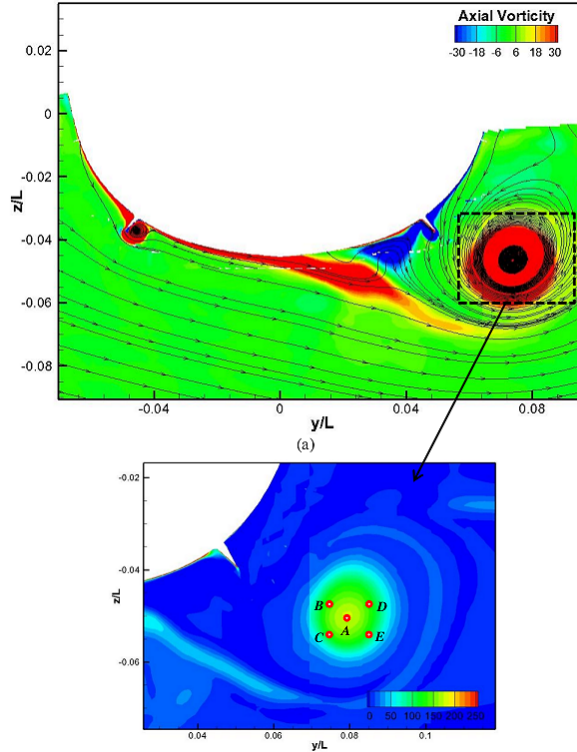
Figure 168: Location of extracted CFD time histories in the SDV at β=20°. From (Bhushan, 2013, fig.2)

In order to eliminate noise and improve the quality of the frequency analysis, POD (see section 2.2.1) has been applied to the experimental data. The velocity fields have been reconstructed using the ten first POD modes as an approximation. The first step in determining any dominant frequencies in the experimental data is to perform an FFT on the POD coefficients themselves. Figure 169 shows the result for x=0.400. Here, the FFT's of all ten coefficients are superimposed, and we clearly see a dominant frequency of approximately 3[Hz]. Next we investigate the frequency content of the reconstructed velocity components. FFT's of the velocity components at point A for x=0.400 are shown in figures 170, 171 and 172. For the FFT's, all five runs are superimposed in one plot, and frequency peaks that coincide for all five runs are considered to be actual dominant

frequencies. For clarity, the time history is only shown for one repetition of the experiment. Although it is not as clearly defined as the peak of the POD coefficients, a dominant frequency of about $3[Hz]$ is observed for V and W at x=0.400. There is no clear peak for U. Similar figures for the remaining points, and for all points at the remaining stations are given in the appendices (see Appendix B). The overall results show that there is no dominant frequency detected for U at any station. The dominant frequency of W is ~ 3 $[Hz]$ for stations x=0.060 - 0.400, and at x=0.400 there are secondary peaks at ~ 2.3 $[Hz]$ and ~ 4.2 $[Hz]$. For stations x=0.060, 0.100 and 0.400, the dominant frequency of V found to be $\sim$ 3 $[Hz]$. However, for x=0.120 and 0.200 there is no clear dominant frequency for V. CFD analysis gives a somewhat different picture (Bhushan, 2013). No dominant frequencies were found for the U component, but there was frequency content for V and W. The dominant frequencies determined numerically seem to be increasing towards the bow, whereas the experimental data gives similar frequencies at all stations. At x=0.400 the CFD result is similar to EFD, predicting dominant frequencies of 2.35 - $3.13[Hz]$ for V and W. For x=0.200 the dominant frequency is $\sim 4[Hz]$ and at x=0.120 it has increased to $\sim 6[Hz]$. At x=0.100 it is in the range of 6-8$[Hz]$. No dominant frequency was found for x=0.060. Moreover, the numerical predictions indicate that the inception of the SDV does not occur until after x=0.060(see fig. 173). Ideally, this should be investigated further by more detailed experiments at station x=0.060 and immediately downstream. Because of the highly unstable nature of the flow, we cannot expect the exact same result from the experimental- and the numerical analysis. Small perturbations, such as vibration in the towed experimental setup, can cause significant changes in the flow.
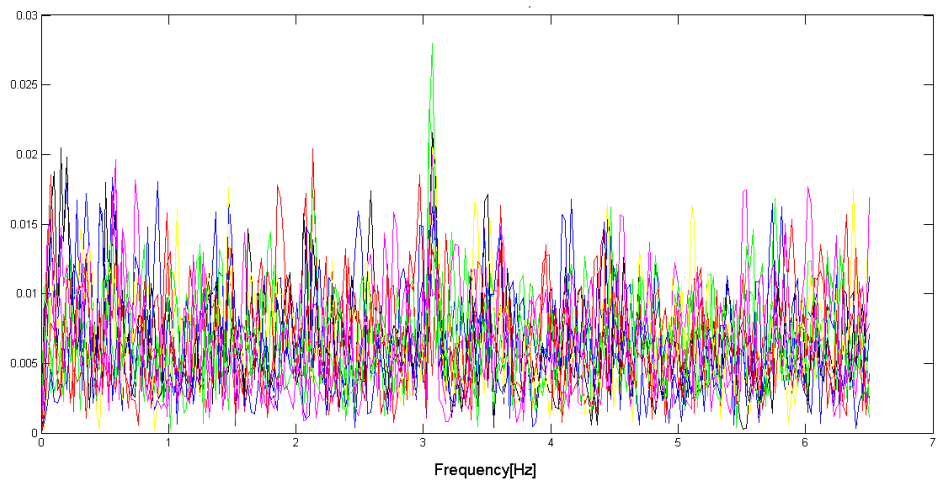
Figure 169: FFT of first ten POD coefficients, x=0.400.
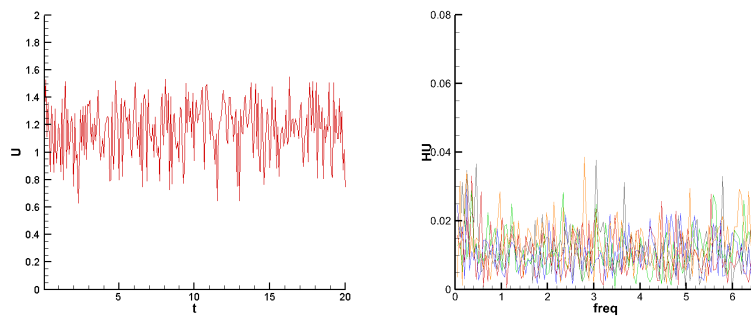
Figure 170: U time history and FFT at point A, x=0.400.
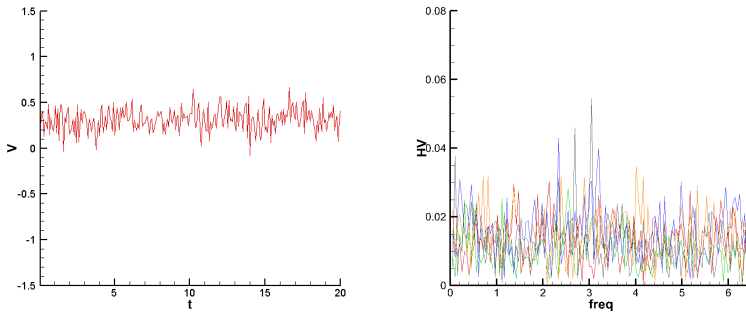
Figure 171: V time history and FFT at point A, x=0.400.
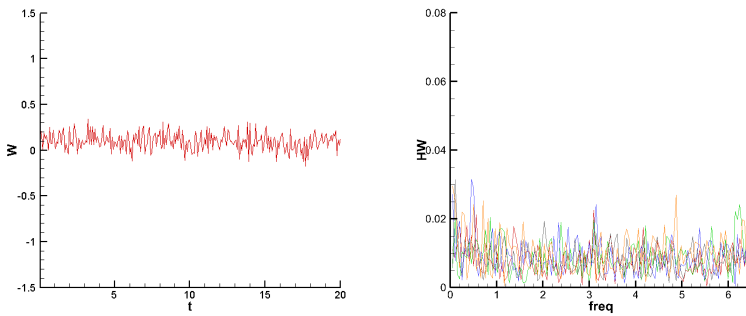
Figure 172: W time history and FFT at point A, x=0.400.
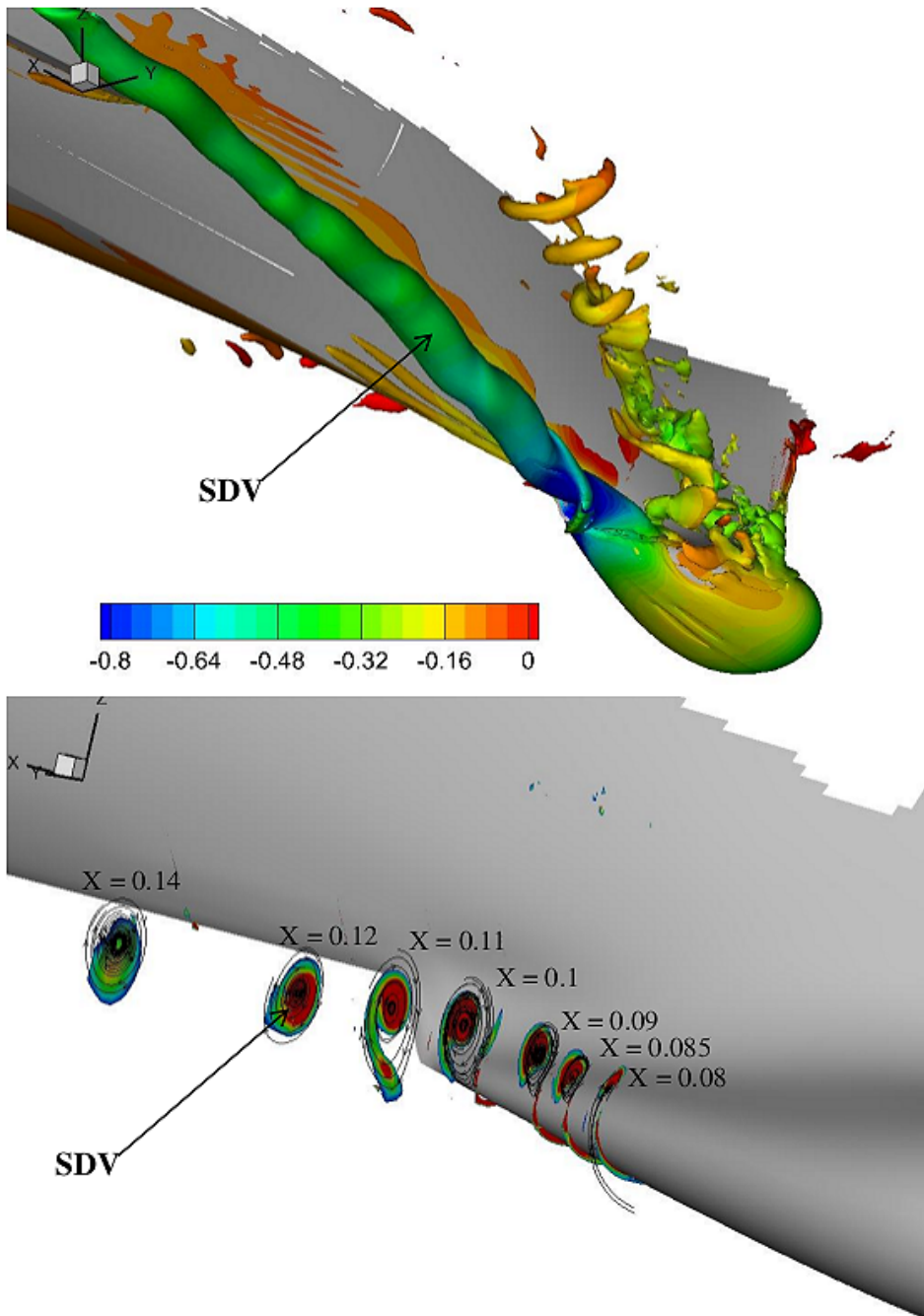
Figure 173: Inception and progression of the SDV at $\beta{=}20°$, as predicted by CFD analysis. From Bhushan (2013, Fig. 2).

5 Conclusions and further work

In this work the vortex system of the surface combatant model DTMB 5512 (geosym of DTMB 5415) has been investigated for drift angles -1°, 10° and 20°. The measurement data was obtained by means of tomographic PIV. An overview of the onset and progression of the vortices has been given for all measurement stations, and detailed volume analysis has been conducted for x=0.400.

For β=-1°, two major vortices are found, the SDV and the FBKV. There is also evidence of a vortex forming at the bilge keel at x=0.600. The angle -1° was chosen as being closest to the neutral angle, when it was discovered that 0° gave asymmetry of the flow field. It turns out that the flow still has some asymmetry, which manifests in the presence of the port side SDV in the measurement volume. Had the flow been exactly symmetrical, the vortices would have no drift angle. CFD analysis does not register a BKV at this drift angle, which might mean that this vortex is caused by the asymmetry of the experimental setup. Rigorous neutral angle tests have been performed, but too late be incorporated into the current study.

For β=10° the SDV is dominant. The windward and leeward SDV's merge at some point between x=0.120 and x=0.200. a BKV can be observed at x=0.600, but merges quickly with the stronger SDV. The displacement of the SDV with respect to the ship centreline increases as we move downstream, but it never leaves the measurement domain. At x=0.935 the BKV-WW, which was not observed at other stations, has drifted close to the centreline. In addition, a vortex has formed on the after-body, called the ABKV.

The major vortices of β=20° are the SDV, FBKV and FBKV-WW. Only one SDV is observed, and it is assumed that the SDV-WW dissipates rapidly because of the strain from the strong crossflow at this drift angle. THe inception the the FBKV's is around x=0.200, and it is assumed that they either dissipate or merge with the stronger SDV at some point between x=0.400 and x=0.600. Vortices form on both bilge keels at x=0.400. The leeward BKV persists until somewhere between x=0.600 and x=0.800. At x=0.800 the BKV-WW has drifted close to the centreline, and we see the early formation of a vortex on the after-body. The ABKV still persists at x=0.935. The SDV drifts out of the domain after x=0.600 so further

measurements are needed to determine its characteristics downstream of this point.

It is seen that the inception of vortices is hard to determine, due to laser reflections from the hull surface. The TPIV system was not able to register the vortical structures until they had separated from the hull. For β=-1° and 10° there are no indication of vortical structures at x=0.060, but for β=-1° there are signs of a weak vortex close to the sonar dome, which is assumed to be the SDV. This is supported by frequency analysis of the velocity components at the assumed location of the vortex core, which indicates a dominant frequency of 3[Hz]. However, CFD analysis performed by Bhushan (2013) indicate that the onset of the SDV occurs further downstream than x=0.060. Thus, the nature of this structure should be investigated in more detail.

From the volume analysis at x=0.400, it is seen that the strength and size of the vortices increase with the drift angle. Reynolds stresses and strain predictably increase, and it is seen that for the two larger drift angles, their maxima are located in the vicinity of the SDV. At β=-1°, the close proximity of the ship hull influences the distribution and value of the Reynolds stresses and strains. Another factor of influence is the presence of the port side SDV, which alters the strain field.

The vorticity is computed, and it is observed that for β=10° and 20° ω_x dominates the other components. For β=-1° the magnitude of the vorticity components are of the same order.

Iso-surfaces of Q>0 and λ_2<0 are used to identify vortical structures. There seems to be little difference between them when computing mean values, although λ_2 appears to be more sensitive to the measurement noise close to the model surface. For the instantaneous iso-surfaces there are some minor differences. λ_2 seems to capture more of the small vortex filaments, but the major trends are similar.

One of the purposes of this study was to provide recommendations for further volume analysis within the DTMB 5415 project at IIHR. It is concluded that TKE, vorticity and Q (with λ_2 for comparison) are the most useful variables for comparison with CFD analysis. This is because they hold a lot of information about the flow in a compact form. Q, for example, indicates the balance between vorticity and strain in the flow, whereas TKE will give a measure of the turbulent stresses. Vorticity,

although contained within Q, is so common for comparisons that leaving it out would be contra-intuitive to most. Moreover, the fact that the use of TPIV allows us to compute all vorticity components from experimental data, makes comparison with numerical analysis more interesting.

The instantaneous iso-surfaces of Q were investigated for all drift angles. For β=-1° the structures found from the mean flow were not immediately apparent. The flow behaviour is somewhat similar to that of a turbulent flat-plate boundary layer, although it is influenced by the strain field from the SDV's. Typical features of a turbulent boundary layer, such as quasi-streamwise vortices and hairpin vortices can be observed.

For β=10° the SDV is the dominant feature of the instantaneous flow, and a number of smaller vortex filaments spiral around it. The core of the SDV is seen to deform in a seemingly periodical manner, sometimes developing secondary core lines within the main structure. This deformation coincides with a weakening of the SDV strength (lower Q values), and a tight clustering of oblique vortex filaments around the core. For future work, FFT analysis is recommended for the SDV at this drift angle to investigate any dominant frequencies that might be related to the deformation behaviour.

Two zones are investigated for β=20°: the measurement volume containing the SDV (zone01), and the one containing the FBKV, FBKV-WW and the BKV (zone02). The SDV is the dominant instantaneous flow feature. The FBKV's and BKV cannot be distinguished from the instantaneous Q iso-surfaces. There is clearly interaction between the strong SDV and the weaker vortical structures, and some periodicity is indicated for this interaction. A number of small vortex filaments swirl around the SDV, and they seem to be drawn from zone02. Also, a larger vortex tube, stretching diagonally from the upper left corner, which coincides with the approximate mean position of the FBKV's, to the lower corner of zone01 appears with some regularity. This implies that there is a fluctuation of strength in the SDV. This is confirmed by the Q magnitude in the SDV core region.

The frequency content of the SDV β=20° is investigated by means of FFT analysis of the velocity components, and compared with CFD analysis. Stations x=0.06-0.600 are investigated for EFD and x=0.06 - 0.400 for CFD. Neither EFD nor CFD predict any dominant frequencies for U at

any stations. CFD predicts a steady decrease in the dominant frequency of V and W, from 6-8[Hz] at x=0.100 to 2.35-3.13[Hz] at x=0.400. no dominant frequencies were predicted at x=0.060 for CFD. EFD data shows a dominant frequency of aproximately 3[Hz] for stations x=0.060-0.400, while no dominant frequency is found for x=0.600. It is assumed that the difference between the EFD and CFD result is due to the unsteady nature of the flow. Small disturbances that are ever present in the experimental environment, but blessedly absent for CFD, can quickly case transition from one flow state to another.

For future work, it is recommended that measurements be taken with a higher sampling frequency, inasmuch as this is possible, in order to get a better resolution of the instantaneous structure in the flow. Also, the progression of the vortices along the hull could be better determined by adding measurement stations in between for example x=0.200 and x=0.400, as well as between x=0.400 and 0.600. It seems that some very interesting vortex dynamics , merging and breakdown, happens in between these stations. Naturally, any expansion of the project depends on the resources available. The overall aim of the EFD work is to provide validation data for CFD, so it a decision must be made whether the available resolution in time and space is sufficient for this purpose, but those considerations are beyond the scope of the current work.

6   Bibliography

R. J. Adrian. Hairpin Vortex Organization in Wall Turbulence. *Physics of Fluids*, 19:041301, 2007.

R. J. Adrian and J. Westerweel. *Particle Image Velocimetry*. Cambridge University Press, 2011.

Y. M. Ahmed. Numerical simulation for the free surface flow around a complex ship hull form at different Froude numbers. *Alexandria Engineering Journal*, 50(3):229–235, 2011.

H. Amini and S. Steen. Shaft loads on azimuth propulsors in oblique flow and waves. *International Journal of Maritime engineering*, 153(1): A9–A21, 2011.

D. C Banks and B. A. Singer. Vortex Tubes in Turbulent Flows:Identification, Representation, Reconstruction. In *Proceedings of IEEE Visualization 1994*, pages 132–129, 1994.

G. Berkooz, P. Holmes, and J. L. Lumley. The proper orthogonal decomposition in the analysis of turbulent flows. *Annual Review of Fluid Mechanics*, 25:539, 1993.

P. S. Bernard. Basic Phyics. In R. W. Johnson, editor, *The Handbook of Fluid Mechanics*, chapter 13, pages 13–4. Springer/CRC Press, 1998.

P. S. Bernard, J. M. Thomas, and R. A. Handler. Vortex Dynamics and the production of Reynolds Stress. *Journal of Fluid Mechanics*, 253: 385–419, 1993.

S. Bhushan. DES SIMULATION FOR STATIC DRIFT AT 20° DTMB 5415 WITH BILGE KEELS USING CFDSHIP-IOWA V.4. work report, August 2nd 2010.

S. Bhushan. Velocity Time History and FFT in SDV Core. work report, April 2013.

S. Bhushan and F. Stern. Onset and Progression of Vortical Structures for Static Drift 5415 at $\beta = 20°$. work report, September 19th 2012.

S. Bhushan, P. Carrica, J. Yang, and F. Stern. Scalability studies and large grid computations for surface combatant using CFDShip-Iowa. *International Journal of High Performance Computing Applications*, 25(4): 466–487, 2011.

S. Bhushan, T Xing, T. M Visonneau, J. Wackers, G. Deng, F. Stern, and L. Larsson. Chapter 7: Post Gothenburg 2010 Workshop Computations and Analysis for KVLCC2 and 5415. work report, February 20th 2013.

D. K. Bisset, R. A. Antonia, and L. W. B Browne. Spatial organization of large structures in the turbulent far wake of a cylinder. *Journal of Fluid Mechanics*, 218:439–461, 1990.

C. Brucker. Digital-Particle-Image-Velocimetry (DPIV) in a scanning light-sheet: 3D starting flow around a short cylinder. *Experiments in Fluids*, 19:255–263, 1995.

N. A. Buchmann, C. Atkinson, and J. Soria. Tomographic PIV investigation of coherent structures in a turbulent boundary layer flow. In *15th Int Symp on Applications of Laser Techniques to Fluid Mechanics, Lisbon, Portugal*, 2010.

A.-J. Buchner, N. Buchmann, K. Kilany, C. Atkinson, and J. Soria. Stereoscopic and Tomographic PIV of a pitching plate. *Experiments in Fluids*, 52:299–314, 2012.

B. J. Cantwell. Organized motion in turbulent flow. *Annual Review of Fluid Mechanics*, 13:457, 1981.

P. Chakraborty, S. Balachandar, and R. J. Adrian. On the relationships between local vortex identification schemes. *Journal of Fluid Mechanics*, 535:189–214, 2005.

M. S. Chong, A. E. Perry, and B. J. Cantwell. A general classification of three-dimensional flow fields. *Physics of fluids A*, 2:765–777, 1990.

J. W. Cooley and J. W. Tukey. An Algorithm for the Machine Computation of the Complex Fourier Series. *Mathematics of Computation*, 19:297–301, 1965.

R. De Kat and B. W. Van Oudheuseden. Instantaneous planar pressure determination from PIV in turbulent flow. *Experiments in Fluids*, 52: 1089–1106, 2012.

D. Donnelly and B. Rust. The Fast Fourier Transform for Experimentalists, Part I: Conecpts. *Computing in Science and Engineering*, 7(5):80–88, 2005.

G. Dubbioso, R. Muscari, and A. Di Mascio. Analysis of the performances of a marine propeller operating in oblique flow. *Computers and Fluids*, 75:86–102, 2013.

G. E. Elsinga, C. Poelma, A. Schröder, R. Geisler, and J. Scarano, F.and Westerweel. Tracking of vortices in a turbulent boundary layer. *Journal of Fluid Mechanics*, 697:273–295, 2012.

G.E. Elsinga, F. Scarano, B. Wieneke, and B.W. Van Oudheusden. Tomographic particle image velocimetry. *Experiments in Fluids*, 41:933–947, 2006.

S.-Y. Fan and S.-K. Lu. Experimental study and numerical calculation of hydrodynamic forces and moments acting on a high-speed transomstern ship running oblique to the course. *Journal of Hydrodynamics*, 3(1): 1–10, 1991.

L.-H. Feng, J.-J. Wang, and C. Pan. Proper orthogonal decomposition analysis of vortex dynamics of a circular cylinder under synthetic jet control. *Physics of Fluids*, 23:014106, 2011.

M. Frigo and S. G. Johnson. FFTW: An Adaptive Software Architecture for the FFT. In *Proceedings of the International Conference on Acoustics, Speech, and Signal Processing*, volume 3, pages 1381–1384, 1998.

L. Gui, J. Longo, B. Metcalf, J. Shao, and F. Stern. Forces, moment, and wave pattern for surface combatant in regular head waves. Part I. Measurement systems and uncertainty assessment. *Experiments in Fluids*, 31(6):674 –680, 2001.

R. Hain, C. J. Kähler, and D. Michaelis. Tomographic and time resolved PIV measurements on a finite cylinder mounted on a flat plate. *Experiments in Fluids*, 45:715–724, 2007.

G. Haller. An objective definition of a vortex. *Journal of Fluid Mechanics*, 525:1–26, 2005.

K. D Hinsch. Holographic particle image velocimetry. *Measurement Science and Technology*, 13:R61–R72, 2002.

T Hori and J. Sakakibara. High-speed scanning stereoscopic PIV for 3D vorticity measurement in liquids. *Measurement Science and Technology*, 15:1067–1078, 2004.

J. Huang and B. Feng. Investigation on optimization strategies for the hydrodynamic design of DTMB 5415. In *3rd international Conference on Manufacturing Science and Engineering, ICMSE 2012;Xiamen*, volume 479-481, pages 1950–1954, 2012.

J. C. R. Hunt. Vorticity and vortex dynamics in complex turbulent flows. *Canadian Society for Mechanical Engineering, Transactions*, 11(1):21–35, 1987.

J. C. R. Hunt, A. A. Wray, and P. Moin. Eddies, stream and convergence zones in turbulent flows. *Center for Turbulence Research Report CTR-S88*, pages 193–208, 1988.

A. K. M. F. Hussain and M. Hayakawa. Eduction of large-scale organized structures in a turbulent plane wake. *Journal of Fluid Mechanics*, 180: 193–229, 1987.

M. Irvine Jr., J. Longo, and F. Stern. Pitch and heave tests and uncertainty assessment for a surface combatant in regular head waves. *Journal of Ship Research*, 52(2):146 –153, 2008.

ITTC. Report of performance Committee. In *15th International Towing tank Conference, Hague, the Netherlands*, pages 364–366, 1978.

ITTC. In *23rd International Towing tank Conference, Seoul,Korea/Beijing,China*, 2002.

J. Jeong and F. Hussain. On the identification of a vortex. *Journal of Fluid Mechanics*, 25:69–94, 1995.

C. J. Khäler and J. Kompenhaus. Fundamentals of multiple plane stereo particle image velocimetry. *Experiments in Fluids*, Suppl:S70–S77, 2000.

H. Kim, C. Yang, and F. Noblesse. Hull form optimization for reduced resistance and improved seakeeping via practical designed-oriented CFD tools. In *Grand Challenges in Modeling and Simulation Symposium, GCMS 2010 - Proceedings of the 2010 Summer Simulation Multiconference, SummerSim 2010*, volume 3, pages 375 –385, 2010.

K. Kume, J. Hasegawa, Y. Tsukada, J. Fujisawa, R. Fukasawa, and M. Hinatsu. Measurements of hydrodynamic forces, surface pressure, and wake for obliquely towed tanker model and uncertainty analysis for CFD validation. *Journal of Marine Science and Technology*, 11(2):65–75, 2006.

L. Larsson. SSPA-ITTC workshop on ship boundary layers. Technical Report 90, Swidish State Shipbuilding Experiment tank, Gothenburg, Sweden, 1981.

L. Larsson, F. Stern, and V. Bertram. Benchmarking of Computational Fluid Dynamics for Ship Flows: The Gothenburg 2000 Workshop. *Journal of Ship Research*, 47(1):63–81, 2003.

Y. Levy, D. Degani, and A. Seigner. Graphical Visualization of Vortical Flows by Means of Helicity. *AIAA Journal*, 28(8):1347–1352, 1990.

Y. C. Liang, H. P. Lee, S. P. Lim, W. Z. Lin, K. H. Lee, and C. G. Wu. Proper Orthogonal Decomposition and its Applications-Part I:Theory. *Journal of Sound and Vibration*, 252(3):527–544, 2002.

J. Logo, J. Shao, M. Irvine, and F Stern. Phase-Averaged PIV for the Nominal Wake of a Surface Ship in Regular Head Waves. *Journal of Fluids Engineering*, 129:524–540, 2007.

J. Longo and F. Stern. Effects of drift angle on model ship flow. *Experiments in Fluids*, 32:558–569, 2002.

J. Longo and F Stern. Uncertainty Assessment for Towing Tank Tests With Example for Surface Combatant DTMB Model 5415. *Journal of Ship Research*, 49(1):55–68, 2005.

H. J. Lugt. The dilemma of defining a vortex. In *Recent Devopments in theoretical and Experimental Fluid Mechanics*, pages 309–321, 1979.

D. Lyon. The Discrete Fourier Transform, Part 4: Spectral Leakage. *Journal of Object Technology*, 8(7):23–34, 2009.

O. Marcu and A. Lungu. Numerical investigation of the flow around the KVLCC2 hull in static drift motion. In *NUMERICAL ANALYSIS AND APPLIED MATHEMATICS ICNAAM 2012: International Conference of Numerical Analysis and Applied Mathematics*, pages 185–188, 2012.

B. McKeon, G. Comte-Bellot, and J. Foss. Velocity, Vorticity and Mach number. In C. Tropea, A. L. Yarin, and J. F. Foss, editors, *Springer Handbook of Experimental Fluid Mechanics*, chapter 2.3, page 289. Springer, 2007.

P. Meunier, S. Le Dizes, and T. Lweke. Physics of vortex merging. *Comptes Rendus Physique 6*, 4(5):431–450, 2005.

K. E. Meyer, J. M. Pedersen, and O. Özcan. A turbulent jet in cross-flow analysed with proper orthogonal decomposition. *Journal of Fluid Mechanics*, 583:199, 2007.

K. Meyne and A. Nolte. EXPERIMENTAL STUDIES OF THE HYDRO-DYNAMIC FORCES AND MOMENTS ACTING ON ONE BLADE OF A SHIP'S PROPELLER AT AN OBLIQUE ANGLE OF FLOW. *SCHIFF U HAFEN*, 21(5):–, 1973.

F.J. Moraga, P.M. Carrica, D.A. Drew, and R.T. Lahey Jr. A sub-grid air entrainment model for breaking bow waves and naval surface ships. *Computers and Fluids*, 37(3):281–298, 2008.

R. Muscari and A. Di Masco. Numerical modeling of breaking waves generated by a ship's hull. *Journal of marine science and technology*, 9(4): 158 –170, 2004.

G. Neumann and W. J. Pierson. *Principles of Physical Oceanography*. Prentice Hall, 1966.

A. Olivieri, F. Pistani, R. Wilson, E. F. Campana, and F. Stern. Scars and Vortices Induced by Ship Bow and Shoulder Wave Breaking. *Journal of Fluids Engineering*, 129:1445–1459, 2007.

F. Pereira and M. Gharib. Defocusing digital particle image velocimetry and the three-dimensional characterization of two-phase flows. *Experiments in fluids*, 12:353–358, 2002.

D. Peri and E.F. Campana. Multidisciplinary design optimization of a naval surface combatant. *Journal of Ship Research*, 47(1):1–12, 2003.

A. B. Phillips, S. R. Turnlock, and F. Maaten. Evaluation of manoeuvring coefficients of a self-propelled ship using a blade element momentum propeller model coupled to a Reynolds averaged Navier Stokes flow solver. *Ocean Engineering*, 36:1217–1225, 2009.

A. K. Prasad. Stereoscopic particle image velocimetry. *Experiments in fluids*, 29:103–116, 2000.

W. H. Press, S. A. Teukolsky, W. T. Vetterling, and B. P. Flannery. *Numerical Recipes in FORTRAN 77: the Art of Scientific Computing*. Cambridge University Press, 1992.

S. K. Robinson. Coherent Motions in the Turbulent Boundary Layer. *Annual Review of Fluid Mechanics*, 23:601–639, 1991.

O. Rutgersson. Cavitation on high speed propellers in oblique flow-influence of propeller design and interaction with ship hull. *GOTENBURG, SWEDEN, SWEDISH MARIT. RES. CENTRE*, 89:44, 1981.

J. Sahner. *Extraction of Vortex Structures in 3D Flow Fields*. PhD thesis, Fakultät für Informatik der Otto-von-Guericke-Universität Magdeburg, 2009.

J. Sahner, T. Weinkauf, and H. C. Hege. Galilean Invariant Extraction and Iconic Representation of Vortex Core Lines. In *EUROGRAPHICS - IEEE VGTC Symposium on Visualization (2005)*, 2005.

T. Sasajima and T. Muruhashi. Performance of highly skewed controllable pitch propellers for high speed twin screw vessels, 1980.

F. Scarano and C. Poelma. Three-dimensional vorticity patterns of cylinder wakes. *Experiments in Fluids*, 47(1):69–83, 2009.

T. Schafhitzel, J.E. Vollrath, J. P. Gois, D. Weiskopf, A. Castelo, and T. Ertl. Topology-Preserving λ_2-based Vortex Core Line Detection for Flow Visualization. In *Proceedings of Eurographics/ IEEE-VGTC Symposium on Visualization 2008*, volume 27(3), pages 1023–1030, 2008.

A. Schröder and J. Kompenhaus. Investigation of a turbulent spot using multi-plane stereo particle image velocimetry. *Experiments in Fluids*, 36:82–90, 2004.

A. Schröder, R. Geisler, G. E. Elsinga, F. Scarano, and U. Dierksheide. Investigation of a turbulent spot and a tripped turbulent boundary layer flow using time-resolved tomographic PIV. *Experiments in Fluids*, 44(2): 305–316, 2008.

L. Schäfer and W. Schröder. Comparison of holographic and tomographic particle image velocimetry turbulent channel flow measurements. In *13th European Turbulence Conference (ETC13)*, 2011.

L. Sirovich. Turbulence and the dynamics of coherent structures. Part I: Coherent structures. *Quarterly of Applied Mathematics*, 45:561, 1987.

F. Stern, J. Longo, R. Penna, A. Olivieri, T. Ratcliffe, and H. Coleman. IN-TERNATIONAL COLLABORATION ON BENCHMARK CFD VALI-DATION DATA FOR SURFACE COMBATANT DTMB MODEL 5415. In *Twenty-Third Symposium on Naval Hydrodynamics*, pages 402–422, 2001.

D. Sujudi and R. Haimes. Identification of swirling flow in 3D vector field, Technical report. *Department of Aeronautics and AstroNautics, MiT*, AAIA paper 95-1715, 2010.

H. Theisel and H. P. Seidel. Feature Flow Fields. In *VISSYM '03 Proceedings of the symposium on Data visualisation*, pages 141–148, 2003.

S. Toxopeus. Viscous-flow calculations for KVLCC2 in deep and shallow water. In *MARINE 2011 - Computational Methods in Marine Engineering IV*, pages 351–368, 2011.

Tsinober. Why strain too? In *An Informal Conceptual Introduction to Turbulence*, chapter 6.2.2, page 128. Springer, 1998.

H.-M. Wang, Y.-H. Xie, J.-M. Liu, Z.-J. Zou, and W. He. Experimental and numerical study of hydrodynamic forces on ship in oblique motion. In *Proceedings of the 2011 International Conference on Remote Sensing, Environment and Transportation Engineering (RSETE 2011)*, pages 328–331, 2011.

T. Weinkauf, J. Sahner, H. Theisel, and H.-C. Hege. Cores of Swirling Particle Motion in Unsteady Flows. In *IEEE Transactions on Visualization and Computer Graphics*, volume 13(6), pages 1759–66, 2007.

C. E. Willert and M. Gharib. Three-dimensional particle imaging with a single camera. *Measurement Science and Technology*, 13:683–694, 1992.

C. C. Wolf and R. Hörnschemeyer. Tomographic Particle Image Velocimetry Measurements in a Bluff-Body Wake Flow. *AIAA Journal*, 50:2899–2907, 2012.

T. Xing, S. Bhushan, and F. Stern. Vortical and turbulent structures for KVLCC2 at drift angle 0, 12, and 30 degrees. *Ocean Engineering*, 55:23–43, 2012.

A. Ymuro. SOME EXPERIMENTS ON FLOW-STRAIGHTENING EFFECT OF A PROPELLER IN OBLIQUE FLOWS. *Naval architecture and ocean engineering*, 18:58–68, 1980.

H. Yoon, L. Gui, and F. Stern. DTMB Model 5415(5512) Tomographic PIV Static Drift Tests at β= 0°, 10°, 20°. PART I: Experimental Methods. work report, March 4th 2013.

F. Zhao and Z.-R. Zhang. Numerical simulation of viscous flow around ship model DTMB 5415. In *Proceeding of the 2003 17th National Conference on Hydrodynamics and the 6th National Congress on Hydrodynamics*, pages 345–351, 2003.

J. Zhou, Adrian R.J., S. Balachandar, and Kendall T. M. Mechanisms for generating coherent packets of hairpin vortices in channel flow. *Journal of Fluid Mechanics*, 287:353–396, 1999.

Appendices

Appendix A: Comparison between CFD and EFD data

B1. β = 0°

1) Axial velocity contours and cross-plane streamlines

x/L	CFD	EFD (INSEAN)	EFD (TPIV)
0.06		N/A	
0.1			
0.12		N/A	

x/L	CFD	EFD (INSEAN)	EFD (TPIV)
0.2			
0.4			
0.6			
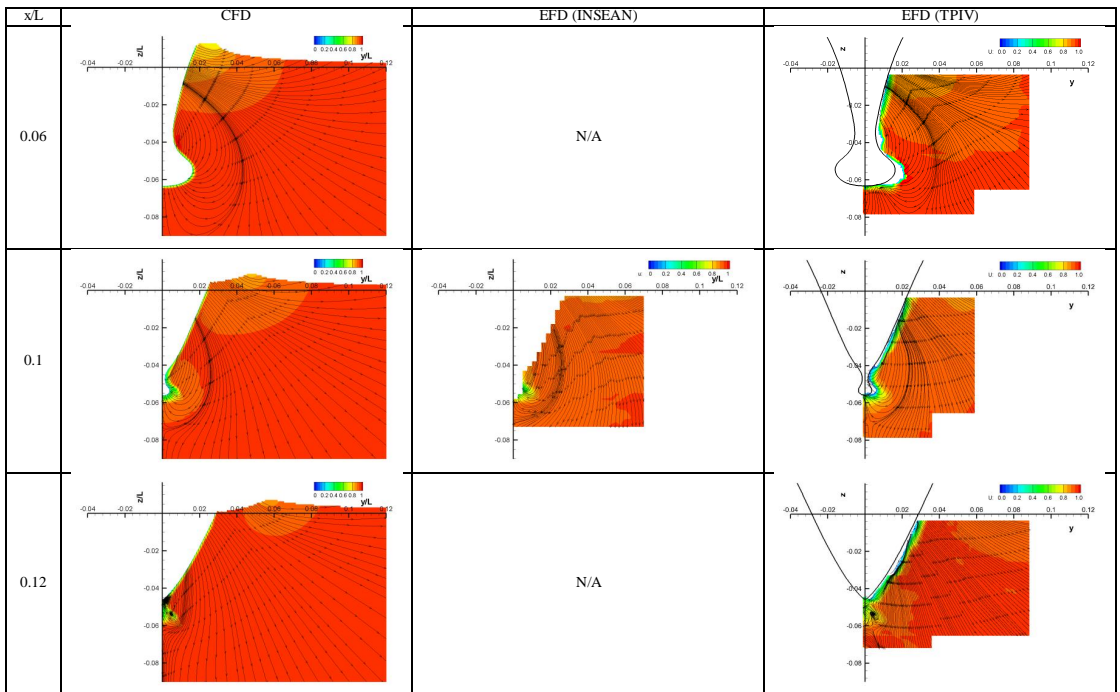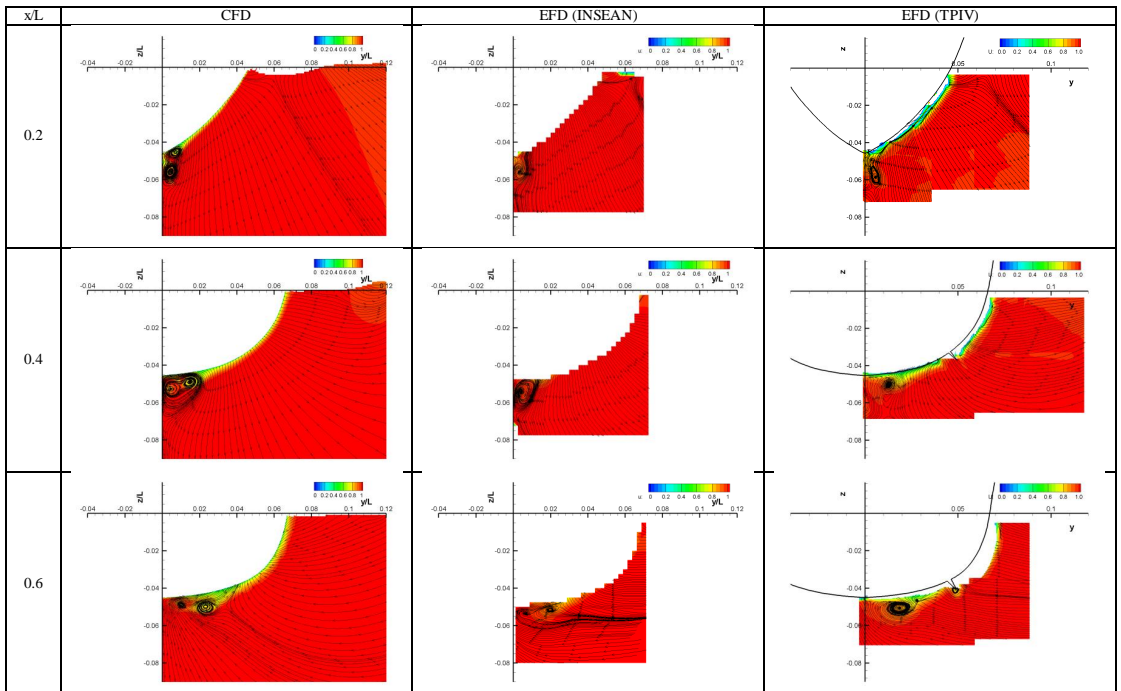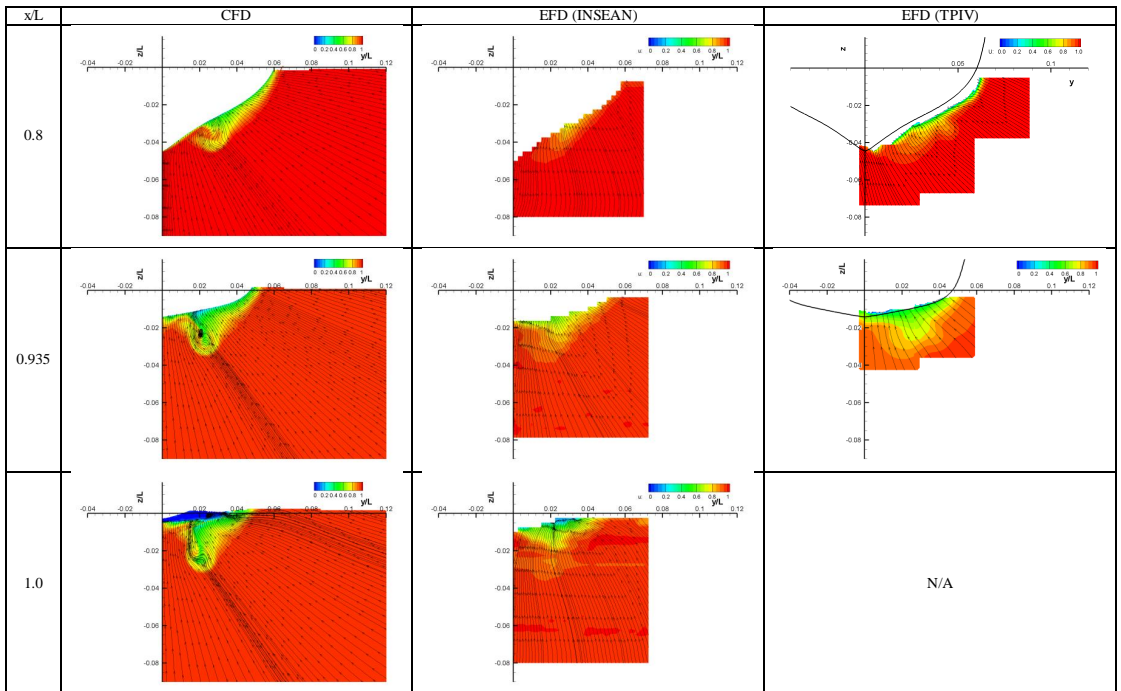
Appendix B: Time histories and FFT's for the SDV β=20°, six measurement stations

x=0.060
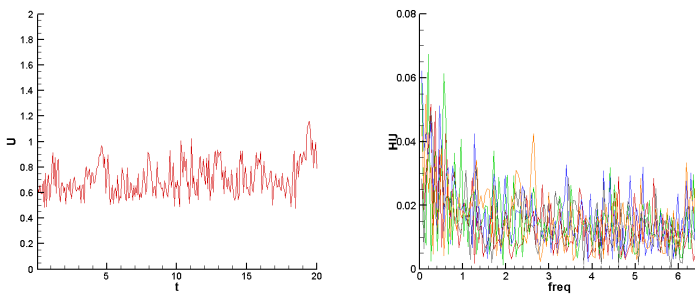
Figure 174: U time history and FFT at point A, x=0.060.
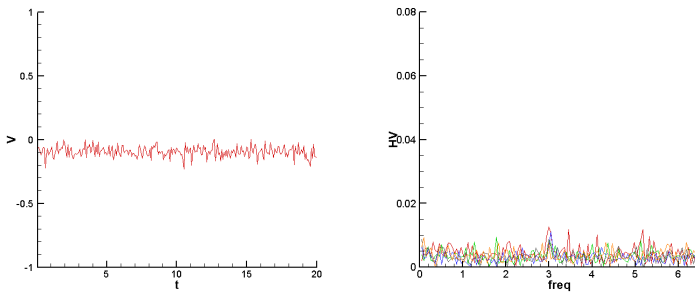
Figure 175: V time history and FFT at point A, x=0.060.
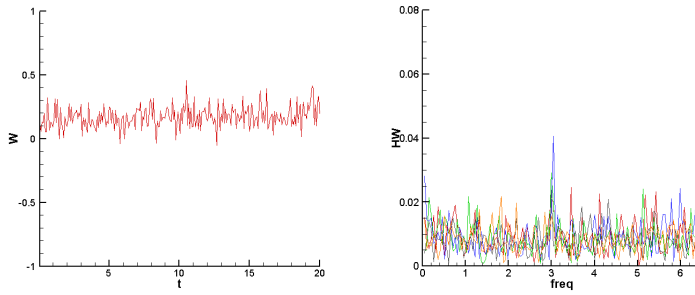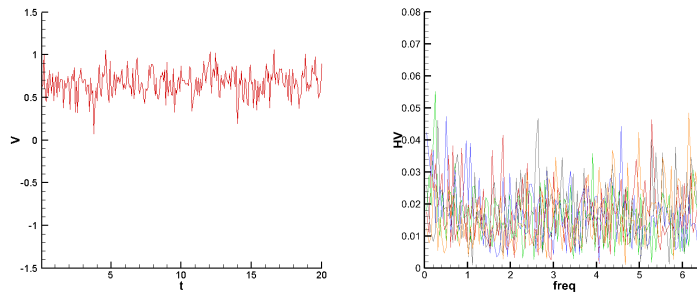
Figure 176: W time history and FFT at point A, x=0.060.
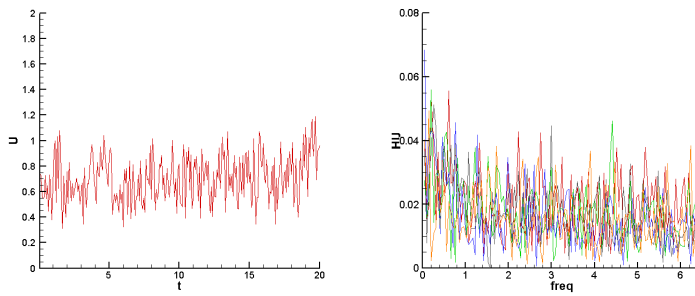
Figure 177: U time history and FFT at point B, x=0.060.
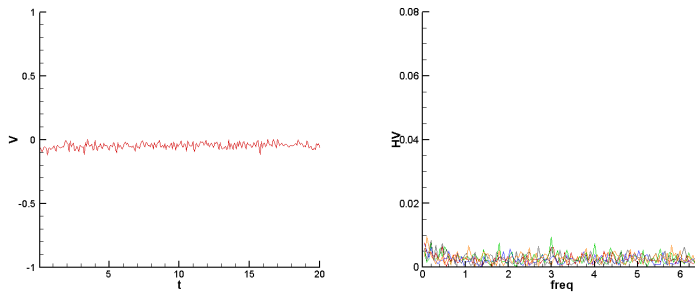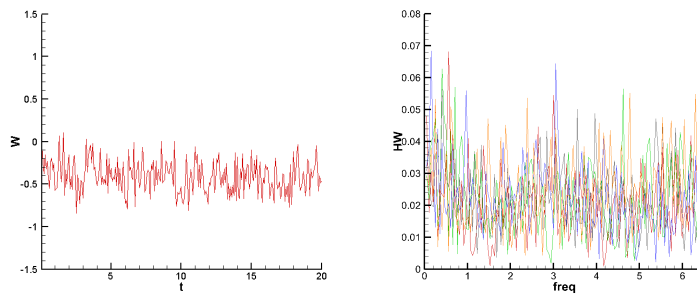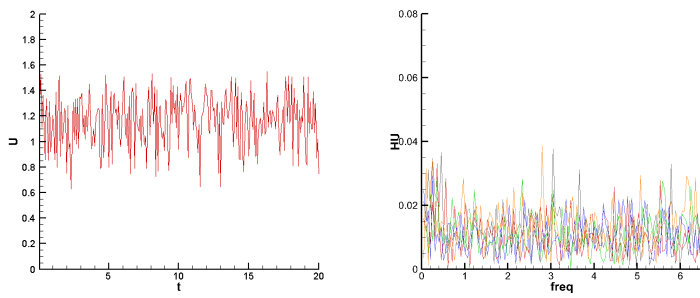

Figure 178: V time history and FFT at point B, x=0.060.
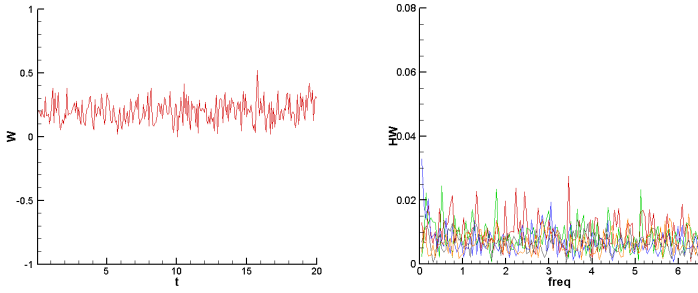
Figure 179: W time history and FFT at point B, x=0.060.
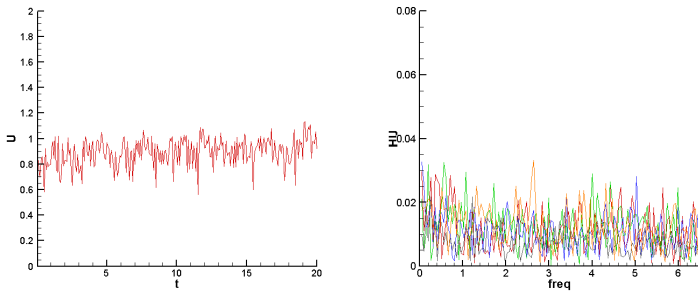
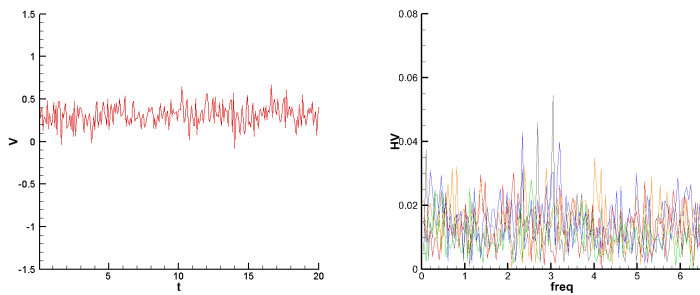**Figure 180:** U time history and FFT at point C, x=0.060.
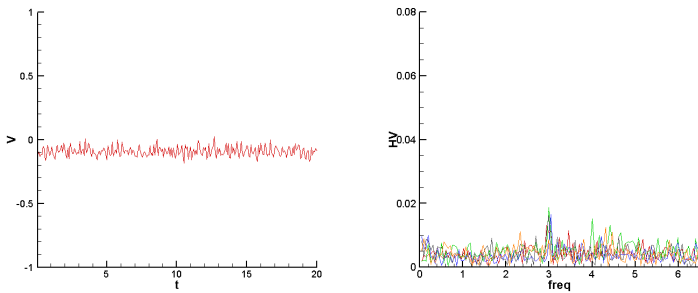
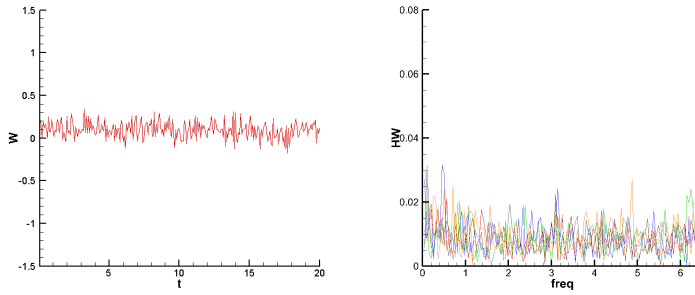**Figure 181:** V time history and FFT at point C, x=0.060.
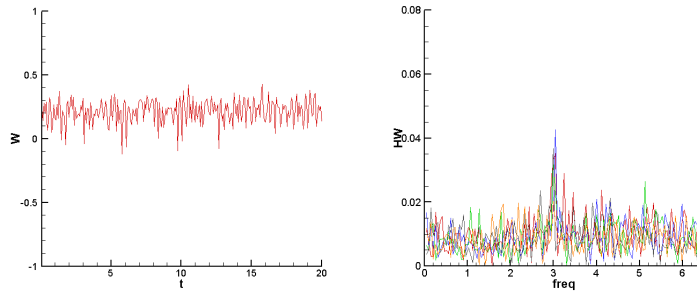
Figure 182: W time history and FFT at point C, x=0.060.
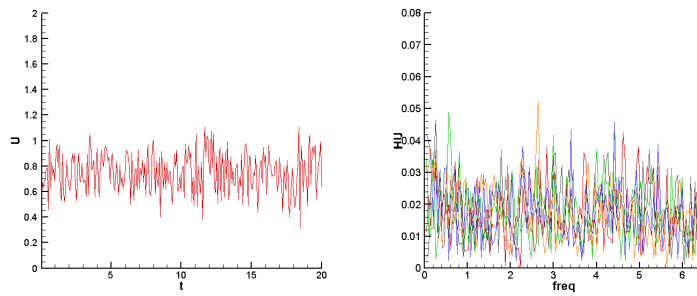
Figure 183: U time history and FFT at point D, x=0.060.
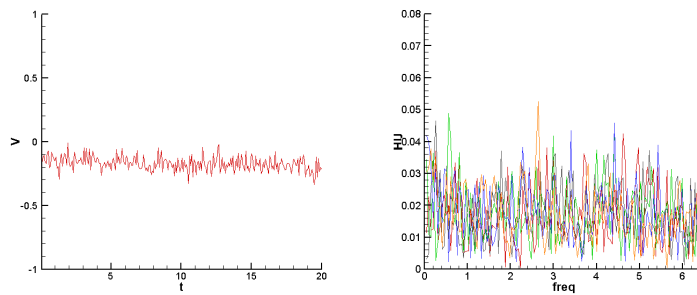
Figure 184: V time history and FFT at point D, x=0.060.
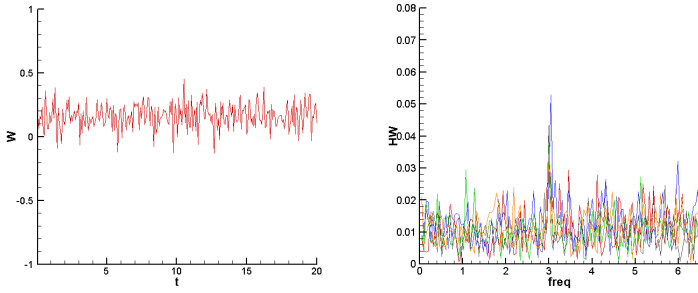
Figure 185: W time history and FFT at point D, x=0.060.
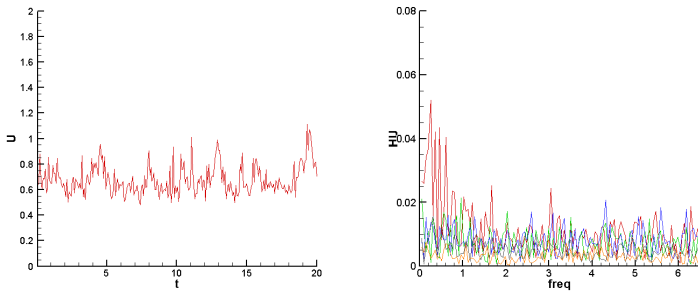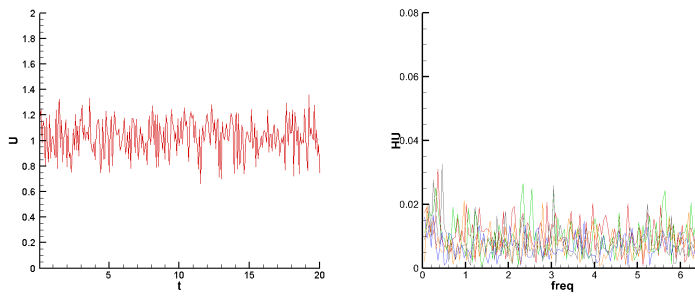

Figure 186: U time history and FFT at point E, x=0.060.
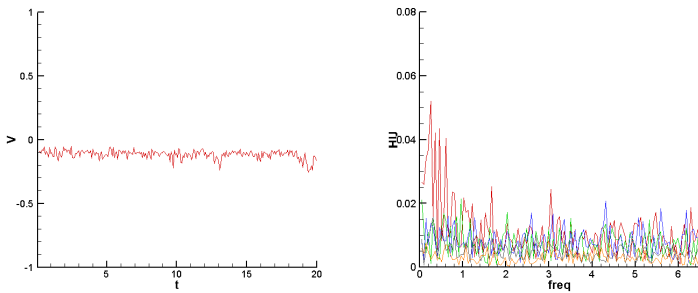
Figure 187: V time history and FFT at point E, x=0.060.
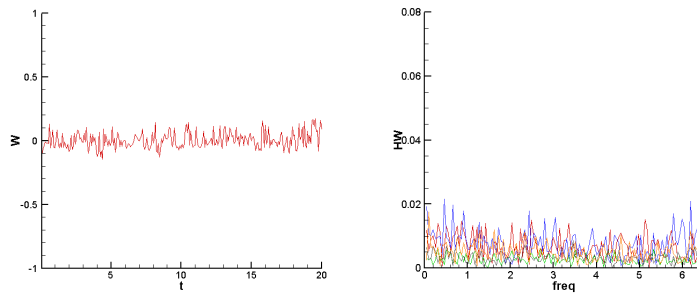
Figure 188: W time history and FFT at point E, x=0.060.

x=0.100
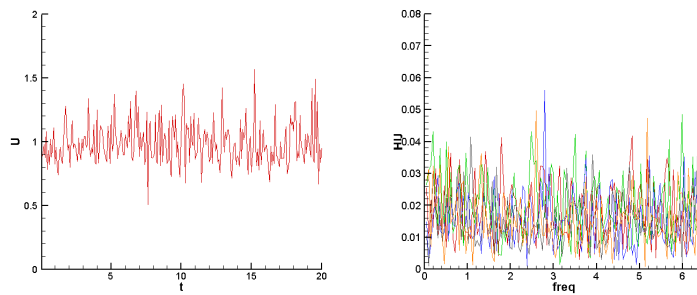
Figure 189: U time history and FFT at point A, x=0.100.
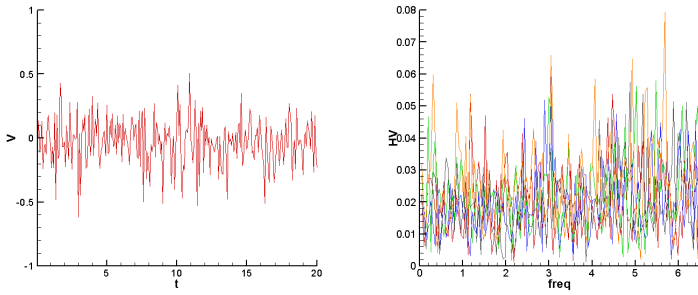
Figure 190: V time history and FFT at point A, x=0.100.
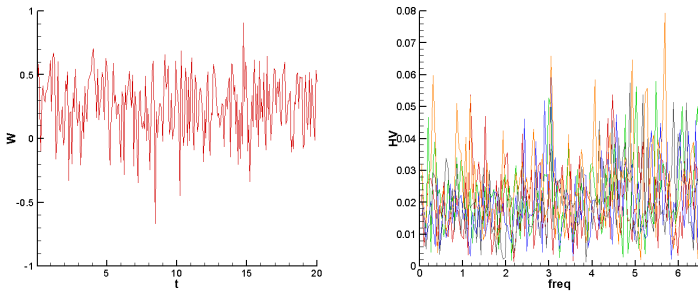
Figure 191: W time history and FFT at point A, x=0.100.
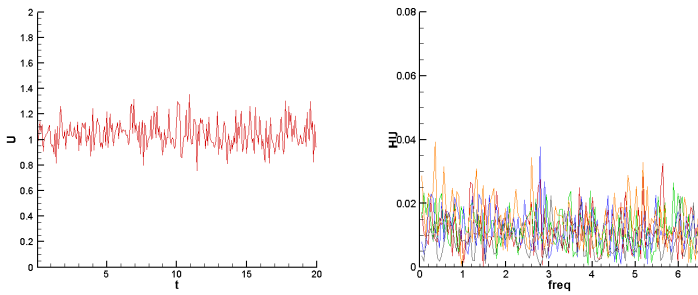
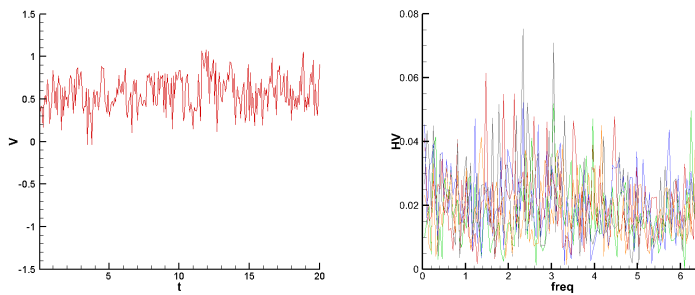**Figure 192:** U time history and FFT at point B, x=0.100.
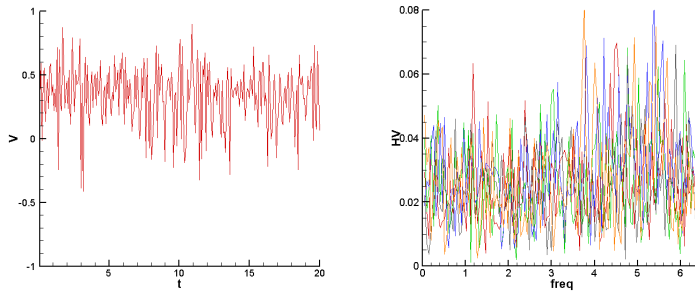
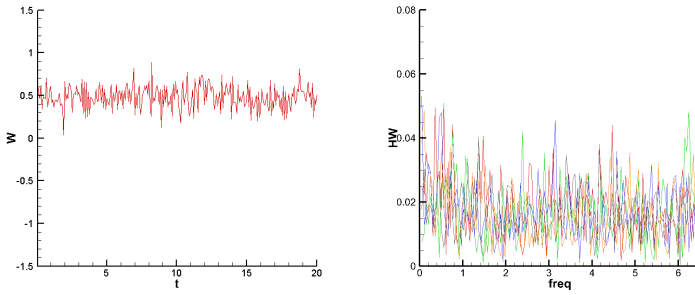**Figure 193:** V time history and FFT at point B, x=0.100.
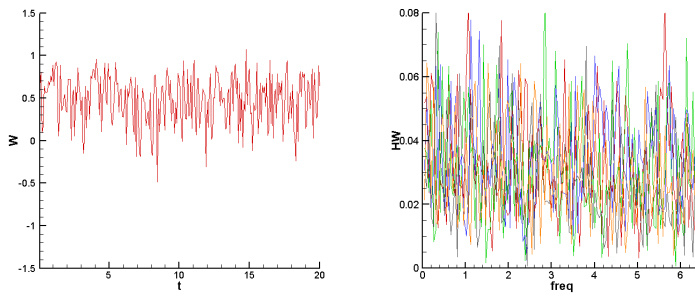
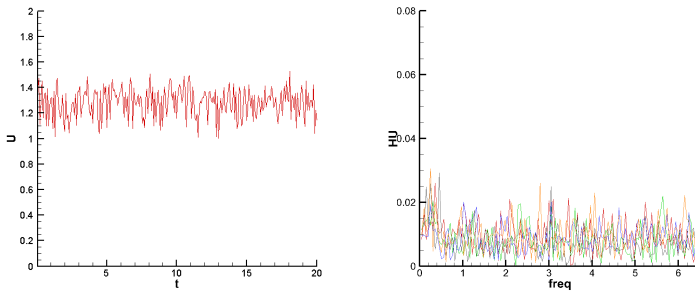**Figure 194:** W time history and FFT at point B, x=0.100.
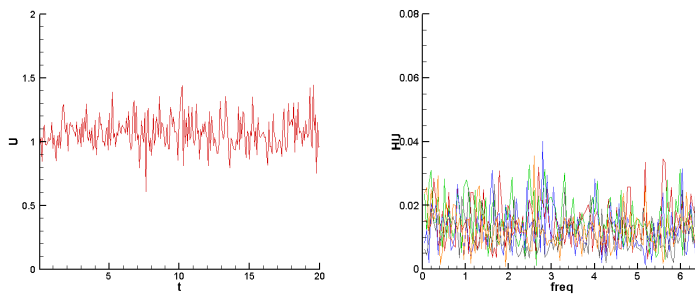
Figure 195: U time history and FFT at point C, x=0.100.
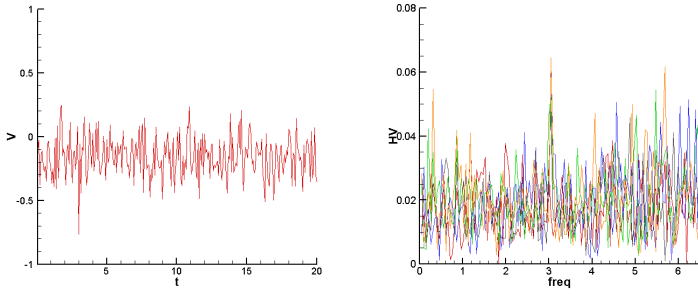
Figure 196: V time history and FFT at point C, x=0.100.
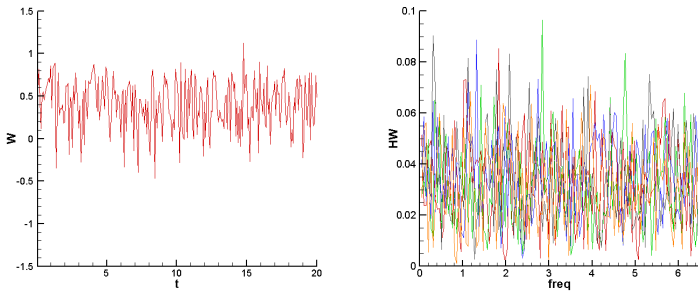
Figure 197: W time history and FFT at point C, x=0.100.
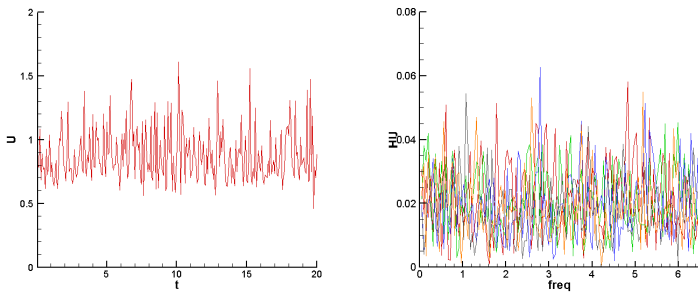
Figure 198: U time history and FFT at point A, x=0.100.
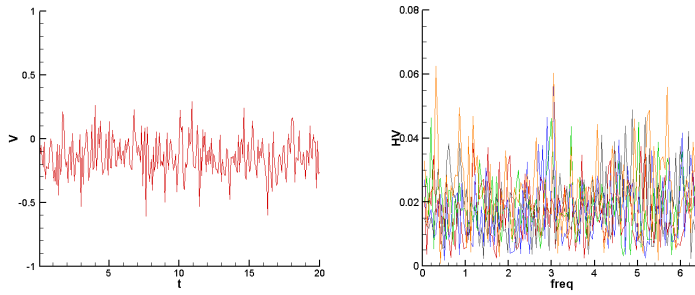
Figure 199: V time history and FFT at point D, x=0.100.
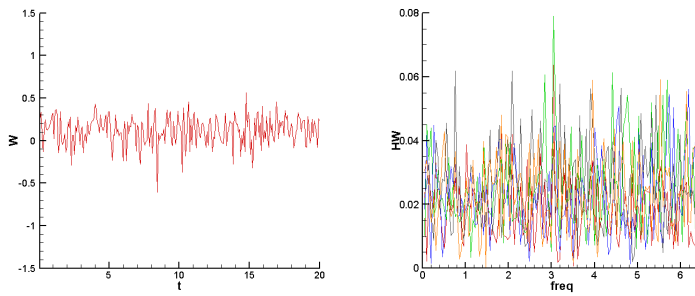
Figure 200: W time history and FFT at point D, x=0.100.
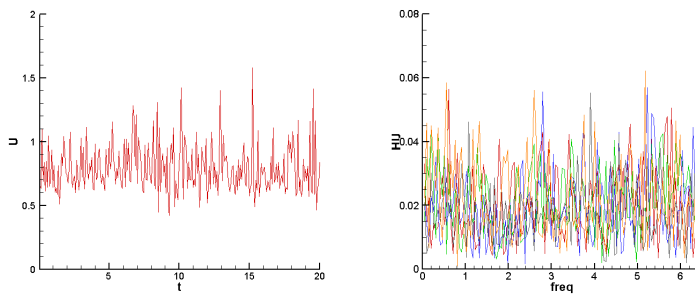
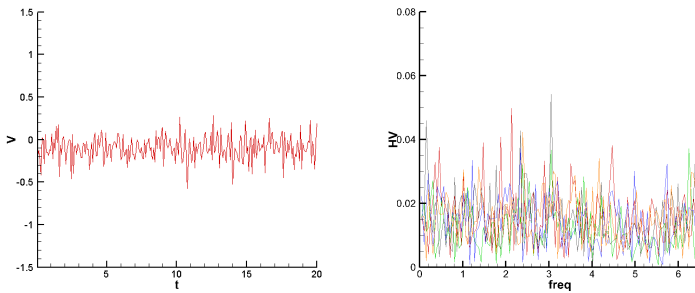**Figure 201:** U time history and FFT at point E, x=0.100.
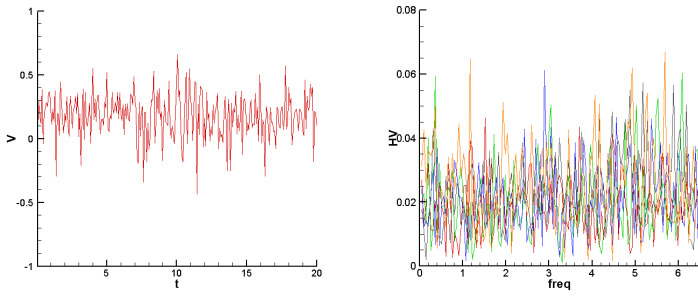
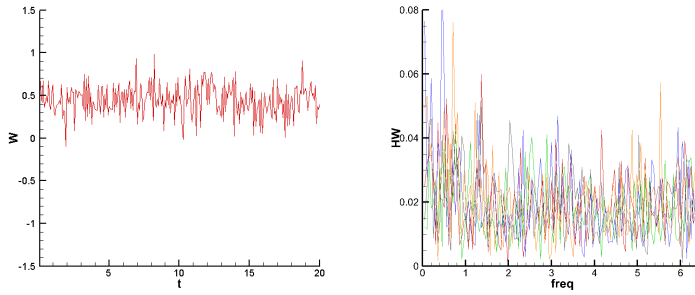**Figure 202:** V time history and FFT at point E, x=0.100.
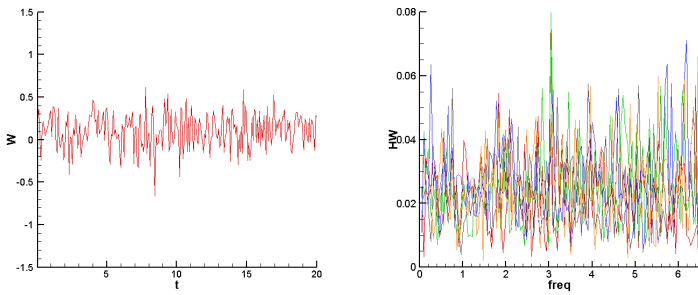
Figure 203: W time history and FFT at point E, x=0.100.
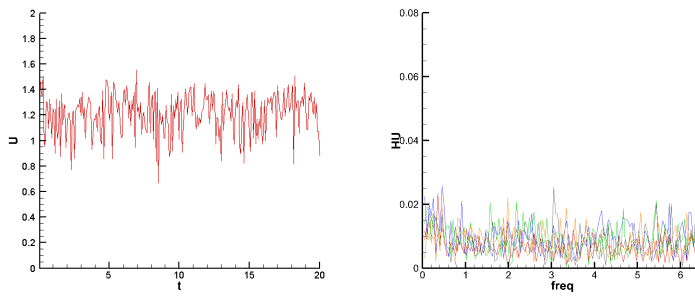
x=0.120
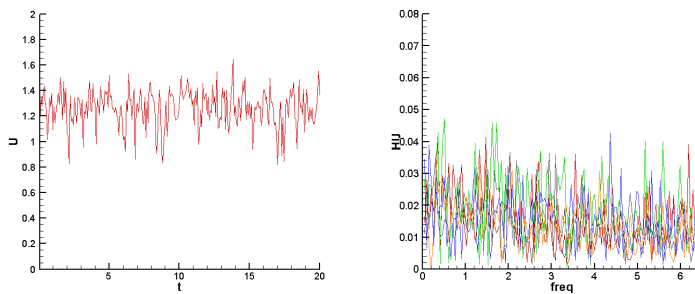
Figure 204: U time history and FFT at point A, x=0.120.
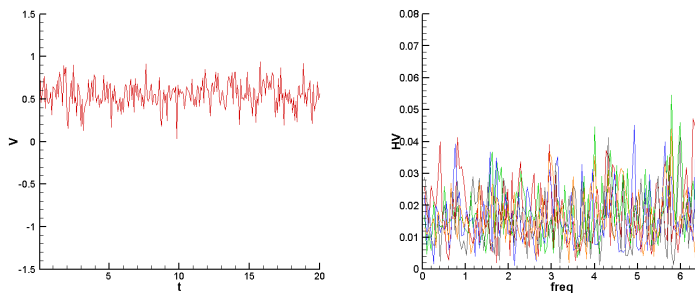
Figure 205: V time history and FFT at point A, x=0.120.
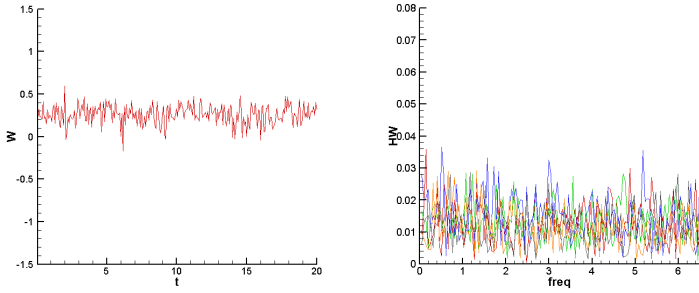
Figure 206: W time history and FFT at point A, x=0.120.
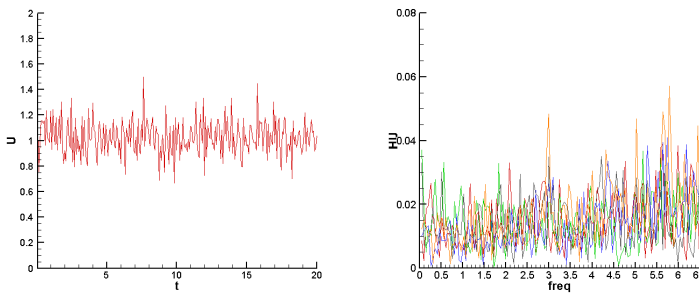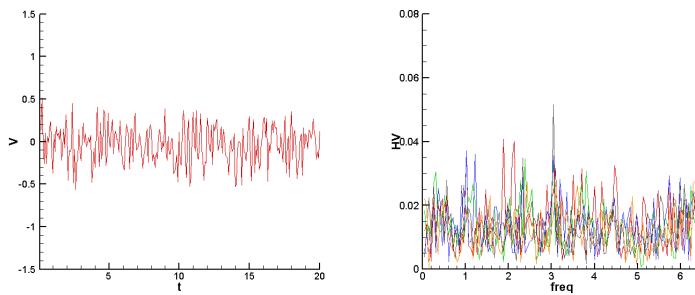

Figure 207: U time history and FFT at point B, x=0.120.
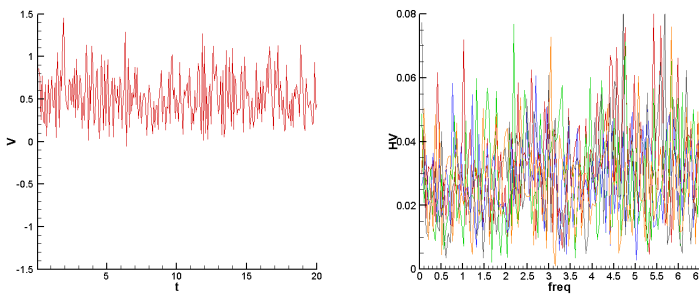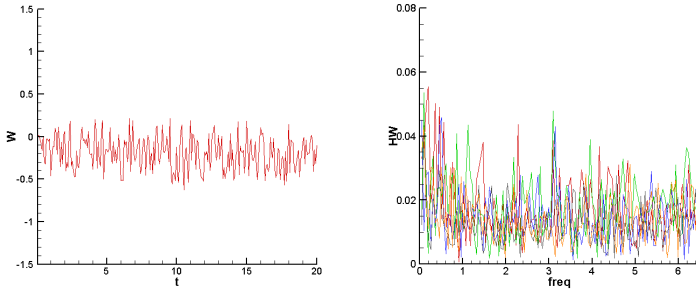

Figure 208: V time history and FFT at point B, x=0.120.
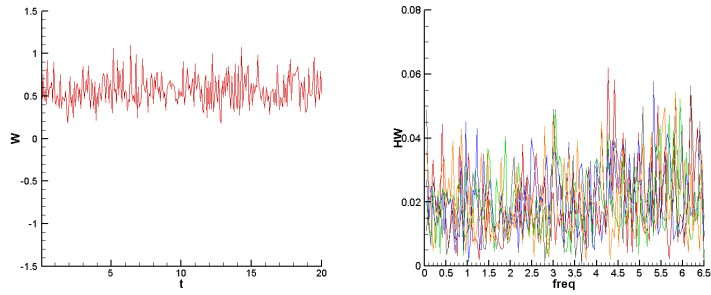
Figure 209: W time history and FFT at point B, x=0.120.
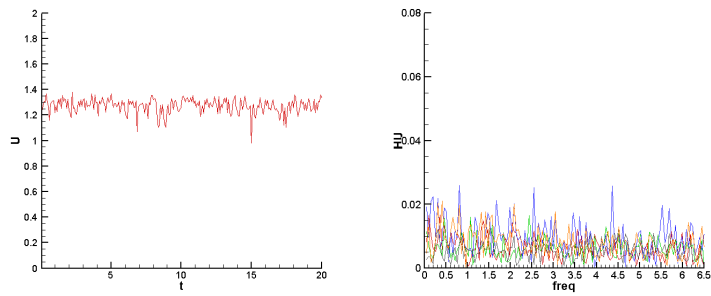
Figure 210: U time history and FFT at point C, x=0.120.
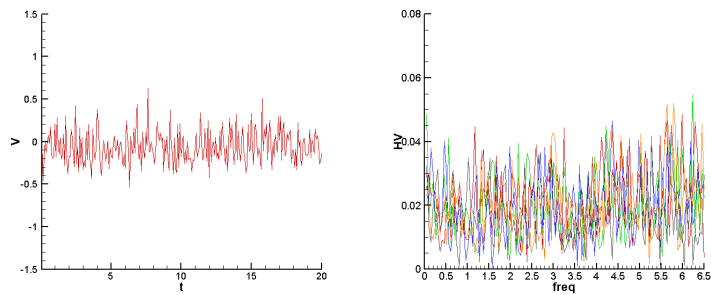
Figure 211: V time history and FFT at point C, x=0.120.
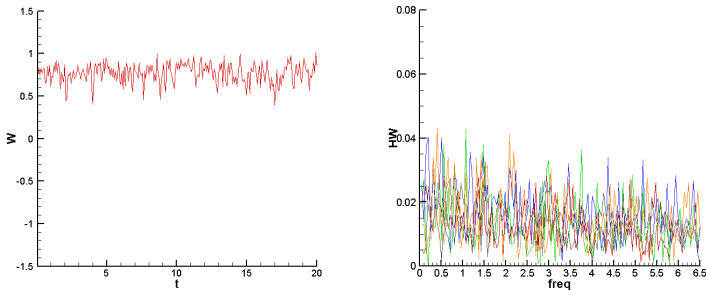
Figure 212: W time history and FFT at point C, x=0.120.
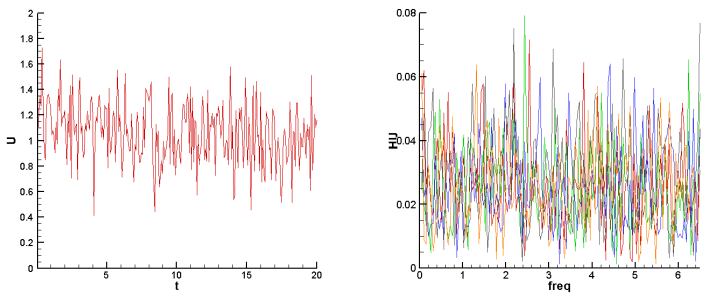
Figure 213: U time history and FFT at point D, x=0.120.
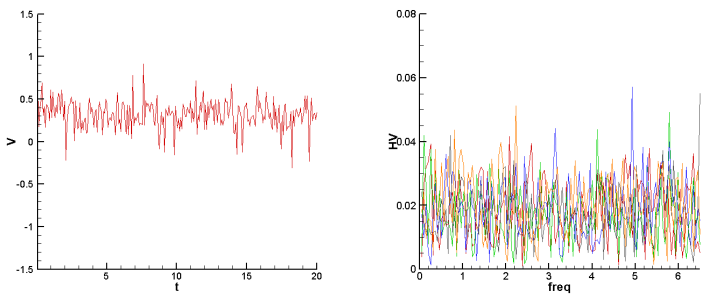
Figure 214: V time history and FFT at point D, x=0.120.
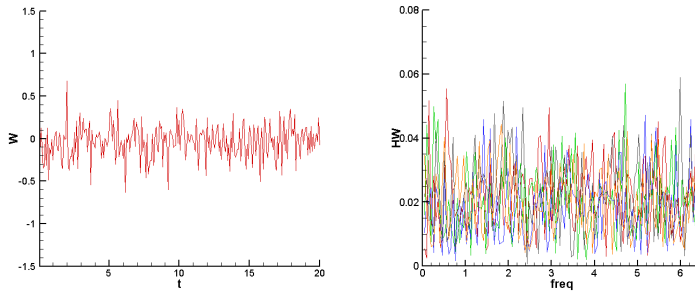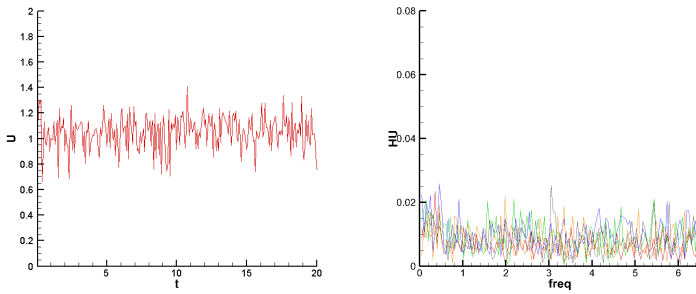
Figure 215: W time history and FFT at point D, x=0.120.
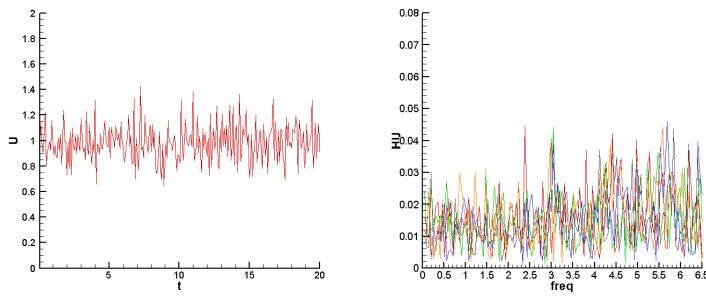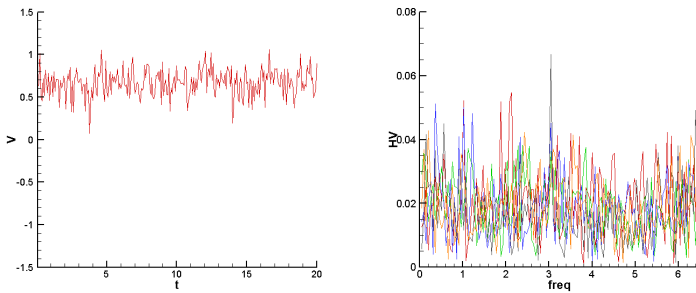

Figure 216: U time history and FFT at point E, x=0.120.
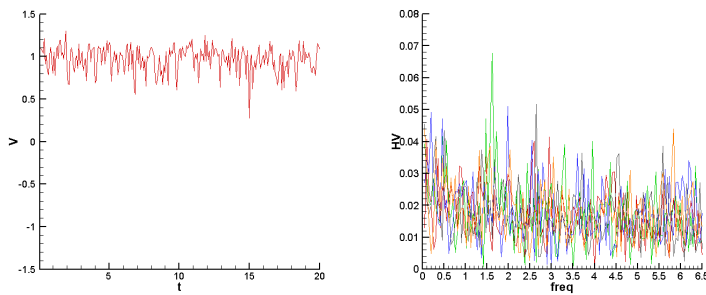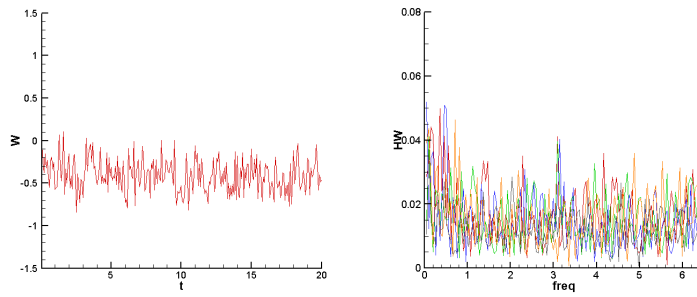

Figure 217: V time history and FFT at point E, x=0.120.
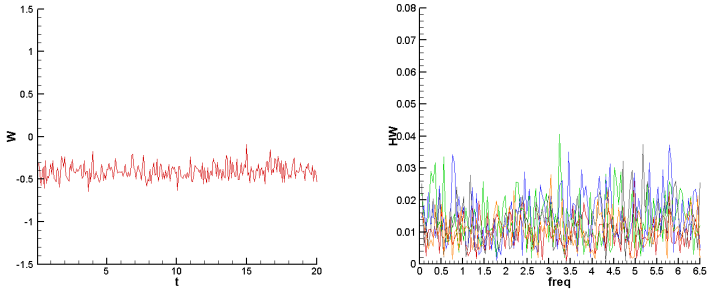
Figure 218: W time history and FFT at point E, x=0.120.
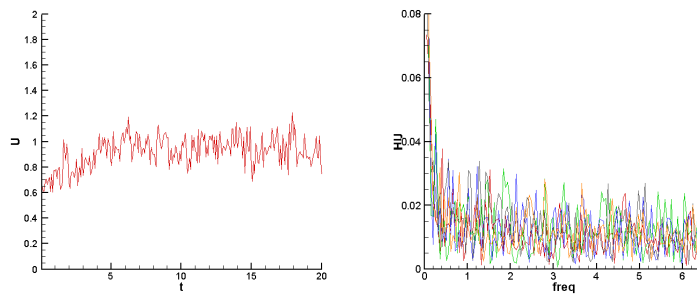
x=0.200
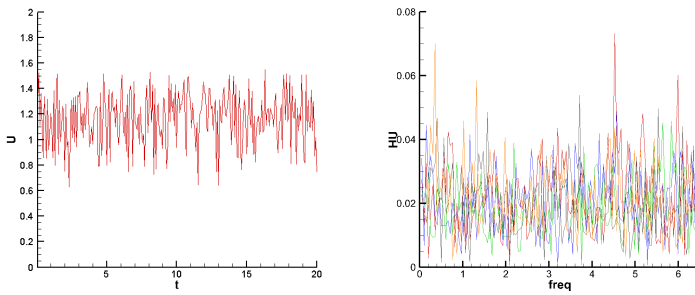
Figure 219: U time history and FFT at point A, x=0.200.
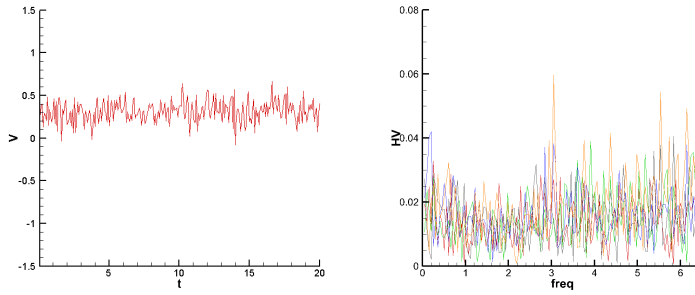
Figure 220: V time history and FFT at point A, x=0.200.
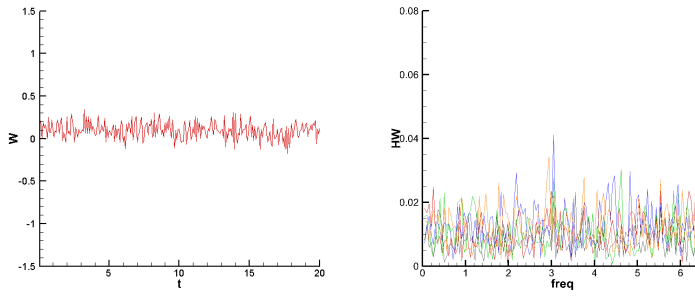
Figure 221: W time history and FFT at point A, x=0.200.
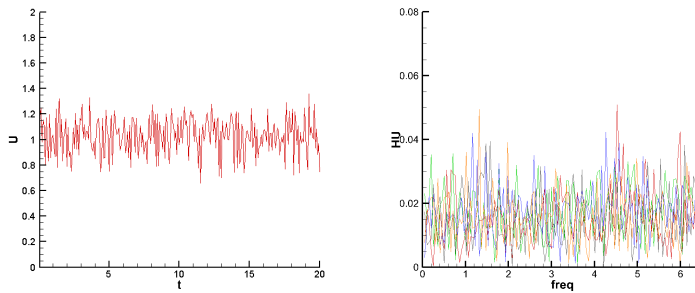
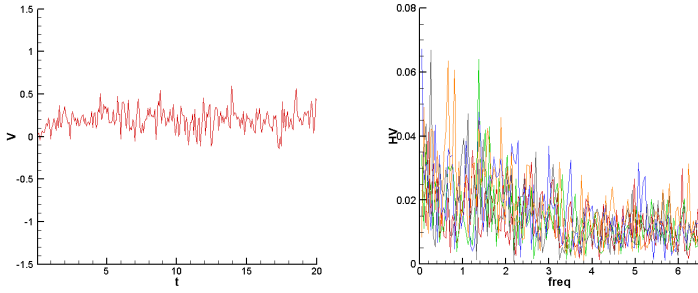**Figure 222:** U time history and FFT at point B, x=0.200.
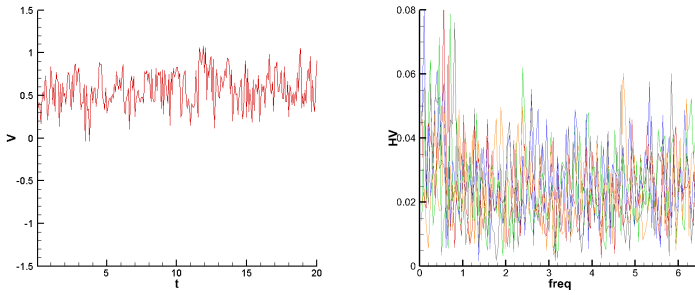
Figure 223: V time history and FFT at point B, x=0.200.
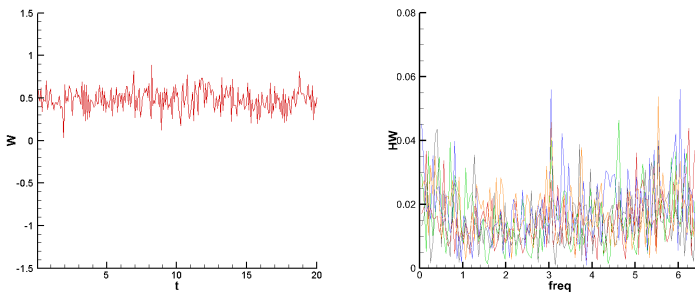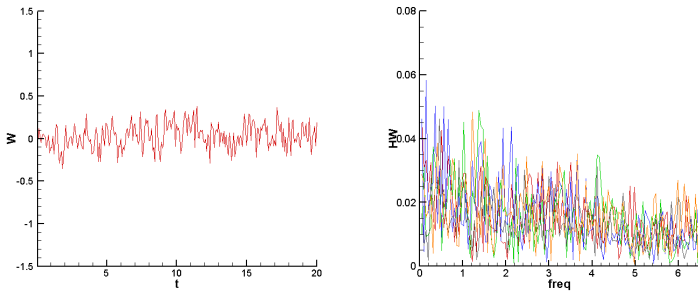

Figure 224: W time history and FFT at point B, x=0.200.
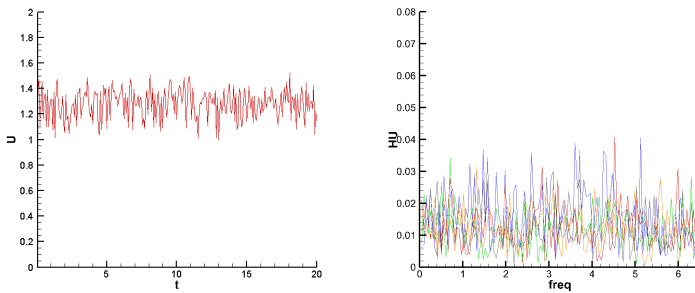
Figure 225: U time history and FFT at point A, x=0.200.
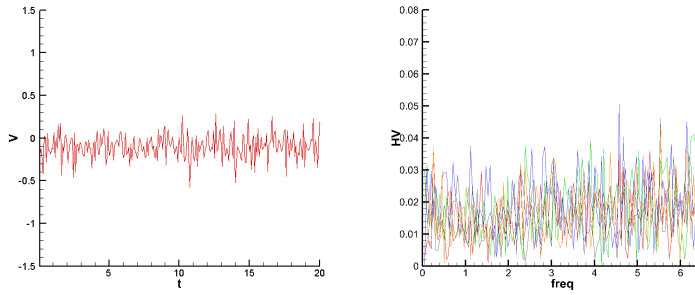
Figure 226: V time history and FFT at point C, x=0.200.
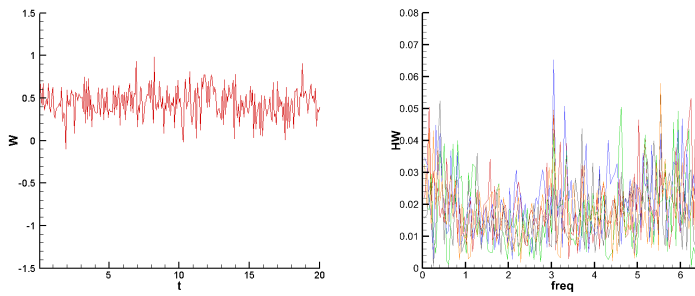
Figure 227: W time history and FFT at point C, x=0.200.
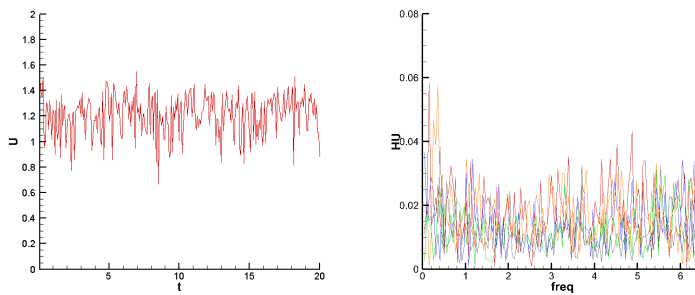
Figure 228: U time history and FFT at point D, x=0.200.
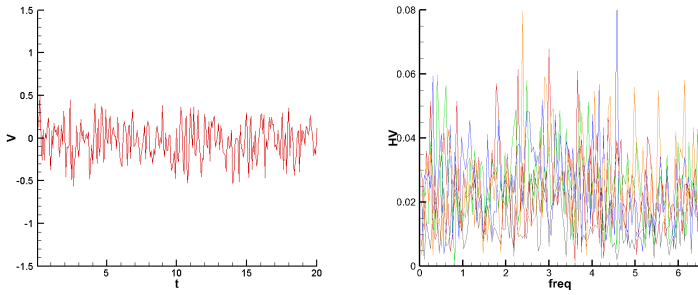
Figure 229: V time history and FFT at point D, x=0.200.
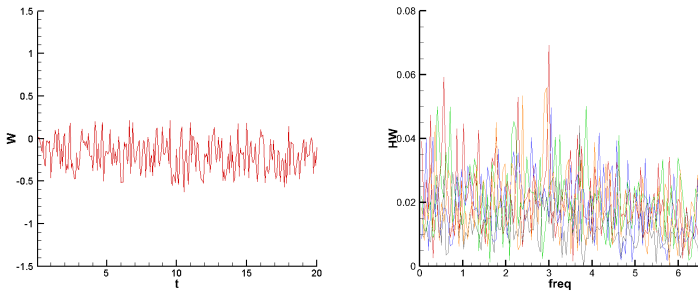
Figure 230: W time history and FFT at point D, x=0.200.
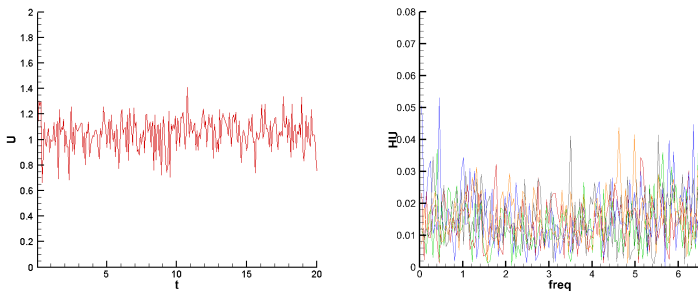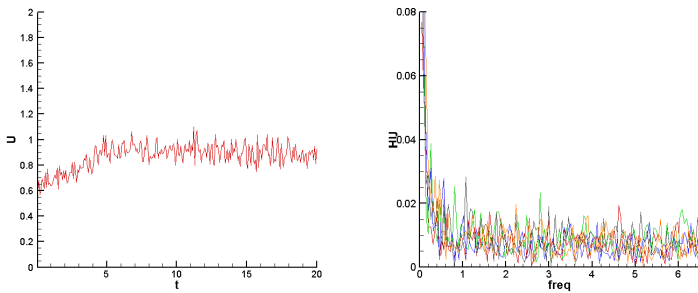

Figure 231: U time history and FFT at point E, x=0.200.
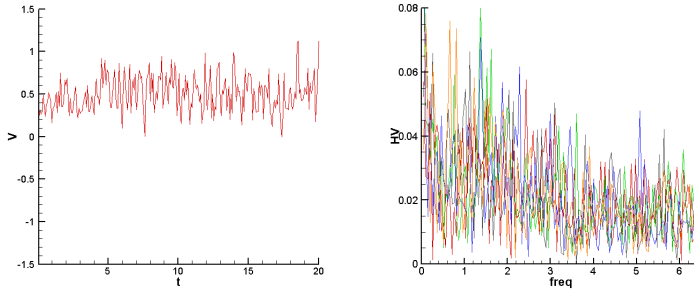
Figure 232: V time history and FFT at point E, x=0.200.

Figure 233: W time history and FFT at point E, x=0.200.

x=0.400

Figure 234: U time history and FFT at point A, x=0.400.

Figure 235: V time history and FFT at point A, x=0.400.

Figure 236: W time history and FFT at point A, x=0.400.

Figure 237: U time history and FFT at point B, x=0.400.

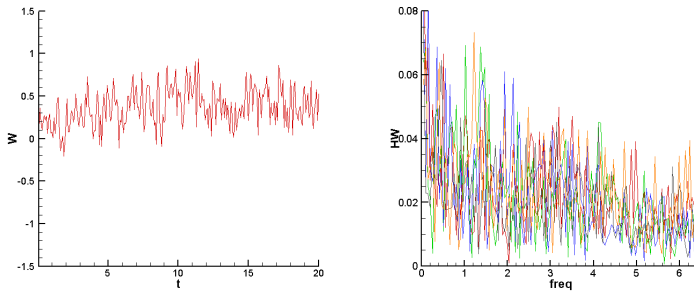**Figure 238:** V time history and FFT at point B, x=0.400.

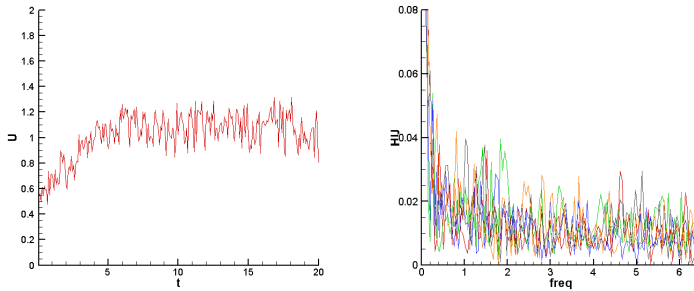**Figure 239:** W time history and FFT at point B, x=0.400.

Figure 240: U time history and FFT at point C, x=0.400.

Figure 241: V time history and FFT at point C, x=0.400.

Figure 242: W time history and FFT at point C, x=0.400.

Figure 243: U time history and FFT at point D, x=0.400.
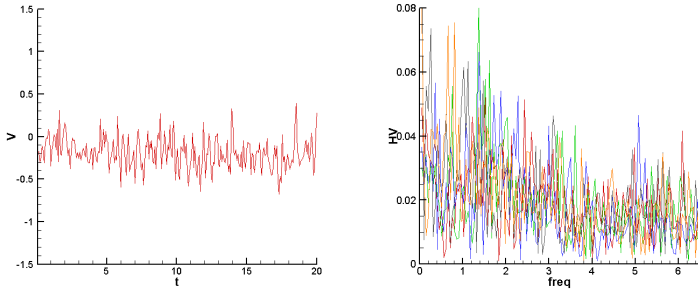

Figure 244: V time history and FFT at point D, x=0.400.
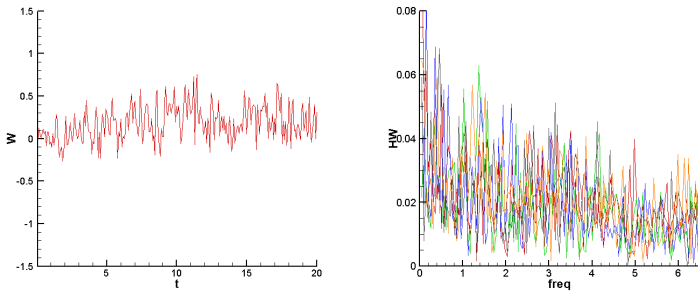
Figure 245: W time history and FFT at point D, x=0.400.

Figure 246: U time history and FFT at point E, x=0.400.

Figure 247: V time history and FFT at point E, x=0.400.

Figure 248: W time history and FFT at point E, x=0.400.

x=0.600

Figure 249: U time history and FFT at point A, x=0.600.

Figure 250: V time history and FFT at point A, x=0.600.

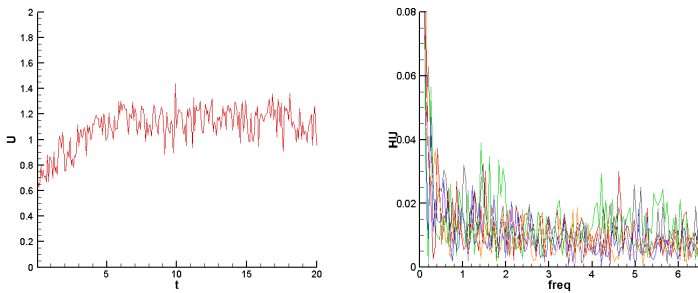**Figure 251:** W time history and FFT at point A, x=0.600.

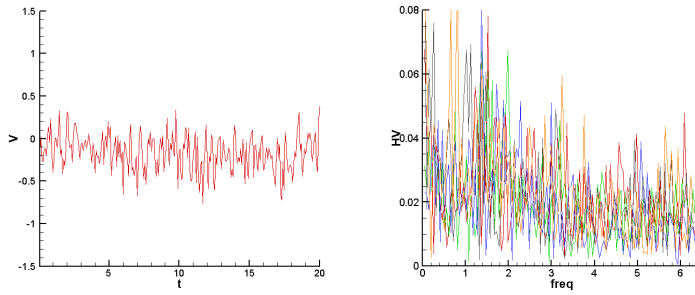

Figure 252: U time history and FFT at point B, x=0.600.

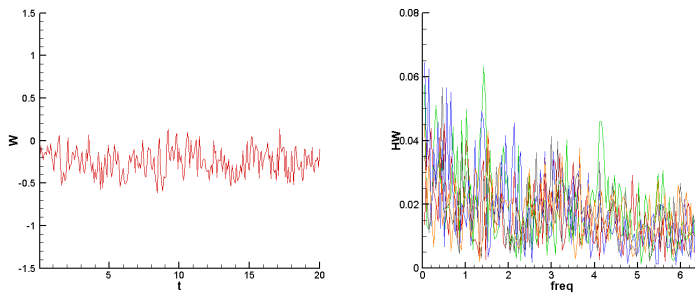**Figure 253:** V time history and FFT at point B, x=0.600.

Figure 254: W time history and FFT at point B, x=0.600.

Figure 255: U time history and FFT at point C, x=0.600.

Figure 256: V time history and FFT at point C, x=0.600.

Figure 257: W time history and FFT at point C, x=0.600.

Figure 258: U time history and FFT at point D, x=0.600.

Figure 259: V time history and FFT at point D, x=0.600.

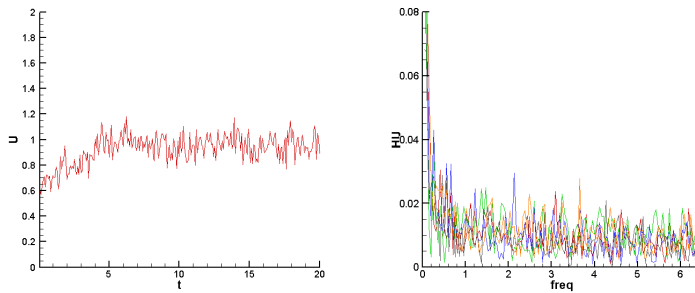**Figure 260:** W time history and FFT at point D, x=0.600.

Figure 261: U time history and FFT at point E, x=0.600.

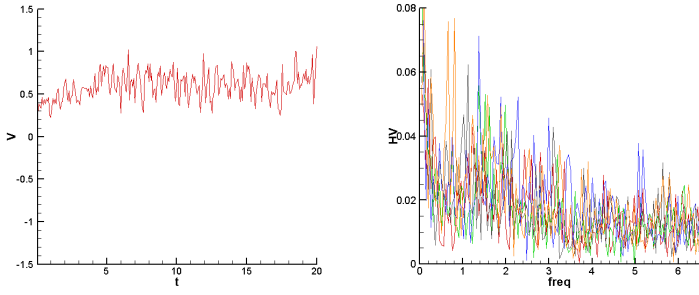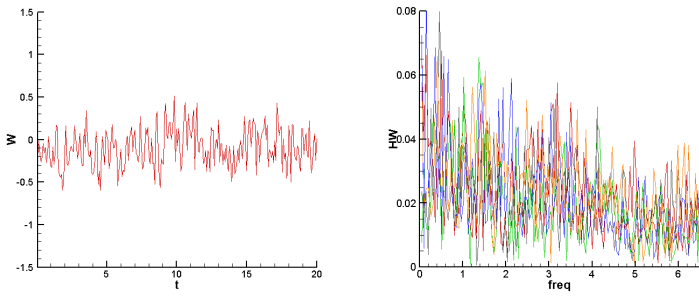**Figure 262:** V time history and FFT at point E, x=0.600.

Figure 263: W time history and FFT at point E, x=0.600.